Order Number 9410181

A self-consistent time varying auroral model

Min, Qilong, Ph.D.

University of Alaska Fairbanks, 1993

U·M·I
300 N. Zeeb Rd.
Ann Arbor, MI 48106

A SELF-CONSISTENT TIME VARYING AURORAL MODEL

A

THESIS

Presented to the Faculty

of the University of Alaska Fairbanks

in Partial Fulfillment of the Requirements

for the Degree of

DOCTOR OF PHILOSOPHY

By

Qilong Min, B.S., M.S.

Fairbanks, Alaska

September 1993

A SELF-CONSISTENT TIME VARYING AURORAL MODEL

By

Qilong Min

RECOMMENDED:

Prof. J. R. Kan

Dr. D. Lummerzheim

Prof. R. Piacenza

Prof. K. Stamnes

Prof. M. H. Rees, Chairman, Advisory Committee

Prof. J. L. Morack, Head, Physics Department

APPROVED:

P. B. Reichardt, Dean, College of Natural Sciences

E. Murphy, Chancellor's Faculty Assoc., Graduate Studies

22 July 1993

Date

ABSTRACT

A time dependent model of auroral processes has been developed by self-consistently solving the electron transport equation, the ion continuity equations and the electron and ion energy equations. It is used to study the response of ionospheric and atmospheric properties in regions subjected to electron bombardment. The time history of precipitation events is computed for a variety of electron spectral energy distributions and flux magnitudes. Examples of daytime and night-time aurorae are presented. Precipitating energetic auroral electrons heat the ambient electrons and ions as well as enhancing the ionization rate which increases the ion concentration. The consequences of electric field acceleration and an inhomogeneous magnetic field in auroral electron transport in the topside ionosphere are investigated. Substantial perturbations of the low energy portion of the electron flux are produced: An upward directed electric field accelerates the downward directed flux of low energy secondary electrons and decelerates the upward directed component. Above about 400 km the inhomogeneous magnetic field produces anisotropies in the angular distribution of the electron flux. The effects of the perturbed energy distributions on auroral spectral emission features and on the electron temperature are noted. The response of the Hall and Pederson conductivities to auroral electron precipitation is discussed as a function of the characteristic energy of the spectral distribution.

TABLE OF CONTENTS

LIST OF FIGURES

LIST OF TABLES

ACKNOWLEDGMENTS

The completion of the research work underlying this thesis would not have been possible without the steady advice and encouragement of the chairman of my advisory committee, Prof. M. H. Rees. He introduced me to the research of auroral physics and provided a constant guidance, leading me through the maze of the research project. Not only did he support me in scientific aspects, but also he encouraged me to cultivate my social and language abilities which are essential for succeeding in the world of research. His commitment to excellence, dedication, and patience are things that I hope to carry with me to future endeavors.

I would like to take this chance to thank the other committee members: Profs. J. Kan, R. Piacenza, and K. Stamnes, and Dr. D. Lummerzheim for their valuable suggestions, comments and constant encouragement in carrying through my Ph.D. project. In particular, Prof. K. Stamnes and Dr. D. Lummerzheim have made many critical and helpful comments for improving the research.

I also want to thank my fellow graduate students in Geophysical institute and many friends, Yongxiang Hu, Nettie LaBelle-Hamer, Øystein Lie-Svendsen, Deli Shen, and Jih-Hong Shue, for their help in countless discussions, and for their help directly or indirectly related with the completion of the thesis.

This work has been supported in part by a grant from the National Science Foundation ATM90-22197 and a grant from National Aeronautics and Space Administration NAG5-1097. The computations were performed on the computers of the University of Alaska.

Finally, I am extremely grateful to my wife Furong Long and my baby daughter Nancy for their love, care, understanding and encouragement during my graduate studies.

CHAPTER 1

Introduction

Aurora, in particular its most spectacular and curtain-like intense form, the *discrete aurora*, manifests itself as a result of plasma energization processes primarily taking place in the coupled magnetosphere-ionosphere system in which energy, momentum, and mass are transported between the magnetosphere and the ionosphere. The development of auroral physics required contributions from a large number of disciplines, including the study of solar phenomena, solar wind in the interplanetary space, magnetospheric phenomena, and processes in the upper atmosphere. Precipitating energetic electrons and/or protons along magnetic field lines from the magnetosphere into the ionosphere produce ionization that enhances the ion and electron densities as well as heating the ambient electron and ion gases, thus affecting the conductivity of the ionosphere. In this coupled system, however, the ionosphere is not a passive element. The spatial distribution of ionospheric conductivity affects magnetospheric plasma transport and the configuration of the magnetospheric current systems that are the principal carriers of mass, momentum, and energy between the ionosphere and the magnetosphere. Meanwhile, the global thermospheric neutral response to ion drag and Joule heating is critically dependent on the ionospheric conductivity. On the other hand, aurorally produced changes in atmospheric/ionospheric parameters may cause perturbations to the phase space distribution of the precipitating electrons, i.e. the physical processes are coupled and electrons precipitating from the magnetosphere to the ionosphere are the key element. It was not possible to investigate the coupled physical processes without first understanding the evolution of the phase space distribution of electrons and/or protons as they penetrate into the inhomogeneous atmosphere.

1.1 Overview

As an important phenomenon of magnetosphere-ionosphere (M-I) coupling, aurora has been studied by both the magnetospheric and ionospheric communities for more than half a century. Numerous measurements have been made by sounding rockets and satellites, since the first *in situ* measurements performed in the 1960s by sounding rockets. Various features related to aurora were detected such as quasi-monoenergetic beams of electrons over auroral arcs [*McIlwain*, 1960], strongly field aligned fluxes of electrons [*Hoffman and Evans*, 1968], the inverted-V structure on the energy-time spectrogram of auroral precipitation [*Frank and Ackerson*, 1971], the "forbidden region" in phase space defined by the potential well with a magnetic and electric mirror [*Albert and Lindstrom*, 1970], perpendicular electric "shock" [*Mozer et al.*, 1977], weak double layers [*Temerin et al.*, 1982], "electron conic" signatures [*Menietti and Burch*, 1985], and the existence of parallel electric fields in inverted-V regions inferred by using the co-orbiting DE-1 and DE-2 [*Reiff et al.*, 1988].

The study of auroral processes is based largely on measurements of electron and ion distributions that result from particle interactions with electric and magnetic fields, and with the atmospheric environment. *Alfvén*'s [1958] parallel electric field hypothesis led to the development of numerous theoretical models of auroral electron acceleration. The first modeling attempts by *Knight* [1973] and *Lennartsson* [1976] introduced a scheme whereby a nonresistive acceleration may occur simply because of the magnetic mirroring geometry. A quite successful model of the electron distribution resulting from such a nonresistive acceleration, including the backscattering of electron, was introduced by *Evans* [1974]. Many other models followed, based on the concept of *Evans* [*Kaufmann et al.*, 1976, *Pulliam et al.*, 1981]. *Chiu* and coworkers (see review by *Chiu et al.* [1983]) focused on the data from the USAF satellites and developed a detailed theoretical model [*Chiu and Schulz*, 1978; *Chiu and Cornwall*, 1980] incorporating the ideas of *Alfvén and*

Fälthammar [1963], *Knight* [1973] and *Lennartsson* [1976] on the maintenance of parallel electric fields through the principle of quasi-neutrality as applied to plasma-sheet electron and ion distributions. *Stasiewicz* [1985, *Stasiewicz et al.*, 1987] suggested that the low-energy electron power-law component is formed within the acceleration region by the combined action of a parallel electric field and wave-particle interactions. Alternatively, *Bryant* [1983, 1990] suggested that this power-law component and the associated broad electron energy peak are indicative of a wave-energization mechanism. *Gurgiolo and Burch* [1988] performed computer simulations based on various model potential profiles to explain the observed auroral electron distributions measured by the DE-1 spacecraft at high altitudes.

Meanwhile, several processes (rewieved by *Kan*, 1982; *Lundin and Eliasson*, 1991) have been proposed for the electron acceleration: a) magnetic mirroring (e.g. *Alfvén and Fälthammar*, 1963); b) Double layers (e.g. *Block*, 1972); c) collisionless thermoelectric fields [*Hultqvist*, 1971]; d) "anomalous resistivity" [*Papadopolous*, 1977]; e) Alfvén waves [*Goertz and Boswell*, 1979; *Temerin et al.*, 1986]; f) Lower hybrid waves [*Bingham et al.*, 1984]. It is believed that most of the proposed theories for field aligned electron acceleration may operate, but only a few are expected to be important.

Transport of auroral electrons in the magnetosphere is governed by the magnetic field topology, by currents, and by waves. In the thermosphere, the region of auroral production, transport of the electrons is dominated by collisions. The spectroscopic aurora is the result of excitation of atomic and molecular constituents produced by particle impact on the neutral atoms and molecules as well as by chemical reactions (reviewed by *Rees and Lummerzheim*, 1991; *Vallance Jones*, 1991). Ratios of emission features are used to infer characteristics of the precipitating electrons and to determine ionospheric properties locally from ground based observations [*Strickland et al.*, 1983; *Vallance Jones et al.*, 1987; *Christensen et al.*, 1987] or on the scale of an auroral

oval from satellite images [*Rees et al.*, 1988; *Lummerzheim et al.*, 1991]. The spectroscopic ratio method was pioneered by *Rees* (e.g. *Rees*, 1958; *Rees*, 1963; *Rees and Luckey*, 1974; *Rees and Roble*, 1986) and *Vallance Jones* (e.g. *Vallance Jones*, 1974). Current approaches to modeling the relationship of the ratio of emission features to the characteristics of the precipitating electrons are based on electron transport calculations which yield the electron intensity as a function of altitude and energy. Different methods and algorithms for the solution of the electron transport equation have been reported. Monte Carlo simulation [*Berger et al.*, 1970], two-stream calculations [*Banks and Nagy*, 1970; *Nagy and Banks*, 1970; *Banks et al.*, 1974; *Mantas*, 1975; *Stamnes*, 1980; *Stamnes*, 1981; *Link*, 1992], and angular dependent or multi-stream calculations [*Strickland and Kepple*, 1974; *Strickland et al.*, 1976; *Stamnes*, 1980; *Porter et al.*, 1987; *Lummerzheim*, 1987; *Lilensten*, 1989] have been applied to auroral electron transport. Knowledge of the electron intensity provides the means to study the ionospheric properties of aurora, as well as the volume emission rates of spectral lines and bands that result from direct electron impact on neutrals and from chemical reactions.

To study the response of the thermosphere to electron bombardment, several investigators have solved the time-dependent ion continuity equations including diffusion and chemical reactions (e.g. *Walker and Rees*, 1968; *Schunk and Walker*, 1970a; 1970b; *Jones and Rees*, 1973; *Roble and Rees*, 1977). Publications on time-dependent auroral modeling [*Jones and Rees*, 1973; *Rees and Jones*, 1973], in which O^+ was asummed to be the dominant diffusing ion and N^+, He^+ and H^+ were minor diffusing ions, demonstrated that ionospheric chemistry and spectroscopic emission morphology are controlled primarily by the temporal variation of auroral bombardment of the atmosphere. *Roble and Rees* [1977] extended the mid-latitude diurnal model of the ionospheric *F*-region developed by *Roble* [1975] to include auroral processes and used the model to study the coupled, time-dependent ionospheric and atmospheric processes associated with auroral events. *Stamnes at el.* [1986] used this model to analyze electron and ion temperature profiles

measured by incoherent radar as a result of daytime auroral precipitation. The good agreement between computed and measured profiles leads considerable credence to this model. The global effects of the aurora (reviewed by *Rees and Fuller-Rowell*, 1991; *Killeen et al.*, 1991) have been studied with large scale 3-dimensional models such as the NCAR-TIGCM [*Roble et al.*, 1988] and the UCL-TGCM [*Fuller-Rowell and Rees*, 1980; *Fuller-Rowell et al.*, 1987]. The NCAR-TIGCM model adopts a simplified set of 8 ion-chemical and 3 recombination reactions, solves the time-independent continuity equation for O^+, including ambipolar diffusion and assumes photochemical equilibrium between N_2^+, O_2^+, O^+, N^+ and NO^+. In the above models, primary ionization rates and electron production spectra due to aurora are calculated by computationally efficient simplified schemes instead of solving the electron transport equation. *Robinson et al.* [1987] and *Fuller-Rowell and Evans* [1987] make use of energetic electron fluxes measured by instruments carried by polar orbiting satellites to derive altitude profiles of ionization rates from an energy deposition function derived by *Rees* [1963]. An effective recombination rate coefficient is adopted to determine the electron density profile, and the conductivities are computed.

The dynamic behaviour of the thermosphere is influenced by the temperature structure through the equation of state of a gas which relates temperature to pressure, and by the temperature dependence of the transport coefficients. Several reaction rate coefficients are also temperature dependent, requiring the continuity equations to be coupled with the energy equations for the electron and ion gas. Solution of the energy equations yields the electron and ion temperatures. Auroral electron temperatures have been calculated by *Rees et al.* [1967] and *Rees and Walker* [1968] by using the electron heat conduction equation with local sources and sinks. The electron energy equation applicable to the ionospheric region is derived from the Boltzmann equation by *Burgers* [1969] and *Schunk and Walker* [1970c]. *Rees et al.* [1971] studied the influence of field-aligned currents on the auroral electron temperature. *Rees and Roble* [1975] developed a model of coupled electron-ion energy equations and discussed various sources and

sinks of energy, heating and cooling rates. *Schunk and Nagy* [1978] reviewed the theory and observations relating to electron temperatures in the *F*-region of the ionosphere. Electron heating, including the origin of the stopping cross section is analyzed by *Stamnes and Rees* [1983]. The contribution of auroral precipitation to neutral and ion heating is summarized separately for auroral electrons and for ions [*Rees et al.*, 1983; *Rees*, 1987]. *Rees* [1989] reviewed extensively the neutral, ion and electron temperatures in the upper atmosphere.

In spite of the numerous studies cited above, many aspects of aurora are not yet completely understood. The objective of this thesis is to obtain a better understanding of the transport of auroral electrons from the magnetosphere to the ionosphere and the influence of the ionosphere on the characteristics of the auroral stream.

1.2 This Work

This thesis makes a start in the direction of coupling the magnetosphere and ionosphere self-consistently by introducing an electric field acceleration term and a converging magnetic field term into the collisional transport equation. A self-consistent time varying auroral model is developed by solving the electron transport equation, ion continuity equations and electron and ion energy equations self-consistently. The outline of this thesis is given below:

Chapter 2 introduces the basic theory of a self-consistent time varying auroral model. A closed set of coupled equations is derived. The baseline value of parallel electric field in the topside ionosphere, the polarization field, is discussed. I have investigated the effects of a parallel electric field, especially the self-consistent polarization electric field, and the geomagnetic mirror force on the electron distribution in the collisional medium. A new electron transport code, including elastic and inelastic collisions, the geomagnetic mirror effect and the electric field, is developed. The coupled ambipolar diffusion equations of two major ions O^+ and H^+ are derived

as well as the other minor ion continuity equations. The electron and ion energy equations are adopted and include impact electron heating, ion heating by orthogonal electric fields, and heat conduction.

Chapter 3 contains the procedure for solving the coupled electron transport equation, ion continuity equations and electron and ion energy equations. In this chapter the computational problems are simplified by using physical arguments concerning various time scales and altitude regimes. Implementation of the solution is provided for each type of equation. Boundary conditions and initial conditions are also discussed in detail.

Chapter 4 presents the numerical results for various cases. The diurnal variation of the ionosphere during non-auroral conditions is illustrated. The response of the ionosphere to different incident auroral electron spectra that may occur during daytime and night-time is investigated.

Chapter 5 discusses the effects of a parallel electric field and the magnetic mirror force on both auroral electron and photoelectron transport, as well as the response of the ionosphere to electron precipitation. New results of the Pederson and Hall conductances, based on the present auroral model, are illustrated. Comparison is made between the new results and previous work.

Chapter 6 summarizes and discusses the principal results of this thesis.

CHAPTER 2

Self-consistent Time Varying Auroral Model

The structure of the thermosphere at high latitudes is significantly affected by auroral activity, which is caused by precipitating energetic electrons and ions. These particles penetrate from the magnetosphere into the atmosphere, where they lose their energy by exciting and ionizing the neutral atoms and molecules, by dissociation of molecules, and by heating the ambient electron gas. As a consequence, the temperature and composition of the thermosphere are affected [*Schunk and Walker*, 1970c; *Hays et al.*, 1973; *Jones and Rees*, 1973; *Roble and Rees*, 1977; *Rees et al.*, 1983; *Roble and Ridley*, 1987] as well as the conductivity of the ionosphere [*Robinson et al.*, 1987; *Hardy et al.*, 1987; *Fuller-Rowell and Evans*, 1987; *Rasmussen et al.*, 1988; and *Brekke et al.*, 1988]. In turn, the affected atmospheric/ionospheric parameters may perturb the electron transport. In this coupled system, electron precipitation associated with field aligned current plays a key role, along with other processes.

The main features of the auroral model are schematically outlined in Figure (2.1). The two primary energy sources within the thermosphere are solar EUV and particle precipitation during auroral events. The solar EUV photons are absorbed in the thermosphere by photoionization and photodissociation, leading to the production of primary photoelectrons. The primary auroral electrons and/or embedded primary photoelectrons are transported in the atmosphere and produce impact ionization and secondary electrons by ionizing and exciting the neutral species. Unlike most other models (reviewed in Chapter 1) which use parameterizations to calculate the ionization rates, a new electron transport equation is derived by including the associated feedback effects generated by the polarization field and the properties of the ambient electron gas. Ion continuity equations are developed by including all the ionization sources, solar EUV, electrons,

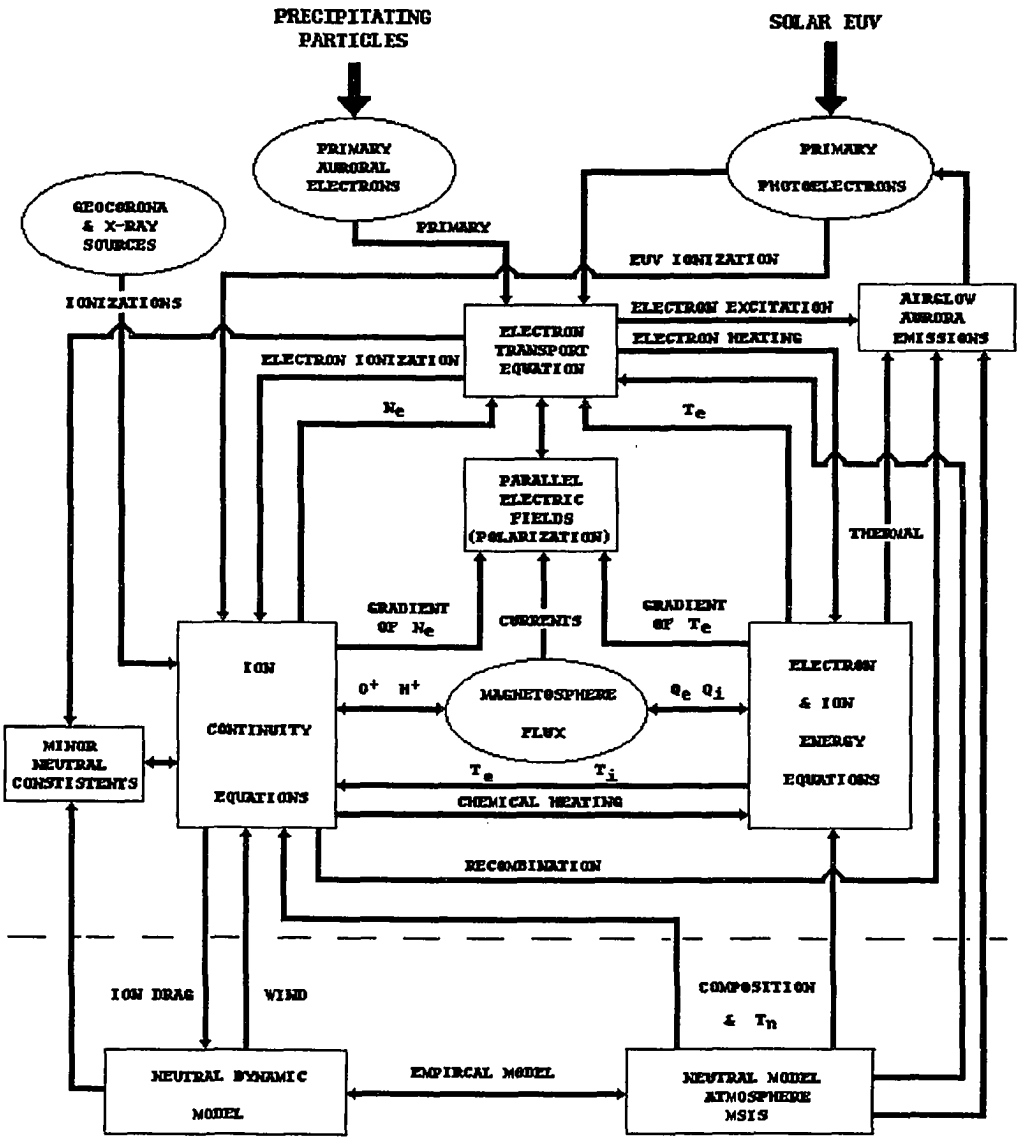

Figure 2.1 Schematic diagram of the self-consistent time varying auroral model.

solar X-rays, and geocoronal scattered EUV, chemical reactions and diffusion. Based on observations, it is assumed that O^+ and H^+ are the major ions in the topside *F*-region. The coupled ion continuity equations are derived for $O^+(^2P)$, $O^+(^2D)$, $O^+(^4S)$, O_2^+, $O_2^+(a^4\Pi)$, N_2^+, NO^+, N^+, and H^+. The energy balance process is investigated. Ambient electrons and ions are heated by energy associated with field aligned current out of the ionosphere, by thermal conduction, and by collisions with photoelectrons and auroral electrons.

The polarization field governs the field aligned transport of positive ions and electrons. An upward directed electric field in the topside ionosphere accelerates the downward moving electron flux and decelerates the upward component, thus perturbing the energy distribution of electrons.

Perturbation of the major gas constituents in the neutral atmosphere due to auroral activity is not included in this model (below the dashed line in Figure (2.1)) because the auroral model is one-dimensional along a geomagnetic field line whereas neutral dynamics can only be calculated with three-dimensional models such as those described by *Dickinson et al.* [1981], *Roble and Ridley* [1987], and *Fuller-Rowell et al.* [1987]. Global-scale winds are affected by global-scale variations in ion drag, but small horizontal-scale ionization anomalies are balanced by perturbation pressures. Therefore, once the global-scale neutral wind system is determined for a specified ion drag distribution it can be used to calculate, independently, the component along the geomagnetic field line. The major effects of neutral gas heating due to auroral processes on the neutral gas composition have been discussed by *Rees et al.* [1983] and *Hays et al.* [1973] and are included in the three-dimensional models cited above.

2.1 Parallel Electric Fields

The large difference in mass between the positive ions and electrons gives rise to a corresponding difference in the inertial force terms in the equations for the diffusion velocity. Separation of oppositely charged species is prevented, however, by the development of a polarization field that constrains the ions and electrons to drift as a single gas, thus maintaining bulk charge neutrality in the ionosphere. For most F-region applications collisional interactions dominate over field effects and Ohm's law reduces to

$$\mathbf{J} = \sigma_e \left[\mathbf{E} + \frac{kT_e}{en_e} \nabla n_e \right] + \tau_e \nabla T_e \tag{2.1}$$

where σ_e is the electrical conductivity; τ_e is the current flow conductivity due to thermal gradients at constant electron density; $\mathbf{E}$ is the polarization electric field; T_e and n_e are the electron temperature and density, respectively. In the ionosphere, the polarization field, $\mathbf{E}$, is determined by the current rather than vice versa.

$$\mathbf{E} = \frac{\mathbf{J}}{\sigma_e} - \frac{kT_e}{en_e} \nabla n_e - \frac{\tau_e}{\sigma_e} \nabla T_e \tag{2.2}$$

Polarization electric fields exist whenever there are gradients in the electron density and temperature, and field aligned currents provide an additional component of electric field. A precipitating electron flux contributes to the field aligned current not only directly but also through enhanced ionization produced by its interaction with atmospheric gases. In addition, a suprathermal electron stream heats the electron gas resulting in an increase of the electron temperature. In turn, an upward directed polarization field accelerates the downward moving electrons and decelerates the upward moving component. In this context, downward means the direction from the magnetosphere into the ionosphere along the magnetic field line; upward is in the opposite direction. The perturbed electron energy distribution results from the effects of the polarization

field on the ionospheric parameters and in turn implies a change in the polarization electric field, i.e. the physical processes are coupled. The polarization electric field represents the baseline value of parallel electric fields in the topside ionosphere.

Several processes have been proposed in the literature to show that additional parallel electric fields can be supported self-consistently under various conditions (c.f. Chapter 1). The mechanisms are anomalous resistivity, double layers, electrostatic shocks, pitch angle anisotropy, magnetic mirror effect on parallel currents, thermoelectric effects and Alfv́en waves. As the accelerated auroral electrons impinge on the atmosphere, ionization and hence the ionospheric conductivity are enhanced. In addition to the loss cone constriction on the upward field aligned current, anomalous resistivity due to current-driven instabilities can also limit the current and may lead to a potential drop along field lines [*Papadopolous*, 1977; *Stasiewicz*, 1984]. Some evidence for the existence of turbulent resistivity during auroral activity has been reported by *Volokitin et al.* [1984], using the three-component ferrosonde magnetometer onboard the Interkosmos-Bolgariya 1300 satellite at an altitude of about 850 km.

The electron acceleration mechanisms enumerated above are believed to operate well above the thermosphere. In order to close the magnetosphere-ionosphere circuit the current continuity condition requires the presence of field aligned currents. Field aligned currents in the topside ionosphere have been inferred from the perturbations that are produced in the magnetic field [*Evans et al.*, 1977; *Lanchester and Rees*, 1987]. The largest field aligned current densities in the ionosphere are associated with thin auroral arcs, especially near their edges [*Lanchester and Wallis*, 1985; *McFadden, et al.*, 1990]. *Otto and Birk* [1992] have suggested that a resistive instability operates within the ionosphere in regions of sheared magnetic field topology. This proposal is consistent with low altitude satellite borne measurements of magnetic field perturbations. The instability can grow under typical ionospheric conditions and is not damped by plasma-neutral gas frictional forces and by ionization/recombination processes. Observations of upward field

aligned ion beams and electric field reversals suggest that the low-altitude boundary of an auroral potential structure may be located below 1000 km [*Mozer*, 1980; 1981]. From the BIDARCA sounding rocket campaign, *McFadden et al.* [1990] reported a potential drop of about 400 V between the high-altitude crossing (at 950 km) and the low-altitude crossing (at 430 km) of two nearly identical payloads that traveled within 70 km of the same magnetic field line containing a narrow auroral arc. A new study of the BIDARCA data by *Boehm et al.* [1990] revealed an even stronger potential drop between the two payloads, about 2 kV. This would imply a 4 mV/m parallel electric field if the potential drop were uniformly distributed. However, *McFadden et al.* [1990] point out that the differences in the electron precipitation at the two altitudes indicates that temporal and/or longitudinal variations in the arc were large. Therefore unambiguous evidence of this potential drop could not be found in their particle data.

2.2 The Electron Transport Equation

The interaction of suprathermal electrons with the partially ionized gas in the thermosphere is described by the electron continuity equation

$$\frac{\partial f(\mathbf{r},\mathbf{v},t)}{\partial t} + \mathbf{v}\cdot\nabla_{\mathbf{r}} f(\mathbf{r},\mathbf{v},t) + \nabla_{\mathbf{v}}[\dot{\mathbf{v}} f(\mathbf{r},\mathbf{v},t)] = \left(\frac{\delta f(\mathbf{r},\mathbf{v},t)}{\delta t}\right)_{coll} \qquad (2.3)$$

For the treatment of auroral electron transport a number of approximations can be made to simplify the non-linear Boltzmann equation in order to arrive at a linear transport equation. The transit time of precipitating electrons along the magnetic field lines is short compared to changes in the atmosphere in response to electron impact. Thus, the structure of an auroral potential region is likely to be controlled by its boundary conditions and auroral electron transport is generally considered to be quasi-static. The explicit time dependence of the electron distribution function is therefore neglected ($\partial f/\partial t = 0$). For the magnetic field strength and average mean free path

in the topside ionosphere the electron gyrofrequency is much larger than the collision frequency. The transport of an individual electron can then be represented by the motion of its guiding center. Consequently, the average motion is symmetric with respect to azimuth and one-dimensional along the geomagnetic field.

The interaction of the streaming electrons with the ambient electron gas is approximated by a continuous energy loss process. The energy loss to the ambient electrons with density n_e is specified by the loss function $L(\epsilon)$ [Swartz *et al.*, 1971]. The total change in momentum is

$$m\frac{\partial \mathbf{v}}{\partial t} = -n_e L(\epsilon)\frac{\mathbf{v}}{v} + q\mathbf{E} + q\frac{\mathbf{v}\times\mathbf{B}}{c} \tag{2.4}$$

where

$$L(\epsilon) = \frac{3.37\times10^{-12}}{\epsilon^{0.94} n_e^{0.03}\left(\frac{\epsilon - T_e}{\epsilon - 0.53T_e}\right)^{2.36}} \qquad \text{cm}^{-2}\ \text{eV} \tag{2.5}$$

and T_e is the ambient electron temperature in eV, n_e is the electron density in cm^{-3} and ϵ is the energy of the incident electrons in eV. The electric field is related to the potential drop ϕ by $\mathbf{E} = -\nabla\phi$. The electron energy is $\epsilon = \frac{1}{2}mv^2 + q\phi$, and $q = -e$ for electrons.

Using equation (2.4), the third term on the left hand side of equation (2.3) becomes

$$\nabla_{\mathbf{v}}[\dot{\mathbf{v}}f] = -n_e\sum_{k=1}^{3}\left(\frac{\partial}{\partial v_k}\left[L(\epsilon)\frac{v_k}{mv}f\right]\right) - e\nabla_{\mathbf{v}}\left[\left(\mathbf{E} + \frac{\mathbf{v}\times\mathbf{B}}{c}\right)f\right]$$

Since

$$\nabla_{\mathbf{v}}\left(\mathbf{E} + \frac{\mathbf{v}\times\mathbf{B}}{c}\right) = 0$$

and

$$\sum_{k=1}^{3}\left(\frac{\partial}{\partial v_k}\left[L(\epsilon)\frac{v^2}{m}\frac{v_k}{v^3}f\right]\right) = \sum_{k=1}^{3}\left(\frac{v_k}{v^3}\frac{\partial}{\partial v_k}\left[L\epsilon\frac{v^2}{m}f\right] + L(\epsilon)\frac{v^2}{m}f\frac{\partial}{\partial v_k}\left[\frac{v_k}{v^3}\right]\right) \tag{2.6}$$

The last term in equation (2.6) vanishes because [*Stamnes and Rees*, 1983]

$$\sum_{k=1}^{3}\frac{\partial}{\partial v_k}\left[\frac{v_k}{v^3}\right] = \sum_{k=1}^{3}\left(\frac{-3v_k^2}{v^5} + \frac{1}{v^3}\right) = 0$$

Since $\partial\epsilon/\partial\mathbf{v} = m\mathbf{v}$, the loss term in equation (2.4) is transformed and the continuity equation

becomes,

$$\mathbf{v}\cdot\nabla_{\mathbf{r}}f-\frac{m}{v}n_e\frac{\partial}{\partial\epsilon}\left(\frac{v^2}{m}Lf\right)-e\left(\mathbf{E}+\frac{\mathbf{v}\times\mathbf{B}}{c}\right)\cdot\mathbf{v}\frac{\partial}{\partial\epsilon}f=\left(\frac{\delta f}{\delta t}\right)_{coll} \tag{2.7}$$

Conservation of the first adiabatic invariant requires that

$$\frac{\frac{1}{2}m\mathbf{v}_\perp^2}{B}=\frac{(\epsilon+e\phi)(1-\mu^2)}{B}=const.$$

where μ is the cosine of the pitch angle. Differentiating with respect to s, a spatial variable along the magnetic field line, yields

$$\frac{\partial\mu}{\partial s}=-\frac{(1-\mu^2)}{2\mu B}\frac{\partial B}{\partial s}+\frac{e(1-\mu^2)}{2\mu(\epsilon+e\phi)}\frac{\partial\phi}{\partial s} \tag{2.8}$$

then the first term in equation (2.7) becomes

$$\mathbf{v}\cdot\nabla_{\mathbf{r}}f=\mu v\frac{\partial f}{\partial s}-\frac{(1-\mu^2)v}{2B}\frac{\partial B}{\partial s}\frac{\partial f}{\partial\mu}-\frac{(1-\mu^2)}{2}\frac{evE}{\epsilon+e\phi}\frac{\partial f}{\partial\mu} \tag{2.9}$$

The Lorentz force does not contribute any energy to particles; the third term in equation (2.7) is, therefore

$$-e(\mathbf{E}+\frac{\mathbf{v}\times\mathbf{B}}{c})\cdot\mathbf{v}\frac{\partial}{\partial\epsilon}f=-\mu evE\frac{\partial f}{\partial\epsilon} \tag{2.10}$$

The collision term on the right hand side of the continuity equation specifies the interaction of the electrons with neutral and charged particles in the thermosphere, including elastic, excitation, dissociation, and ionization collisions. In each collision an electron is transferred between points in phase space. Defining the electron intensity $I(s,\epsilon,\mu)=v^2f(\mathbf{r},\mathbf{v},t)/m$ [*Duderstadt and Martin*, 1979], for each process k the collision term can be written in the form

$$\frac{v}{m}\left(\frac{\delta f}{\delta t}\right)_{coll}^{k}=n_j(s)\int\sigma_j^k(\epsilon')p_j^k(\epsilon'\rightarrow\epsilon,\mu'\rightarrow\mu)I(s,\epsilon',\mu')\,d\mu'-n_j(s)\sigma_j^k(\epsilon)I(s,\epsilon,\mu) \tag{2.11}$$

where n_j is the species density; p_j^k is the phase function; σ_j^k is the cross section of the kth collision process of species j. The first term on the right hand side constitutes a source of electrons for a phase space volume, the second term is a loss term.

For elastic collisions with atmospheric atoms, molecules and ions, the energy of the emitted electron ϵ is identical to the incident electron energy ϵ'. The energy loss for the excitation collisions is defined by the excitation threshold w so that $\epsilon = \epsilon' - w$. In ionization collisions a secondary electron with an energy ϵ_s is emitted. To conserve energy, the energy of the degraded primary electron ϵ_p is given by $\epsilon_p = \epsilon' - w - \epsilon_s$, where w is the sum of the ionization threshold and any additional energy required to produce an excited state of the ion. The energy of the secondary electron ϵ_s follows an energy distribution function which is given by *Rees et al.* [1969].

Electron transport is less sensitive to angular scattering in excitation and ionization collisions compared with angular scattering in elastic interactions [*Lummerzheim*, 1987]. It suffices to describe the angular distribution of the degraded primary electrons by pure forward scattering. The secondary electrons produced in ionizing collisions are emitted with, approximately, an isotropic pitch angle distribution. A suitable phase function for elastic scattering is given by the Rutherford formula with a screening parameter β:

$$p(\epsilon, \mu' \rightarrow \mu) = \frac{4\beta(1+\beta)}{(1+2\beta-\cos(\Theta))^2} \tag{2.12}$$

where Θ is the scattering angle between $\cos^{-1}\mu$ and $\cos^{-1}\mu'$.

The screening parameter β of the Rutherford phase function is discussed by *Stamnes* [1981] and *Berger et al.* [1970]

$$\beta = \begin{cases} \frac{1}{2}\frac{1}{(\frac{\epsilon}{12})^{3/4}-1} & \text{if } 12 \text{ eV} < \epsilon < 500 \text{ eV} \\ \beta_c \frac{6.22\cdot 10^{-5}}{(2+\epsilon_r)\epsilon_r} & \text{if } 500 \text{ eV} < \epsilon \end{cases} \tag{2.13}$$

where ϵ_r is the kinetic energy of the electron in units of the electron rest mass, $\epsilon_r = \epsilon / m_e c^2$, and β_c is a constant. *Lummerzheim et al.* [1989] assumed a weak energy dependence given by $\beta_c = 0.6\epsilon^{0.09}$, with ϵ given in units of keV for electron energies above 1 keV and a value of 0.6 for electron energies below 1 keV. For energies less than 12 eV isotropic scattering is assumed.

Taking into account elastic and inelastic collisions, the geomagnetic mirror effect through conservation of the first adiabatic invariant, the electric field, and the interaction with ambient electrons through the continuous slowing down approximation, the one dimensional steady-state transport equation is,

$$\begin{aligned}\mu\frac{\partial I}{\partial s} &- \frac{(1-\mu^2)}{2B}\frac{\partial B}{\partial s}\frac{\partial I}{\partial \mu} - n_e\frac{\partial (LI)}{\partial \epsilon} \\ &- \frac{eE}{2(\epsilon+e\phi)}(1-\mu^2)\frac{\partial I}{\partial \mu} - \mu eE(\epsilon+e\phi)\frac{\partial}{\partial \epsilon}\frac{I}{(\epsilon+e\phi)} \\ &= -\sum_j n_j {\sigma_j}^{tot} I + Q^{el} + Q^{ex} + Q^{ion} + Q_{photo}\end{aligned} \tag{2.14}$$

where ${\sigma_j}^{tot}$ is the sum of all loss cross sections, i.e. ${\sigma_j}^{tot} = \sum_k \sigma_j^k$; Q^{el}, Q^{ex}, Q^{ion} and Q_{photo} are the sources of elastic collision, excitation, ionization and photoionization and the summation is taken over all species j.

In order to solve this integro-differential equation for the electron intensity I as a function of the position s, energy ϵ, and cosine pitch angle μ, the electric field and magnetic field terms are treated as sources and the energy loss term is treated as an additional collision-like process. Denoting the angle between the horizontal and the magnetic field direction by α, the altitude z is given by $z = s\sin\alpha$. Substituting the scattering depth τ for the altitude z by

$$d\tau = -\sum_j \left[n_j(z)\sigma_j^{tot}(\epsilon) + n_e\frac{L(\epsilon)}{\Delta\epsilon_n}\right]\frac{dz}{\sin\alpha}$$

the transport equation is simplified to read:

$$\begin{aligned}\mu\frac{\partial I(\tau,\epsilon,\mu)}{\partial \tau} &= I(\tau,\epsilon,\mu) - \frac{\omega(\tau,\epsilon)}{2}\int_{-1}^{1} p(\epsilon,\mu'\rightarrow\mu)I(\tau,\epsilon,\mu')d\mu' \\ &+ Q_{coll}(\tau,\epsilon,\mu;I) + Q_E(\tau,\epsilon,\mu;I) + Q_B(\tau,\epsilon,\mu;I)\end{aligned} \tag{2.15}$$

where $\Delta\epsilon_n$ is the energy difference between two discrete electron energies at energy level denoted by n, α is the dip angle, and $\omega(\tau,\epsilon)$ is the single scattering albedo which is the ratio of the elastic collision frequency to the total collision frequency [*Lummerzheim*, 1987]. Q_{coll} combines

all internal sources, including locally produced photoelectrons, energy degraded electrons from inelastic collisions at higher energies, and secondary electrons from ionizing collision. Q_E and Q_B are the electric field and the inhomogeneous magnetic field terms.

Embedded primary photoelectrons and a flux at the upper boundary representing conjugate photoelectrons and/or primary auroral electrons are the two principal electron sources shown in Figure (2.1). The role of conjugate photoelectron and/or primary auroral electron fluxes as boundary conditions will be discussed in detail in Chapter 3. The energy spectrum of photoelectrons produced directly by solar photoionization of the ambient neutral particles in the atmosphere is governed by the UV photon flux, a multitude of photoionization cross sections and the neutral gas composition of the atmosphere. The production rate of photoelectrons with energy ϵ at altitude z is given by

$$Q_{photo}(z,\epsilon) = \sum_j \sum_l \sum_\lambda n_j(z)\sigma_j^{pion} b_j^{photo}(l,\lambda_{th},\lambda) I_{photo}(z,\lambda) \qquad (2.16)$$

where σ_j^{pion} is the photoionization cross section of species j and $b_j^{photo}(l,\lambda_{th},\lambda)$ is the branching ratio of the electronic state l and species j. The threshold wavelength, λ_{th}, is a function of the electronic state, l, of species, j. The intensity of the solar irradiance, $I_{photo}(z,\lambda)$, is specified by

$$I_{photo}(z,\lambda) = I_{photo}(\infty,\lambda)\exp\left(-\sum_j \sigma_j^{ptot}(\lambda) n_j(z) H_j ch(R_j,\chi)\right) \qquad (2.17)$$

where

$$H_j = \frac{kT_n}{m_j g} \qquad R_j = \frac{(R_E + z)}{H_j}$$

and $I_{photo}(\infty,\lambda)$ is the irradiance at 1 AU 'at the top of the atmosphere', which is adopted from *Hinteregger* [1981] and interpolated as a function of the $F_{10.7}$ solar flux. σ_j^{ptot} is the total absorption cross section of neutral species j. The photoionization and absorption cross sections and branching ratios are adopted from *Rees* [1989]. $n_j(z)$ is the neutral density of species j at

altitude z. m_j is the mass of the j^{th} species, g is the acceleration due to gravity, R_E is the radius of the earth, and $ch(R_j, \chi)$ is the Chapman function at solar zenith angle χ.

$$ch(R_j, \chi) = \frac{1}{n_j(z_s)H_j} \int_z^\infty n(z_s)\, dz_s$$

where z_s is the distance measured in the solar direction. The integration is along a slant column extending from a point of observation z toward the sun. To speed the calculation, the approximation to the Chapman function given by *Smith and Smith* [1972] is used:

$$ch(R_j, \chi) \approx \begin{cases} (\frac{1}{2}\pi R_j)^{\frac{1}{2}} e^{y^2} \mathrm{erfc}(y) & \text{if} \quad \chi \leq 90° \\ (2\pi R_j)^{\frac{1}{2}} \{(\sin\chi)^{\frac{1}{2}} \exp[R_j(1-\sin\chi)] - \frac{1}{2} e^{y^2} \mathrm{erfc}(y)\} & \text{if } 90° < \chi \leq 180° \end{cases} \tag{2.18}$$

where

$$y = (\frac{1}{2} R_j)^{\frac{1}{2}} \mid \cos\chi \mid$$

The energy carried by the ionizing photons may exceed the energy required for ionization, in which case the excess energy can lead to internal excitation of product ions as well as going into kinetic energy of the photoelectrons and ions. Momentum conservation shows that most of the energy is imparted to the lighter electrons. The electron energy will henceforth be specified in energy units (eV), with

$$\epsilon = hc\left(\frac{1}{\lambda} - \frac{1}{\lambda_{th}(j,l)}\right) \tag{2.19}$$

where h is Planck's constant and c is the speed of light.

2.3 Ion Chemistry and Continuity Equations

All the charged species that make up the ionosphere are produced either directly by photoionization and impact ionization of neutral atoms and molecules, or indirectly by subsequent ionic-chemical reactions. They may first radiate if produced in an excited state, or they may react locally or be transported to a different altitude level before reacting. To evaluate the ion composition as a function of time and altitude requires solution of the coupled time dependent continuity equations for all reacting species.

The continuity equation of species i with density N_i is

$$\frac{\partial N_i}{\partial t} = \eta_d^i + \eta_c^i - N_i L_c^i - \frac{\partial \Phi_i}{\partial z} \tag{2.20}$$

where η_d^i and η_c^i are, respectively, the production rates from direct ionization and from chemical reactions, L_c^i is the local chemical and radiative loss rate, and Φ_i is the flux due to ambipolar diffusion. Transport of particles from one region to another, as a consequence of non-uniform distributions in the gas, is influenced by collisions. In the thermosphere, in the presence of forces due to pressure gradients, gravitation and the polarization electric field, the ambipolar diffusion couples the transport of all ion species and the electrons, constraining both to one velocity, the ambipolar diffusion velocity. Major ion transport is governed by ambipolar diffusion while the minor ion distribution is influenced by the ambipolar drift velocity. At E-region heights transport is neglected by assuming photochemical equilibrium because photochemical time constants are fast compared to transport time constants. Above about 250 km O^+ ions are the major ions which determine the ambipolar flux. Based on observations of the H^+ ion densities sometimes being larger than those of O^+ at high altitude, it is assumed that H^+ ions satisfy the same ambipolar

flux formula as O^+. Under the assumption of a small vertical wind compared to the vertical ion drift velocity, the ambipolar flux is

$$\Phi_i = -N_i D_i \left(\frac{1}{N_i} \frac{\partial N_i}{\partial z} + \frac{\partial}{\partial z} \ln T_p + H_i \right) \tag{2.21}$$

where D_i is the ambipolar diffusion coefficient, T_p is the plasma temperature

$$T_p = \frac{(T_e + T_i)}{2}$$

and

$$H_i = \frac{m_i g}{2kT_p}$$

where m_i is the mass of species i, g is the gravitational acceleration, and k is Boltzmann's constant.

The ambipolar diffusion coefficients may be expressed in terms of the collision frequency [*Rees*, 1989]

$$D_i = \frac{kT_r}{m_i \nu_{in}} \left(1 + \frac{T_e}{T_r} \right) \tag{2.22}$$

where T_r is the reduced temperature for the ions and neutrals

$$T_r = M_R \left(\frac{T_i}{m_i} + \frac{T_n}{m_n} \right)$$

and ν_{in} is the ion-neutral collision frequency given by

$$\nu_{ij} = \frac{16}{3} \frac{n_j}{m_i} M_R \Omega_{i,j}^{(1,1)}$$

where $\Omega_{i,j}^{(1,1)}$ is the collision integral for diffusion and M_R is the reduced mass. For O^+ ions, the ambipolar diffusion coefficient has been specified by an explicit numerical expression in units

of $cm^2\ sec^{-1}$ [*Schunk and Walker*, 1970a]

$$D_{O^+} = \frac{3.02 \times 10^{17} T_p}{n(O) T_r^{\frac{1}{2}} (1.08 - 0.139P + 4.5 \times 10^{-3} P^2) + 19.9n(N_2) + 19.5n(O_2)} \qquad (2.23)$$

where $P = \log(T_r)$, and for upper F-region applications, T_r simplifies to

$$T_r = \frac{(T_i + T_n)}{2}$$

T_e, T_i and T_n are the electron, ion and neutral temperatures, respectively. For H^+ ions, one could assume that the collision integral for H^+ diffusion is the same as for O^+, in which case

$$D_{H^+} = 8.5 D_{O^+} \qquad cm^2\ sec^{-1} \qquad (2.24)$$

or use the ambipolar diffusion coefficient of H^+ given by *Schunk and Walker* [1970b]

$$D_{H^+} = \frac{2.1 \times 10^9 T_i^{\frac{5}{2}}}{n_e(\ln \Lambda - 0.961)} \qquad cm^2\ sec^{-1} \qquad (2.25)$$

where Λ is the plasma parameter

$$\Lambda = 5.84 \times 10^3 \left(\frac{T_i^3}{n_e}\right)^{\frac{1}{2}}$$

The latter formula is adopted in the present model calculations.

Combining the continuity equations and the ambipolar flux equations yields second order coupled differential equations. In order to simplify the problem, the time-dependent O^+ and H^+ continuity equations, including diffusion, are solved first. The continuity equations for O_2^+, N_2^+, N^+, and NO^+ are then solved, assuming photochemical equilibrium with respect to the O^+ and

H^+ density profiles. The coupled diffusion equations are

$$\frac{\partial n(O^+)}{\partial t} = D_{O+}\frac{\partial^2 n(O^+)}{\partial z^2} + A_{1O}\frac{\partial n(O^+)}{\partial z} + A_{2O}n(O^+) + A_{3O}n(H^+) + A_{4O} \quad (2.26)$$

$$\frac{\partial n(H^+)}{\partial t} = D_{H+}\frac{\partial^2 n(H^+)}{\partial z^2} + A_{1H}\frac{\partial n(H^+)}{\partial z} + A_{2H}n(H^+) + A_{3H}n(O^+) + A_{4H} \quad (2.27)$$

where

$$A_{1O} = \frac{\partial D_{O+}}{\partial z} + D_{O+}\left(\frac{\partial \ln T_p}{\partial z} + H_{O+}\right)$$

$$A_{1H} = \frac{\partial D_{H+}}{\partial z} + D_{H+}\left(\frac{\partial \ln T_p}{\partial z} + H_{H+}\right)$$

$$A_{2O} = \frac{\partial D_{O+}}{\partial z}\left(\frac{\partial \ln T_p}{\partial z} + H_{O+}\right) + D_{O+}\left(\frac{\partial^2 \ln T_p}{\partial z^2} + \frac{\partial H_{O+}}{\partial z}\right) - L_{O+}$$

$$A_{2H} = \frac{\partial D_{H+}}{\partial z}\left(\frac{\partial \ln T_p}{\partial z} + H_{H+}\right) + D_{H+}\left(\frac{\partial^2 \ln T_p}{\partial z^2} + \frac{\partial H_{H+}}{\partial z}\right) - L_{H+}$$

$$A_{3O} = \gamma_{20}n(O)$$

$$A_{4O} = \eta_d^{O^+} + \eta_c^{O^+}$$

$$A_{3H} = \gamma_{12}n(H)$$

$$A_{4H} = \eta_c^{H^+}$$

and

$$\eta_c^{O^+} = \gamma_{13}n(O^+(^2D))n(O) + \gamma_{19}n(N_2^+)n(O) + \gamma_{24}n(O^+(^2D))n(N_2)$$
$$+ \gamma_{25}n(O^+(^2P))n(O) + \gamma_{27}n(N^+)n(O_2) + \gamma_{28}n(N^+)n(O) + \alpha_5 n(O^+(^2D))$$
$$+ \alpha_7 n(O^+(^2P)) + A_3 n(O^+(^2P)) + A_5 n(O^+(^2D))$$

$$\eta_c^{H^+} = \gamma_{29}n(N^+)n(H)$$

$$L_{O+} = \gamma_1 n(N_2) + \gamma_2 n(O_2) + \gamma_{12}n(H) + \gamma_{21}n(NO) + \gamma_{26}n(N(^2D))$$

$$L_{H+} = \gamma_{20}n(O)$$

where γ_i, α_i and A_i are the rate coefficients for the chemical reactions and radiative decays listed in Table (2.1).

Table 2.1 Chemical reactions and rate coefficients

Reaction	Rate Coefficient
Chemical production of $O^+(^4S)$	
$O^+(^2D) + O \rightarrow O^+(^4S) + O$	$\gamma_{13} = 1.0 \times 10^{-11}$
$O^+(^2D) + e \rightarrow O^+(^4S) + e$	$\alpha_5 = 7.8 \times 10^{-8}(T_e/300)^{-0.5}$
$O^+(^2D) + N_2 \rightarrow O^+(^4S) + N_2$	$\gamma_{24} = 8.0 \times 10^{-10}$
$O^+(^2P) + O \rightarrow O^+(^4S) + O$	$\gamma_{25} = 5.2 \times 10^{-11}$
$O^+(^2P) + e \rightarrow O^+(^4S) + e$	$\alpha_7 = 4.0 \times 10^{-8}(T_e/300)^{-0.5}$
$O^+(^2P) \rightarrow O^+(^4S) + O$	$A_3 = 0.047$
$N_2^+ + O \rightarrow O^+(^4S) + N_2$	$\gamma_{19} = 1.4 \times 10^{-10}(T_R/300)^{-0.5}$
$H^+ + O \rightarrow O^+(^4S) + H$	$\gamma_{20} = \gamma_{12}(8/9)[(T_i + T_n/4)/(T_n + T_i/16)]^{0.5}$
$N^+ + O_2 \rightarrow O^+(^4S) + NO$	$\gamma_{27} = 3.0 \times 10^{-11}$
Chemical loss of $O^+(^4S)$	
$O^+(^4S) + O_2 \rightarrow O_2^+ + O$	$\gamma_2 = 2.0 \times 10^{-11}(T_R/300)^{-0.4}$
$O^+(^4S) + N_2 \rightarrow NO^+ + N(^4S)$	$\gamma_1 = 5.0 \times 10^{-13}, T_R < 1000K$
	$= 4.5 \times 10^{-14}(T_R/300)^2, T_R > 1000K$
$O^+(^4S) + NO \rightarrow NO^+ + O$	$\gamma_{21} = 8.0 \times 10^{-13}$
$O^+(^4S) + H \rightarrow H^+ + O$	$\gamma_{12} = 6.0 \times 10^{-10}$
$O^+(^4S) + N(^2D) \rightarrow N^+ + O$	$\gamma_{26} = 1.3 \times 10^{-10}$
Chemical production of $O^+(^2D)$	
$O^+(^2P) + e \rightarrow O^+(^2D) + e$	$\alpha_8 = 1.5 \times 10^{-7}(T_e/300)^{-0.5}$
$O^+(^2P) \rightarrow O^+(^2D)$	$A_4 = 0.171$
Chemical loss of $O^+(^2D)$	
$O^+(^2D) + N_2 \rightarrow N_2^+ + O$	$\gamma_3 = 8.0 \times 10^{-10}$
$O^+(^2D) + O \rightarrow O^+(^4S) + O$	$\gamma_{13} = 1.0 \times 10^{-11}$
$O^+(^2D) + e \rightarrow O^+(^4S) + e$	$\alpha_5 = 7.8 \times 10^{-8}(T_e/300)^{-0.5}$
$O^+(^2D) + O_2 \rightarrow O_2^+ + O$	$\gamma_{22} = 7.0 \times 10^{-10}$
$O^+(^2D) \rightarrow O^+(^4S)$	$A_5 = 7.7 \times 10^{-5}$
$O^+(^2D) + N \rightarrow N^+ + O$	$\gamma_{32} = 7.5 \times 10^{-11}$
Chemical production of $O^+(^2P)$	
No sources	
Chemical loss of $O^+(^2P)$	
$O^+(^2P) + N_2 \rightarrow N_2^+ + O$	$\gamma_9 = 4.8 \times 10^{-10}$
$O^+(^2P) + N_2 \rightarrow N^+ + NO$	$\gamma_{30} = 1.0 \times 10^{-10}$
$O^+(^2P) + N \rightarrow N^+ + O$	$\gamma_{31} = 1.0 \times 10^{-10}$
$O^+(^2P) + O \rightarrow O^+(^4S) + O$	$\gamma_{25} = 5.2 \times 10^{-11}$
$O^+(^2P) + e \rightarrow O^+(^4S) + e$	$\alpha_7 = 4.0 \times 10^{-8}(T_e/300)^{-0.5}$
$O^+(^2P) + e \rightarrow O^+(^4D) + e$	$\alpha_8 = 1.5 \times 10^{-7}(T_e/300)^{-0.5}$
$O^+(^2P) \rightarrow O^+(^4S)$	$A_3 = 0.047$
$O^+(^2P) \rightarrow O^+(^4D)$	$A_4 = 0.171$

Table 2.1 (continued)

Reaction	Rate Coefficient
Chemical production of H^+	
$O^+(^4S) + H \rightarrow H^+ + O$	$\gamma_{12} = 6.0 \times 10^{-10}$
$N^+ + H \rightarrow H^+ + N$	$\gamma_{29} = 3.6 \times 10^{-12}$
Chemical loss of H^+	
$H^+ + O \rightarrow O^+(^4S) + H$	$\gamma_{20} = \gamma_{12}(8/9)[(T_i + T_n/4)/(T_n + T_i/16)]^{0.5}$
Chemical production of N^+	
$O^+(^4S) + N(^2D) \rightarrow N^+ + O$	$\gamma_{26} = 1.3 \times 10^{-10}$
$O_2^+ + N(^2D) \rightarrow N^+ + O_2$	$\gamma_{17} = 2.5 \times 10^{-10}$
$O^+(^2P) + N_2 \rightarrow N^+ + NO$	$\gamma_{30} = 1.0 \times 10^{-10}$
$O^+(^2P) + N \rightarrow N^+ + O$	$\gamma_{31} = 1.0 \times 10^{-10}$
$O^+(^2D) + N \rightarrow N^+ + O$	$\gamma_{32} = 7.5 \times 10^{-11}$
Chemical loss of N^+	
$N^+ + O_2 \rightarrow NO^+ + O$	$\gamma_{10} = 2.6 \times 10^{-10}$
$N^+ + O_2 \rightarrow N(^4S) + O_2^+$	$\gamma_{11} = 1.1 \times 10^{-10}$
$N^+ + O_2 \rightarrow N(^2D) + O_2^+$	$\gamma_{33} = 2.0 \times 10^{-10}$
$N^+ + O_2 \rightarrow O^+ + NO$	$\gamma_{27} = 3.0 \times 10^{-10}$
$N^+ + O \rightarrow O^+(^4S) + +N$	$\gamma_{28} = 5.0 \times 10^{-13}$
$N^+ + H \rightarrow H^+ + N$	$\gamma_{29} = 3.6 \times 10^{-12}$
Chemical production of N_2^+	
$O_2^+(a^4\Pi) + N_2 \rightarrow N_2^+ + O_2$	$\gamma_6 = 2.5 \times 10^{-10}$
$O^+(^2D) + N_2 \rightarrow N_2^+ + O$	$\gamma_3 = 8.0 \times 10^{-10}$
$O^+(^2P) + N_2 \rightarrow N_2^+ + O$	$\gamma_9 = 4.8 \times 10^{-10}$
Chemical loss of N_2^+	
$N_2^+ + O_2 \rightarrow O_2^+ + N_2$	$\gamma_5 = 5.0 \times 10^{-11}(T_R/300)^{-0.8}$
$N_2^+ + O \rightarrow NO^+ + N(^2D)$	
$N_2^+ + O \rightarrow NO^+ + N(^2S)$	$\gamma_4 = 1.4 \times 10^{-10}(T_R/300)^{-0.44}$
$N_2^+ + e \rightarrow N(^2D) + N(^2D)$	$\alpha_2 = 1.8 \times 10^{-10}(T_e/300)^{-0.39}$
$N_2^+ + O \rightarrow O^+(^4S) + N_2$	$\gamma_{19} = 1.0 \times 10^{-11}(T_R/300)^{-0.23}$
$N_2^+ + NO \rightarrow NO^+ + N_2$	$\gamma_{18} = 3.3 \times 10^{-10}$
Chemical production of O_2^+	
$O^+(^4S) + O_2 \rightarrow O_2^+ + O$	$\gamma_2 = 2.0 \times 10^{-11}(T_R/300)^{-0.4}$
$O^+(^2D) + O_2 \rightarrow O_2^+ + O$	$\gamma_{22} = 7.0 \times 10^{-10}$
$N^+ + O_2 \rightarrow N(^4S) + O_2^+$	$\gamma_{11} = 1.1 \times 10^{-10}$
$N^+ + O_2 \rightarrow N(^2D) + O_2^+$	$\gamma_{33} = 2.0 \times 10^{-10}$
$N_2^+ + O_2 \rightarrow O_2^+ + N_2$	$\gamma_5 = 5.0 \times 10^{-11}(T_R/300)^{-0.8}$
$O_2^+(a^4\Pi) + O \rightarrow O_2^+ + O$	$\gamma_7 = 1.0 \times 10^{-10}$
$O_2^+(a^4\Pi) \rightarrow O_2^+$	$A_8 = 1.0 \times 10^{-4}$

Table 2.1 (continued)

Reaction	Rate Coefficient
Chemical loss of O_2^+	
$O_2^+ + e \rightarrow O(^1D) + O(^3P)$	$\alpha_1 = 1.9 \times 10^{-7}(T_e/300)^{-0.5}$
$O_2^+ + N(^2D) \rightarrow N^+ + O_2$	$\gamma_{17} = 2.5 \times 10^{-10}$
$O_2^+ + N(^2S) \rightarrow NO^+ + O$	$\gamma_{16} = 1.8 \times 10^{-10}$
$O_2^+ + NO \rightarrow NO^+ + O_2$	$\gamma_{15} = 4.4 \times 10^{-10}$
$O_2^+ + N_2 \rightarrow NO^+ + NO$	$\gamma_8 = 5.0 \times 10^{-16}$
Chemical production of $O_2^+(a^4\Pi)$	
No sources	
Chemical loss of $O_2^+(a^4\Pi)$	
$O_2^+(a^4\Pi) + N_2 \rightarrow N_2^+ + O_2$	$\gamma_6 = 2.5 \times 10^{-10}$
$O_2^+(a^4\Pi) + O \rightarrow O_2^+ + O$	$\gamma_7 = 1.0 \times 10^{-10}$
$O_2^+(a^4\Pi) + e \rightarrow O + O$	$\alpha_4 = 1.0 \times 10^{-7}$
$O_2^+(a^4\Pi) \rightarrow O_2^+$	$A_8 = 1.0 \times 10^{-4}$
Chemical production of NO^+	
$N_2^+ + O \rightarrow NO^+ + N(^2D)$	
$N_2^+ + O \rightarrow NO^+ + N(^2S)$	$\gamma_4 = 1.4 \times 10^{-10}(T_R/300)^{-0.44}$
$N^+ + O_2 \rightarrow NO^+ + O$	$\gamma_{10} = 2.6 \times 10^{-10}$
$O^+(^4S) + N_2 \rightarrow NO^+ + N(^4S)$	$\gamma_1 = 5.0 \times 10^{-13}, T_R < 1000K$
	$= 4.5 \times 10^{-14}(T_R/300)^2, T_R > 1000K$
$O^+(^4S) + NO \rightarrow NO^+ + O$	$\gamma_{21} = 8.0 \times 10^{-13}$
$N_2^+ + NO \rightarrow NO^+ + N_2$	$\gamma_{18} = 3.3 \times 10^{-10}$
$O_2^+ + N(^2S) \rightarrow NO^+ + O$	$\gamma_{16} = 1.8 \times 10^{-10}$
$O_2^+ + NO \rightarrow NO^+ + O_2$	$\gamma_{15} = 4.4 \times 10^{-10}$
$O_2^+ + N_2 \rightarrow NO^+ + NO$	$\gamma_8 = 5.0 \times 10^{-16}$
Chemical loss of NO^+	
$NO^+ + e \rightarrow O + N$	$\alpha_3 = 4.2 \times 10^{-7}(T_e/300)^{-0.85}$

As mentioned previously, it is assumed that in the topside ionosphere O^+ and H^+ are the dominant diffusing ions and that N^+, O_2^+, N_2^+, and NO^+ are the minor ions. At low altitude the chemical lifetime controls the ion densities. Photochemical equilibrium between O^+, H^+ and

N^+ yields

$$n(O^+(^4S)) = \frac{L_{N^+}P_{O^+} + [\gamma_{27}n(O) + \gamma_{29}n(H)]P_{N^+}}{[L_{O^+} - \gamma_{12}n(H)]L_{N^+} - [\gamma_{27}n(O_2) + \gamma_{29}n(H)]\gamma_{26}n(N(^2D))}$$
$$n(H^+) = \frac{\gamma_{12}n(H)L_{N^+} + \gamma_{26}n(N(^2D))}{\gamma_{20}n(O)L_{N^+}}n(O^+(^4S)) + \frac{\gamma_{29}n(H)}{\gamma_{20}n(O)}\frac{P_{N^+}}{L_{N^+}} \quad (2.28)$$

where

$$\begin{aligned}
P_{O^+} &= \gamma_{13}n(O^+(^2D))n(O) + \gamma_{19}n(N_2^+)n(O) + \gamma_{24}n(O^+(^2D))n(N_2) \\
&\quad + \gamma_{25}n(O^+(^2P))n(O) + \gamma_{27}n(N^+)n(O_2) + \gamma_{28}n(N^+)n(O) + \alpha_5 n(O^+(^2D)) \\
&\quad + \alpha_7 n(O^+(^2P)) + A_3 n(O^+(^2P)) + A_5 n(O^+(^2D)) + \eta_d^{O^+} \\
P_{N^+} &= \gamma_{17}n(O_2^+)n(N_2) + \gamma_{30}n(O^+(^2P))n(N_2) + \gamma_{31}n(O^+(^2P))n(N) \\
&\quad + \gamma_{32}n(O^+(^2D))n(N) + \eta_d^{N^+} \\
L_{O^+} &= \gamma_1 n(N_2) + \gamma_2 n(O_2) + \gamma_{12}n(H) + \gamma_{21}n(NO) + \gamma_{26}n(N(^2D)) \\
L_{N^+} &= (\gamma_{10} + \gamma_{11} + \gamma_{27} + \gamma_{33})n(O_2) + \gamma_{28}n(O) + \gamma_{29}n(H)
\end{aligned}$$

For the coupled diffusion equations of O^+ and H^+, a flux condition is applied at the upper boundary, corresponding to ion outflow, and photochemical equilibrium is adopted at the lower boundary. Once the O^+ and H^+ distributions are determined the equation for N^+ is solved assuming photochemical equilibrium with the O^+ and H^+ distributions

$$n(N^+) = \frac{P_{N^+}}{L_{N^+}} + \frac{\gamma_{26}n(N(^2D))}{L_{N^+}}n(O^+(^4S)) \quad (2.29)$$

In the altitude region of interest negative ions are unimportant, reducing the charge neutrality condition to the electron density being equal to the sum of all positive ion densities. Based on

chemical balance, a quartic equation can be derived for the electron density:

$$a_4 n_e^4 + a_3 n_e^3 + a_2 n_e^2 + a_1 n_e + a_0 = 0 \tag{2.30}$$

where

$$n_e = n(\mathrm{O}^+) + n(\mathrm{H}^+) + n(\mathrm{N}^+) + n(\mathrm{O}_2^+(a^4\Pi)) + n(\mathrm{N}_2^+) + n(\mathrm{O}_2^+) + n(\mathrm{NO}^+)$$

$$a_0 = -ACE - DHF - BEF - CDG$$

$$a_1 = -\alpha_3(KEC + DC + HD + BE) - \alpha_1(AE + GD) - \alpha_2(AC + FB)$$

$$a_2 = \alpha_3(EC - \alpha_1 KE - \alpha_2 KC - \alpha_1 D - \alpha_2 B) - \alpha_1\alpha_2 A$$

$$a_3 = \alpha_3(\alpha_2 C + \alpha_1 E - \alpha_1\alpha_2 K)$$

$$a_4 = \alpha_1\alpha_2\alpha_3$$

$$A = \gamma_1 n(\mathrm{O}^+(^4\mathrm{S}))n(\mathrm{N}_2) + \gamma_{10} n(\mathrm{N}^+)n(\mathrm{O}_2) + \gamma_{21} n(\mathrm{O}^+(^4\mathrm{S}))n(\mathrm{NO}) + \eta_d^{NO^+}$$

$$B = \gamma_2 n(\mathrm{O}^+(^4\mathrm{S}))n(\mathrm{O}_2) + \gamma_7 n(\mathrm{O}_2^+(\mathrm{a}^4\Pi))n(\mathrm{O}) + \gamma_{11} n(\mathrm{N}^+)n(\mathrm{O}_2)$$
$$+ \gamma_{22} n(\mathrm{O}^+(^2\mathrm{D}))n(\mathrm{O}_2) + \gamma_{33} n(\mathrm{N}^+)n(\mathrm{O}_2) + A_8 n(\mathrm{O}_2^+(\mathrm{a}^4\Pi)) + \eta_d^{O_2^+}$$

$$C = \gamma_8 n(\mathrm{N}_2) + \gamma_{15} n(\mathrm{NO}) + \gamma_1 6 n(\mathrm{N}(^4\mathrm{S})) + \gamma_{17} n(\mathrm{N}(^2\mathrm{D}))$$

$$D = \gamma_3 n(\mathrm{O}^+(^2\mathrm{D}))n(\mathrm{N}_2) + \gamma_6 n(\mathrm{O}_2^+(\mathrm{a}^4\Pi))n(\mathrm{N}_2) + \gamma_9 n(\mathrm{O}^+(^2\mathrm{P}))n(\mathrm{N}_2) + \eta_d^{N_2^+}$$

$$E = \gamma_4 n(\mathrm{O}) + \gamma_5 n(\mathrm{O}_2) + \gamma_{18} n(\mathrm{NO}) + \gamma_{19} n(\mathrm{O})$$

$$F = \gamma_8 n(\mathrm{N}_2) + \gamma_{15} n(\mathrm{NO}) + \gamma_{16} n(\mathrm{N})$$

$$G = \gamma_4 n(\mathrm{O}) + \gamma_{18} n(\mathrm{NO})$$

$$H = \gamma_5 n(\mathrm{O}_2)$$

$$K = n(\mathrm{O}^+) + n(\mathrm{H}^+) + n(\mathrm{N}^+) + n(\mathrm{O}_2^+(a^4\Pi))$$

Solving this equation yields the electron density. Once n_e is known, the densities of N_2^+, O_2^+ and

NO^+ can be determined from the continuity equations:

$$
\begin{aligned}
n(N_2^+) &= \frac{D}{E + \alpha_2 n_e} \\
n(O_2^+) &= \frac{H n(N_2^+) + B}{C + \alpha_1 n_e} \\
n(NO^+) &= \frac{A + F n(O_2^+) + G n(N_2^+)}{\alpha_3 n_e}
\end{aligned}
\tag{2.31}
$$

The chemical production and local loss processes for each species included in the formulation are listed in Table (2.1). A detailed derivation of equation (2.30) is given in Appendix A.

There are two production sources, η_d and η_c, in the continuity equations. η_d is the production rate from direct ionization by electrons and photons. Four possible direct ionization sources are considered:

1) Solar EUV photoionization. During daytime, solar EUV radiation incident upon the Earth's atmosphere causes photoionization of the atmospheric constituents producing primary photoelectrons.

2) Solar X-ray ionization. This is an important ionization source at low altitudes in the E-region during the day-time because solar X-rays penetrate deep into the atmosphere to ionize the neutral constituents.

3) Geocoronal ionization. Solar EUV radiation is scattered by the Earth's extended atmosphere. The scattered radiation, named the geocorona, is a source of global ionization. The geocoronal ionization is a very important source for maintaining the night time ionization rate.

The above three ionization sources are produced by photons. The photoionization rate of species j at altitude z is

$$
\eta_d^{photo}{}_j(z) = n_j(z) \int_{\lambda_{th}}^{0} I_{photo}(z, \lambda) \sigma_j^{Pion}(\lambda) b_j^{photo}(\lambda, l) d\lambda \tag{2.32}
$$

where I_{photo} is the photon intensity, $\sigma_j^{Pion}(\lambda)$ is the ionization cross section, $b_j^{photo}(\lambda, l)$ is the branching ratio that identifies production of ions in various electronic states, l. For each con-

stituent, the sum over l of $p_j^{photo}(\lambda, l)$ equals 1. The solar irradiance and photon cross sections listed in appendix 2 of *Rees* [1989] are adopted in this work.

4) Electron impact ionization. Precipitating energetic electrons which are either primary auroral electrons or electrons from the conjugate hemisphere may be present at the upper boundary. Due to the existence of several energetically accessible states and the complex structure of the solar ultraviolet radiation spectrum, most of the primary photoelectrons have sufficient energy to excite or ionize further the neutral atmospheric constituents. By means of elastic and inelastic collisions the photoelectrons are transported along magnetic field lines, lose energy and are eventually thermalized. Therefore, photoelectrons are included in the electron transport calculation as an embedded source term. Impact electron ionization is a function of the neutral densities $n_j(z)$ and the electron intensity $I(z, \epsilon, \mu)$,

$$\eta_d^{ion}{}_j(z) = n_j(z) \int_{\epsilon_0}^{\infty} \int_{-1}^{1} \sigma_j^{ion}(\epsilon) I(z, \epsilon, \mu)\, d\epsilon\, d\mu \tag{2.33}$$

In the present model, production of species O^+, O_2^+, N_2^+, N^+ and NO^+ by direct ionization are calculated. Since the production of H^+ by electron and photon impact on hydrogen is small, the principal source of H^+ is charge exchange between H and O^+. Atomic nitrogen ions can also be produced by direct electron impact on N, but the contribution from this source is negligible because of the small abundance of this atomic species. The branching ratios 0.4, 0.4 and 0.2 for O^+ states $O^+(^4S)$, $O^+(^2D)$ and $O^+(^2P)$, are obtained from *Burnett and Roundtree* [1979], and 0.63 and 0.37 are used for $O_2^+(X^2\Pi)$, $O_2^+(a^4\Pi)$ [*Watson et al.*, 1967], respectively.

2.4 Electron and Ion Energy Equations

Temperature is the observable parameter in the energy balance of the thermosphere. It is important to understand the physical processes that underlie the energetics of the region and thereby control the altitude profiles of the temperatures of various species of particles. In addition, temperature influences processes other than those associated with energetics such as chemical reactions and transport through the reaction rate coefficients shown in Table (2.1) and the transport coefficients. In addition to sources and sinks of energy, the temperature profiles in the atmosphere are influenced by energy transport processes. The electron energy equation applicable to the ionospheric region is derived from the Boltzmann equation given by *Burgers* [1969]. Neglecting the thermal effects of chemical reactions and viscosity, the equation for the conservation of energy becomes

$$\frac{3}{2}k\frac{D}{Dt}(n_eT_e) = -\frac{5}{2}n_ekT_e\nabla\cdot\mathbf{V}_e - \nabla\cdot\mathbf{q}_e + Q_J + Q_e - L_e \qquad (2.34)$$

where

$$\frac{D}{Dt} = \frac{\partial}{\partial t} + \mathbf{V}\cdot\nabla$$

and where $\mathbf{V}_e$ is the electron drift velocity, which can be expressed in terms of the current $\mathbf{J}$,

$$\mathbf{V}_e = -\frac{\mathbf{J}}{|e|n_e}$$

k is Boltzmann's constant, n_e is the electron number density, T_e is the electron gas temperature, $\mathbf{q}_e$ is the heat flow vector , Q_J is the local rate of heating due to Joule current dissipation. Q_e is the local electron heating by secondary electrons, and L_e is the local electron cooling rate.

The electric current and the electron heat flow are essentially the same as the total current and the total heat flow. The heat flow vector is related to the electric current and to gradients in

electron temperature by [*Schunk and Walker*, 1970c]

$$\mathbf{q} = \zeta \mathbf{J} - K^e \nabla T_e \tag{2.35}$$

where $\zeta = \mu_e/\sigma_e$, $K^e = K - \mu_e \tau_e/\sigma_e$, μ_e is the heat flow conductivity due to an electric field, σ_e and τ_e have already been defined. K^e is the electron thermal conductivity in the limit of zero current.

The time required for auroral electrons to penetrate the atmosphere and heat the ambient electrons is short compared to changes in the host medium in response to electron impact. This justifies assuming a steady state in the electron energy equation. The reverse current in the ionosphere can be equated to the current carried by the bombarding flux at all altitudes [*Rees et al.*, 1971], which is of the order of 10^{-6} Am^{-2}. The contribution of thermoelectric transport is negligible compared to the thermal conduction. Therefore, neglecting the terms relative to the currents, the electron energy equation becomes

$$\sin^2 \alpha \frac{\partial}{\partial z}\left[K^e \frac{\partial T_e}{\partial z}\right] + Q_e - L_e = 0 \tag{2.36}$$

where α is the magnetic dip angle. For the temperature range normally encountered in auroral arcs the electron thermal conductivity is expressed as [*Rees and Roble*, 1975]

$$K^e = \frac{7.5 \times 10^5 T_e^{\frac{5}{2}}}{1 + 3.22 \times 10^4 \frac{T_e^2}{N_e} \sum_j n_j \bar{Q}_j} \qquad \mathrm{eV\ cm^{-1}\ s^{-1} deg^{-1}} \tag{2.37}$$

where $\bar{Q}_j$ is the average momentum transfer cross section, and the summation is over the neutral species n_j.

The principal source of energy in the thermosphere is the absorption of solar UV radiation. The embedded energetic photoelectrons due to photoionization of solar EUV radiation lose energy by collisions with the ambient electron gas as well as to the neutral gas. At high altitudes there is a substantial, but variable, contribution from the dissipation of electric currents driven

by electric fields of magnetospheric origin, and from the absorption of energetic particles associated with the aurora. Precipitating heavy ions, protons and O^+, usually contribute only a small fraction of the total energy deposited in the thermosphere. It is only through the production of electrons by ionization that protons can appreciably heat the electron gas. Here, the heat source due to heavy particles is not included. Occasionally, however, the auroral proton energy flux becomes the dominant heat source at night. As discussed in section 2.2, auroral electron and photoelectron transport along magnetic field lines has been considered by treating the photoelectrons as an embedded source and the conjugate photoelectrons and/or primary auroral electron flux as external sources. The change of momentum due to collisional interactions between superthermal electrons and ambient electrons and by Cerenkov wave radiation can be approximated by a continuous energy loss process, which is specified by the analytic function $L(\epsilon)$ given by equation (2.5). The heating rate due to the superthermal electrons is, therefore,

$$Q_e = n_e(z) \int_{\epsilon_t}^{\infty} \int_{-1}^{1} L(\epsilon) I(z, \epsilon, \mu)\, d\epsilon\, d\mu \tag{2.38}$$

where $I(z, \epsilon, \mu)$ is the superthermal electron intensity which is the solution of the electron transport equation as a function of the altitude z, energy ϵ, and cosine pitch angle μ. ϵ_t is the thermal energy.

In the ionosphere, there exist large scale electric fields directed perpendicular to the geomagnetic field that are generated in the magnetosphere by the interaction between the solar wind and the geomagnetic field. The orthogonal electric fields map to the ionosphere along the highly conducting geomagnetic field lines. Under the action of such an electric field, charged particles drift relative to one another and relative to neutral particles. Collisions between species limit the drift velocities and convert some of the drift energy into thermal energy. The ion gyrofrequency is smaller than the electron gyrofrequency by the inverse of their mass ratio, allowing ionospheric

ions to drift orthogonal to the magnetic field more readily than electrons. The ratio of their heating rates is roughly proportional to the ratio of their respective masses. Consequently, the heating by perpendicular electric fields is important for ions but not for electrons. In this model, the perpendicular electric field heating for electrons is neglected. However, the effect of a weak parallel electric field in the electron energy equation and the effect of perpendicular electric fields in the ion energy equation are taken into account.

There are a number of processes that are effective in cooling the electron gas. In the lower F-region, where the molecular species are abundant, rotational excitation of N_2 and O_2 and excitation of the fine structure levels of atomic oxygen are the most important cooling processes. At electron temperatures greater than 1500°K, vibrational excitation of N_2 and O_2 and electronic excitation of O and O_2 have to be included. At high altitudes, Coulomb collisions with the ambient ions are an important energy loss mechanism for superthermal electrons, and in some cases elastic collisions with the ambient neutrals have to be considered. All of the following cooling rates and heating rates have units of eV cm^{-3} s^{-1}.

In the ionosphere the ambient electrons are generally hotter than the ions and will therefore lose energy to the ions through Coulomb collisions. For the case in which the ions are assumed to have a common temperature, the expression is [*Rees and Roble*, 1975]

$$L_{ei} = 3.2 \times 10^{-8} n_e \left(\frac{\ln \Lambda}{T_e^{\frac{3}{2}}} \right) (T_e - T_i) \cdot [n(O^+) + 16n(H^+) + 0.50n(O_2^+) + 0.53n(NO^+)] \tag{2.39}$$

The energy loss rates for elastic collisions between electrons and various neutral species are

$$\begin{aligned} L_e(e, N_2) &= 1.77 \times 10^{-19} n_e n(N_2)(1 - 1.21 \times 10^{-4} T_e) T_e (T_e - T_n) \\ L_e(e, O_2) &= 1.21 \times 10^{-18} n_e n(O_2)(1 + 3.6 \times 10^{-2} T_e) T_e^{\frac{1}{2}} (T_e - T_n) \\ L_e(e, O) &= 3.74 \times 10^{-18} n_e n(O) T_e^{\frac{1}{2}} (T_e - T_n) \\ L_e(e, H) &= 9.63 \times 10^{-16} n_e n(H)(1 - 1.35 \times 10^{-4} T_e) T_e^{\frac{1}{2}} (T_e - T_n) \end{aligned} \tag{2.40}$$

The rate at which electrons lose energy in exciting rotational bands of molecular nitrogen

and molecular oxygen are [*Rees and Roble*, 1975]

$$\begin{aligned} L_e(e, \mathrm{N}_2(rot)) &= 2.9 \times 10^{-14} n_e n(\mathrm{N}_2) T_e^{\frac{1}{2}} (T_e - T_n) \\ L_e(e, \mathrm{O}_2(rot)) &= 6.9 \times 10^{-14} n_e n(\mathrm{O}_2) T_e^{\frac{1}{2}} (T_e - T_n) \end{aligned} \tag{2.41}$$

Electron energy loss due to excitation of vibrational bands in molecular nitrogen is an important cooling process. Electron cooling by vibrational excitation of molecular oxygen dominates in the lower thermosphere. The expressions for the electron loss due to vibrational excitation of N_2 and O_2 are [*Rees and Roble*, 1975; *Roble*, private communication, 1991]

$$\begin{aligned} L_e(e, \mathrm{O}_2(vib)) &= 3.125 \times 10^{-21} n_e n(\mathrm{O}_2) T_e^2 (T_e - T_n) \\ L_e(e, \mathrm{N}_2(vib)) &= 1.3 \times 10^{-4} n_e n(\mathrm{N}_2) \Big\{ A_\nu \left[1 - \exp\left(\frac{3200}{T_e} - \frac{3200}{T_n} \right) \right] \\ &\quad + \left[7.6 \times 10^{-16} T_e + 2.0 \times 10^{-10} T_e^{-\frac{1}{2}} \right] (T_e - T_n) \Big\} \end{aligned} \tag{2.42}$$

where

$$A_\nu = \begin{cases} 2.53 \times 10^{-6} T_e^{\frac{1}{2}} \exp(-17620.0/T_e) & T_e \geq 2000^\circ \mathrm{K} \\ 2.0 \times 10^{-7} \exp(-4605.2/T_e) & 1000^\circ \mathrm{K} < T_e > 2000^\circ \mathrm{K} \\ 5.71 \times 10^{-7} \exp(-3352.6/T_e) & T_e \leq 1000^\circ \mathrm{K} \end{cases}$$

At high electron temperatures the population in the high-energy tail of the Maxwellian electron energy distribution is sufficiently large to cause appreciable excitation of the ^{1}D level of atomic oxygen. The cooling rate due to this excitation is

$$\begin{aligned} L_e(e, \mathrm{O}(^1\mathrm{D})) &= 1.07 \times 10^{-10} n_e n(\mathrm{O}) T_e^{\frac{1}{2}} \exp(-2.27 \times 10^4 / T_e) \\ &\quad \cdot \Big[0.406 + 0.357 \times 10^{-4} T_e \\ &\quad - (0.333 + 0.183 \times 10^{-4} T_e) \exp(-1.37 \times 10^4 / T_e) \\ &\quad - (0.456 + 0.174 \times 10^{-4} T_e) \exp(-2.97 \times 10^4 / T_e) \Big] \end{aligned} \tag{2.43}$$

The energy loss arising from electron-impact-induced transitions among the fine structure levels of atomic oxygen is the dominant cooling mechanism over a wide range of electron temperatures in the F-region. Based on theoretical calculations, an analytic expression has been

formulated for use in a large thermospheric circulation model by *Roble* [private communication, 1991]

$$L_e(e,\mathrm{O})_f = 3.4 \times 10^{-12} n_e n(\mathrm{O}) \left(\frac{T_e}{T_n} - 1\right) \cdot [1 - 7 \times 10^{-5} T_e] \left(\frac{150}{T_e} + 0.40\right) \tag{2.44}$$

At low altitudes, electron thermal conduction is unimportant and the electron temperature is determined by a balance between local heating and cooling rates. The altitude range in which local processes dominate depends upon the ionospheric and atmospheric conditions. For example, for daytime solar minimum conditions, local energy equilibrium may apply only below about 150 km, while for daytime solar maximum conditions it might apply to altitudes as high as 300 km [*Schunk and Nagy*, 1978]. Here, local equilibrium is assumed below 150 km. The temperature calculated from local energy balance is used as the lower boundary condition for equation (2.36). A heat flux is applied as the upper boundary condition to represent the heat flowing in the electron gas from the magnetosphere to the ionosphere [*Rees and Roble*, 1975].

Other than heating by perpendicular electric fields, discussed previously, and by chemical reactions, the main heat source for the ions is Coulomb collisions with the ambient electrons. The ions, in turn, are cooled by collision with neutral particles. Different species of positive ions are heated and cooled by different collisional processes, resulting in somewhat different temperatures for various species. Because the energy exchange in ion-ion collisions is highly efficient, it is sufficient to characterize the ionic energy distribution by a single ion temperature. Here, it is assumed that the ions have one common temperature. The other possible sources of ion thermal energy such as dissipation of wave energy and chemical reactions are neglected and local energy equilibrium is assumed. The ion energy equation is

$$Q_{ie} + Q_{E_\perp} - L_{in} = 0 \tag{2.45}$$

where Q_{ie} is the ion heating rate by Coulomb collisions with the hotter electrons, given by L_{ei}

in equation (2.36). $Q_{E_\perp}$, the ion heating rate by a perpendicular electric field, is

$$Q_{E_\perp} = \sigma_p E_\perp^{*2} \tag{2.46}$$

where σ_p is the Pederson conductivity. $E_\perp^*$ is the magnitude of the perpendicular electric field felt by an observer moving with the neutral gas. In the present one dimensional model, the horizontal electric field components are not included. Therefore, values for $E_\perp^*$ are assumed based on observations. The ion cooling rate due to ion-neutral collisions through resonance charge exchange and polarization interactions is [*Roble*, private communication, 1991]

$$\begin{aligned} L_{in} \; L_{in} = \Big\{ & \Big[6.6 \times 10^{-14} n(\mathrm{N_2}) + 5.8 \times 10^{-14} n(\mathrm{O_2}) + 0.21 \times 10^{-14} n(\mathrm{O})(2T_n)^{\frac{1}{2}}\Big] n(\mathrm{O^+}) \\ & + \Big[5.45 \times 10^{-14} n(\mathrm{O_2}) + 5.9 \times 10^{-14} n(\mathrm{N_2}) + 4.5 \times 10^{-14} n(\mathrm{O})\Big] n(\mathrm{NO^+}) \\ & + \Big[5.8 \times 10^{-14} n(\mathrm{N_2}) + 4.4 \times 10^{-14} n(\mathrm{O}) + 0.14 \times 10^{-14} n(\mathrm{O_2}) T_n^{\frac{1}{2}}\Big] n(\mathrm{O_2^+}) \Big\} \end{aligned} \tag{2.47}$$

The electron and ion energy equations are two coupled nonlinear equations that are solved iteratively.

CHAPTER 3

Method of Solution

A flow chart of the self-consistent one dimensional time varying auroral model consisting of various interacting physical processes is shown in Figure (2.1). There are three groups of coupled equations corresponding to the main physical processes in the thermosphere, which are electron transport, ion diffusion and chemical reaction, and electron and ion energy balance. Simultaneous solution of all the equations is not attempted. Instead, physical arguments are used to simplify the computational problem according to different time scales and altitude regimes. The initial conditions and boundary conditions for each equation are discussed in the following sections.

3.1 Solution Procedure

Processes in the thermosphere operate on three time scales:

1) Instantaneous processes. As mentioned previously, electron transport, heating, and ionizing processes associated with electron and/or photon impact are faster than the response of the medium. Energetic electrons take only several seconds to penetrate the thermosphere and lose energy during auroral events which last for tens of minutes. The deposited energy is quickly shared with ambient electrons and ions by collisions and conduction. Therefore, the electron and ion temperatures quickly approach steady state values. Steady state is assumed for both the electron transport equation and the energy equations. However, the boundary conditions for these equations are time-dependent.

2) Fast processes. Ion diffusion and photochemical processes for each species depend upon temperature and altitude. At high altitudes, the major ions, O^+ and H^+, take hours to reach

equilibrium, but an auroral event generally lasts only for a few minutes. For the time scale of interest, the electron density and ion composition vary with time. At low altitude, in the *E*-region, diffusion is unimportant compared with chemical reactions. The ion densities are simply controlled by chemical lifetimes which are of the order of minutes [*Jones and Rees*, 1973]. For the entire region, the time scales of ion diffusion and chemical reactions vary from one minute to hours, requiring explicit time dependence in the solution of the ion continuity equations.

3) Slow processes. One of the main sources of ionization and dissociation in the auroral model is solar EUV radiation which varies with the solar zenith angle and is, therefore, a function of local time. The neutral density and composition of the atmosphere also depend upon local time. The variability in these parameters is quite small throughout the day, except at sunrise and sunset. Therefore, processes associated with solar sources can be treated as slow processes. Thus, during changes resulting from fast processes all parameters associated with slow processes are assumed unchanged.

In this auroral model, a variable time step is used to fit the needs of instantaneous, fast and slow processes. Within the auroral events a small time step is adopted and outside the aurora larger time steps are used. For each time step, the neutral densities and temperature of the MSIS-90 model are used, shown in Figure (2.1) below the dashed line. Based on the neutral densities and solar EUV flux, the photoionization rate and primary photoelectron production rate are calculated using equations (2.16) and (2.32) with the adopted cross sections given in *Rees* [1989]. The boundary conditions are given by the conjugate photoelectron and/or auroral electron flux and the electron transport equation is solved self-consistently, including the polarization field and the primary photoelectrons as an internal source. The electron intensities obtained by solving the electron transport equation are used to compute the electron impact ionization rates for each species. The total ionization rate is obtained by adding the ionization rates due to solar EUV, the geocoronal flux and the solar X-ray flux. Ion densities are computed by solving the time

dependent ion continuity equations. With the ion composition, electron density profiles and precipitating electron intensities, the electron and ion energy equations are solved and the electron and ion temperatures are calculated. Ion and electron densities and temperatures provide the input for calculating the electrical conductivity and the polarization electric field in the ionosphere. Once the polarization electric field is derived, the electron transport equation can be solved for the next time step.

Observations of auroral enhancements of NO concentrations in the lower thermosphere [*Zipf et al.*, 1970] have focused attention on the chemistry of the odd nitrogen species in the aurorally perturbed atmosphere. Atomic nitrogen may diffuse in the upper E-region and this would influence the ion chemistry. The problem has been examined theoretically by several investigators (e.g. *Jones and Rees*, 1973; *Hyman et al.*, 1976; *Gerard and Barth*, 1977; *Roble and Rees*, 1977; *Rees*, 1989). In the present model all neutral constituents are assumed to be given and invariant.

3.2 Implementing the Solution of Each Equation

3.2.1 Electron Transport Equation

With the approximations described and justified in section (2.2), the electron transport equation becomes a linear integro-differential equation, i.e. equation (2.15). The solution of the angular dependent electron transport equation requires solving an integro-differential equation and evaluating the source functions. To solve the electron transport equation, *Stamnes* [1978] and *Lummerzheim* [1987] developed an approach based on the discrete ordinate method (DOM) of radiative transfer [*Chandrasekhar*, 1960; *Stamnes et al.*, 1988]. With this approach, the phase functions are expanded into Legendre polynomials and the angular integrals in the transport equation are represented by quadrature sums. The integro-differential equation is thereby transformed

into a system of coupled differential equations which in turn lead to a system of linear algebraic equations. The solution of the resulting system of algebraic equations is described in detail by *Stamnes et al.* [1988] whose numerical code is adopted here. The present work develops a new electron transport code by adopting and modifying the DOM approach of electron transport [*Lummerzheim*, 1987], and including the electric field and magnetic field terms.

Energy degradation is handled by solving the problem from high to low energies. The component of Q_{coll} due to energy degraded electrons at a given energy can be computed from the intensity distribution at higher energies. The locally produced photoelectrons and the secondary electrons from ionizing collisions are combined in the term Q_{coll}. Q_E and Q_B (equation (2.15)) depend not only on $\frac{\partial}{\partial \epsilon}$ but also on $\frac{\partial}{\partial \mu}$. The DOM method of *Stamnes et al.* [1988] provides analytic expressions for the intensity which can be evaluated at any desired angle. The derivative with respect to angle is

$$\frac{\partial I(\tau,\epsilon,\mu)}{\partial \mu} \approx \frac{I(\tau,\epsilon,\mu+\delta\mu) - I(\tau,\epsilon,\mu)}{\delta\mu}$$

and a finite difference scheme is used to calculate the energy derivative

$$\frac{\partial I(\tau,\epsilon,\mu)}{\partial \epsilon} \approx \frac{I(\tau,\epsilon_{n+1},\mu) - I(\tau,\epsilon_n,\mu)}{\Delta\epsilon_n}$$

The energy steps adopted in the numerical solution of equation (2.15) are sufficiently close together to justify specifying the source terms due to the electric and magnetic fields at a given energy by their value at the next higher energy on the grid. The validity of this assumption has been verified by applying an entirely different method of solution to identical test cases.

Cannon [1984] has suggested that terms proportional to $\frac{\partial}{\partial \mu}$ and $\frac{\partial}{\partial \epsilon}$ can be treated as non-local perturbations. If I is the solution of equation (2.15), let

$$I = I^0 + \lambda I^1 + \lambda^2 I^2 + \ldots \tag{3.1}$$

where the parameter λ (which will later be put equal to unity) has been included simply as an aid in isolating terms of approximately the same magnitude. A recursion relation is obtained

$$\mu \frac{\partial I^l(\tau, \epsilon, \mu)}{\partial \tau} = I^l(\tau, \epsilon, \mu) - \frac{\omega}{2} \int p(\mu' \rightarrow \mu) I^l(\tau, \epsilon, \mu')\, d\mu' + Q^l(\tau, \epsilon, \mu, I) \tag{3.2}$$

$$Q^l = \begin{cases} Q_{coll}, & \text{for } l = 0 \\ Q_{E\&B}|^{l-1}, & \text{for } l > 0 \end{cases}$$

where l denotes the order of the perturbation. It is important to note that if the series in equation (3.1) converges, it will converge to the correct result [*Cannon*, 1984]. Figure (3.1) illustrates the convergence of the non-local perturbation method for the case that includes a polarization field plus an imposed electric field of 10 μV/m and a homogeneous magnetic field.

The perturbation method yields values similar to the direct method adopted in this thesis but more than five iterations are required to achieve the same results. Figure (3.2) displays the comparison between two approaches.

The attention is restricted to examining weak upward electric fields with a strength below 50 μV/m. In this range the energy gained by an electron in a mean free path at heights less than 1000 km does not exceed the mean energy of thermal electrons. This obviates the need to include wave processes associated with the excitation of low-frequency plasma instabilities.

Electron impact cross sections are essential input parameters for the transport equation. Electron transport depends on energy degradation which requires detailed knowledge of the cross sections and associated energy losses of each individual excited state of the atom or molecule. An extensive compilation of cross sections, including 29 excited states of N_2, O_2 and atomic oxygen, 11 excited ion states, and elastic interaction is found in *Lummerzheim* [1987].

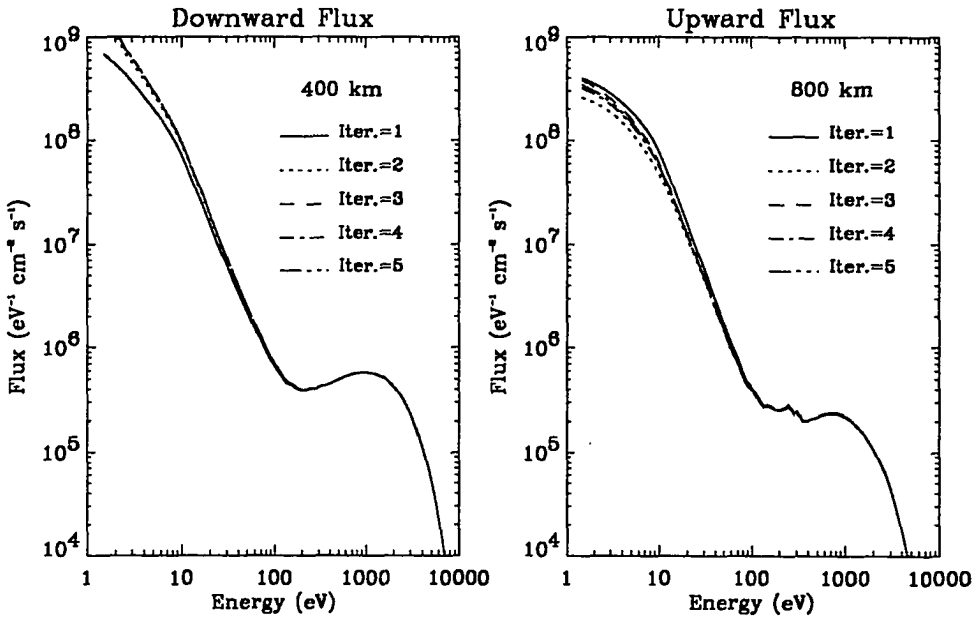

Figure 3.1 The downward and upward hemispheric fluxes are shown at 400 and 800 km, respectively, computed by the iteration method of non-local perturbation.

The downward electron intensity is specified at the upper boundary, while the upward electron intensity is given at the lower boundary. The lower boundary is assumed to lie at a density within the atmosphere that is large so that the intensity becomes vanishingly small. The upper boundary condition applied to the transport equation depends on the problem that is being addressed. In the photoelectron transport case a small downward electron flux characterized by a Maxwellian energy distribution with a characteristic energy of about 50 eV and an energy flux of 0.01 erg $cm^{-2}sec^{-1}$ is assumed, to account for the contribution from the conjugate hemisphere. In the auroral case the flux also vanishes at the lower boundary while at the upper boundary the intensity of auroral electron precipitation is adopted from rocket or satellite measurements or an analytic form is specified.

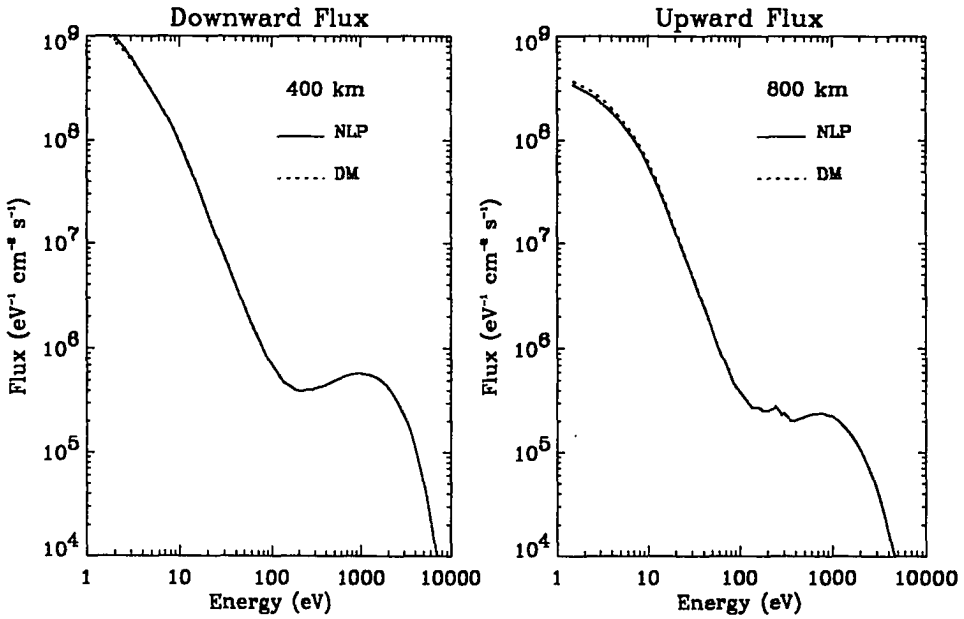

Figure 3.2 Electron energy spectra of downward and upward hemispheric fluxes at 400 and 800 km, respectively, for two different computational schemes: direct method (DM) and non-local perturbation (NLP) after 5 iterations.

3.2.2 Ion Continuity Equations

All nine ion species listed in Table (2.1) are included in this time-varying auroral model. As mentioned previously, the chemical lifetime controls the ion densities at low altitude while diffusion dominates at high altitude. In the E-region, the chemical lifetime of all species is about one minute which is less than the smallest time step (two minutes) during assumed auroral events, allowing ion densities to be calculated by assuming a steady state and local photochemical equilibrium without diffusion. Firstly, O^+, H^+ and N^+ are computed based on the balance between local sources and sinks. With respect to the densities of O^+, H^+ and N^+, the quartic equation (e.g. equation (2.30)) can be solved exactly yielding one real and physical root for the electron density. Secondly, the densities of N_2^+, O_2^+ and NO^+ are calculated from equation (2.31). In the

F-region and above, the coupled time-dependent diffusion equations for two major ions, O^+ and H^+, are derived in Chapter 2. Equation (2.26) and (2.27) are a parabolic system of equations in one spatial dimension and time. A second order finite difference scheme is used for the spatial variable and the method of lines for the time variable. Based on the same procedure used for the *E*-region, the N^+, N_2^+, O_2^+ and NO^+ are computed by solving the quartic equation (2.30) and the ion continuity equations (2.29) and (2.31).

For the coupled time-dependent diffusion equations of O^+ and H^+, the initial conditions are computed self-consistently following the same procedure described in Section 3.1. Firstly, the neutral densities and temperature are obtained from MSIS-90. The initial ionospheric conditions are established by the following procedure. The electron transport equation is solved and various ionization rates are computed. Instead of solving the time-dependent ion continuity equations of O^+ and H^+, the steady-state diffusion equations are solved and all the ion densities are calculated. The temperatures of ions and electrons are determined by solving the electron and ion energy equations. The new results are used to update the initial conditions of the ionosphere. After several iterations, the final convergent results are computed self-consistently, equivalent to the ionosphere reaching equilibrium. The computed parameters are not, strictly, 'initial' conditions, however, the primary interest is in the response of the ionosphere under conditions of substantial auroral bombardment. Under these circumstances the results are not sensitive to the initial conditions while the equilibrium state provides a good and self-consistent set of initial parameters. To mitigate this simplistic approach, the results obtained after several hours of elapsed real time are used, such that the ionospheric density and composition is no longer sensitive to the initial conditions.

The upper boundary of the ion continuity equations can be specified either as a concentration or as a flux. The O^+ and H^+ fluxes are specified at the upper boundary either corresponding

to observations of the outflow or by an arbitrary time-dependent assumption. Photochemical equilibrium prevails at the lower boundary.

3.2.3 Electron and Ion Energy Equations

As discussed in Chapter 2, the ionosphere can be divided into two regions: the region of local sources and sinks and the thermal conduction region. Basically, the altitude range over which local energy balance applies depends upon the ionospheric and atmospheric conditions. In the present model, a balance between local heating and cooling rates is assumed below about 150 km. The electron temperature is determined by solving the local energy equilibrium equation. The root of this nonlinear equation is found by using the *Newton-Raphson* method [*Press et al.*, 1989]. Above 150 km, the electron energy equation is a second order differential equation (2.36) derived in Chapter 2. This equation is solved by the *Relaxation Method* which determines the solution by starting with a guess and improving it iteratively [*Press et al.*, 1989]. The iteration scheme adopted is a multi-dimensional *Newtons*'s method. As the iterations improve the solution, the result is said to relax to the true solution. The steady-state diffusion equations of O^+ and H^+ are also solved by this method.

The differential equation (2.36) requires boundary conditions appropriate to the physical problem being investigated. Local equilibrium between T_e, T_i and T_n prevails at the lower boundary. A heat flux is appropriate at the upper boundary but observations provide little guidance. More commonly, the heat flux is adjusted to match a measured temperature. Large heat fluxes produce temperature gradients that influence the magnitude of the polarization field. Large values of heat flux are associated with the decay of the ring current during large geomagnetic storms. The resulting high electron temperature, in excess of 6000 K, accounts for the mid-latitude red arc phenomenon associated with such events [*Rees and Roble*, 1975]. A downward

heat flux of 1×10^9 eV cm^{-2} sec^{-1} has been assumed, which yields values of T_e typically measured during auroral activity.

CHAPTER 4

Numerical Results

To evaluate the time varying auroral model numerical calculations have been carried out of the coupled electron transport, ion continuity, and energy equations for auroral events representing external flux sources and for solar cases representing embedded sources of photoelectrons. An $F_{10.7}$ solar activity index of 150 is assumed and geomagnetically quiet conditions prevailed, with an A_P index of 30. The MSIS-90 neutral atmosphere [*Hedin*, 1991] is adopted at 60°N, 200°E for northern winter (date 90030). The densities of minor neutral species of $N(^4S)$ and $N(^2D)$ are obtained from MSIS-90 by assuming a ratio of 100:1 between the two species. The NO profile measured by *Meira* [1971] is adopted. I first present the diurnal variation of the ionospheric properties during non-auroral conditions at a given geographic location, as a reference to auroral cases. At a specified time during the non-auroral calculation an auroral event is introduced and the ionospheric response to the auroral input is calculated. The present model covers the region between 80 and 800 km. The results of the ionospheric response are discussed in following sections.

4.1 The Diurnal Variation of the Ionosphere During Non-auroral Conditions

4.1.1 Solar EUV and Photoelectron Ionization

Without auroral precipitation, the main source of ionization is the solar EUV flux, *Hinteregger*'s [1981] measurements are adopted and linearly interpolated as a function of the $F_{10.7}$ solar flux. The photoionization and photoabsorption cross sections and branching ratios used in the

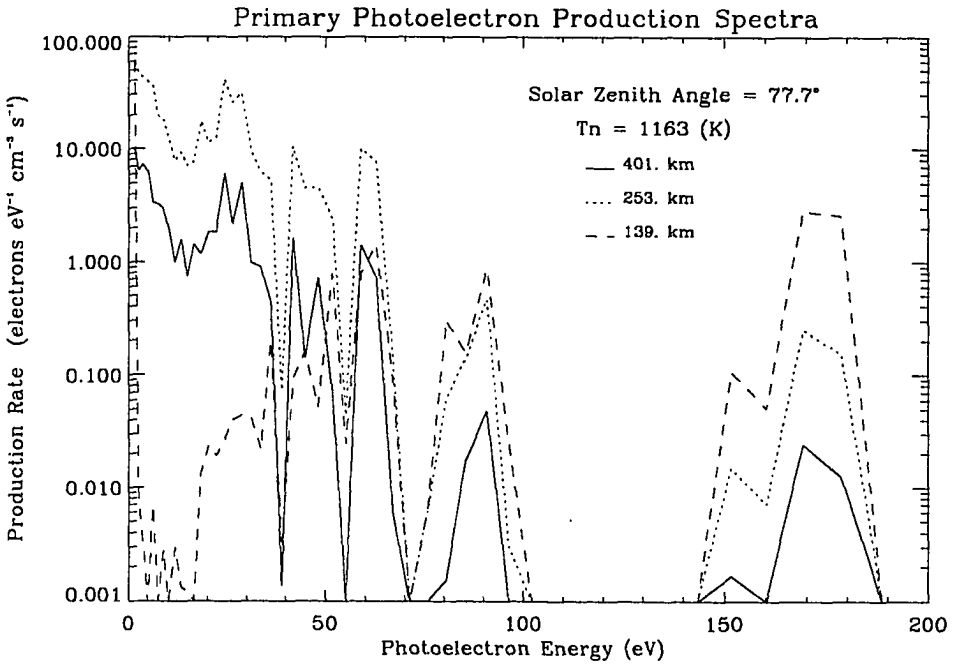

Figure 4.1 The primary photoelectron production spectra at a solar zenith angle of 77.7° at three altitudes. The exospheric temperature is 1163 K.

model are taken from *Rees* [1989]. In calculating the photoionization rates, three main neutral species, N_2, O_2 and O, with 14 different states of their ions, are included. Primary photoelectron production spectra are calculated at each altitude and time step within the model. Figure (4.1) gives an example of the calculated primary photoelectron production spectra at noon at 401, 253, 139 km, for a solar zenith angle of 77.7°. Most primary photoelectrons have energies below 200 eV. The structure shown in Figure (4.1) results from the energy dependent solar radiation spectrum and the photoionization cross sections. The photoelectron spectra are computed by solving the electron transport equation. A small conjugate photoelectron flux is included by specifying a Maxwellian spectrum with an energy flux of 0.01 erg cm^{-2} s^{-1} and a characteristic energy of 50 eV, and adding a power law with an ϵ^{-2} below 10 eV at 800 km, the upper boundary. Figure (4.2) shows the downward and upward components of the photoelectron flux at three altitudes

calculated for the embedded photoelectron source shown in Figure (4.1). At 200 km the downward and upward components of the flux are virtually identical up to energies of several tens of eV. The structure at 2 to 3 eV is attributed to the large cross section for excitation of vibrational levels in N_2, but the effect becomes pronounced only at levels where molecular species become abundant. At 300 km and above the upward fluxes exceed the downward components because of the embedded primary photoelectrons. It is noted that the upward flux at 800 km in the 10 to 40 eV energy region exceeds the downward flux by an order of magnitude to become a source of conjugate photoelectrons. After the photoelectron spectrum has been calculated, electron impact ionization can readily be determined by integrating the appropriate ionization cross section with the electron intensity.

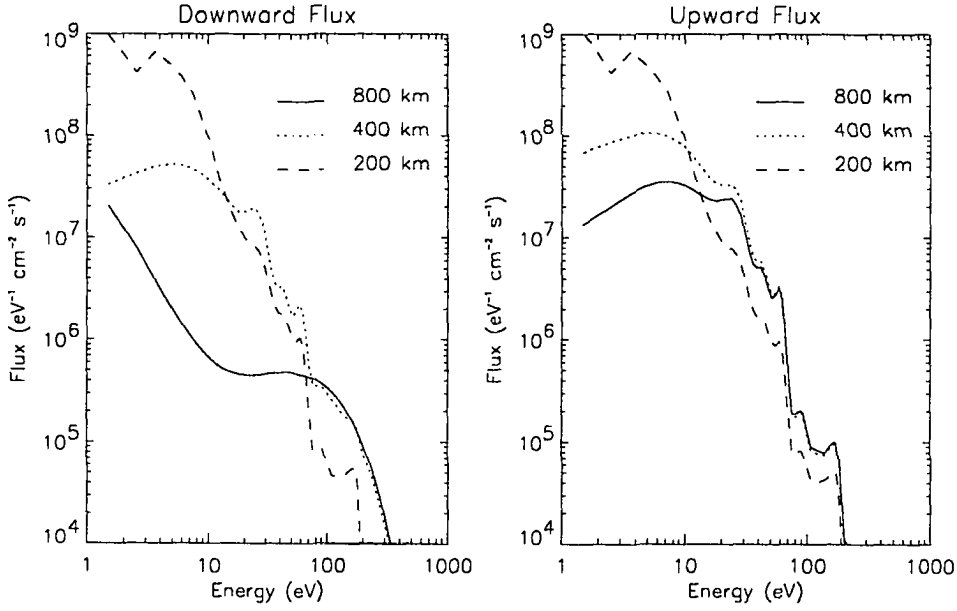

Figure 4.2 Differential photoelectron energy spectra of the downward and upward hemispheric fluxes at three altitudes.

The night-time electron density and temperature in the *E*- and *F*-regions of the ionosphere are found to be larger in the auroral oval than at mid and low latitudes at corresponding local times [*Johnson*, 1969]. These observations are interpreted in terms of a small flux of electrons that continually precipitates into the auroral ionosphere. Therefore, without aurora a small energy (0.01 erg cm^{-2} s^{-1}) soft electron flux is assumed with the characteristic energy of 50 eV as the upper boundary condition for the electron transport equation. The characteristic energy is half of the mean energy for a Maxwellian distribution. Variations of the solar zenith angle, incident electron energy flux and the characteristic energy with time for this diurnal variation case are shown in Figure (4.3).

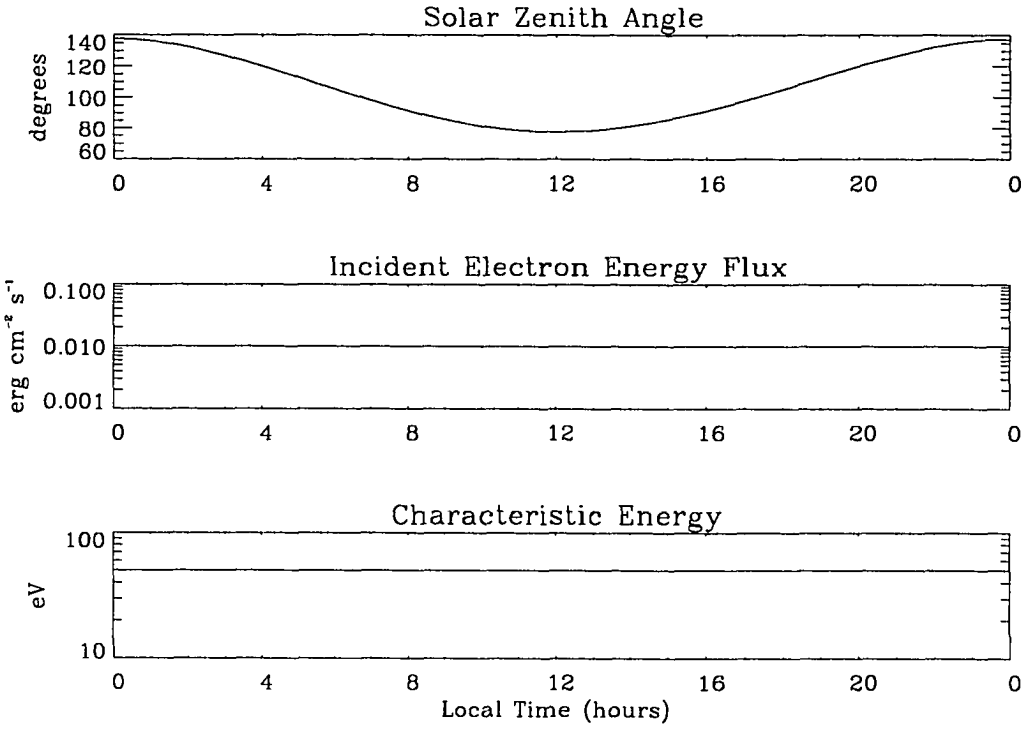

Figure 4.3 The diurnal variation of solar zenith angle, incident electron energy flux and characteristic energy at 800 km.

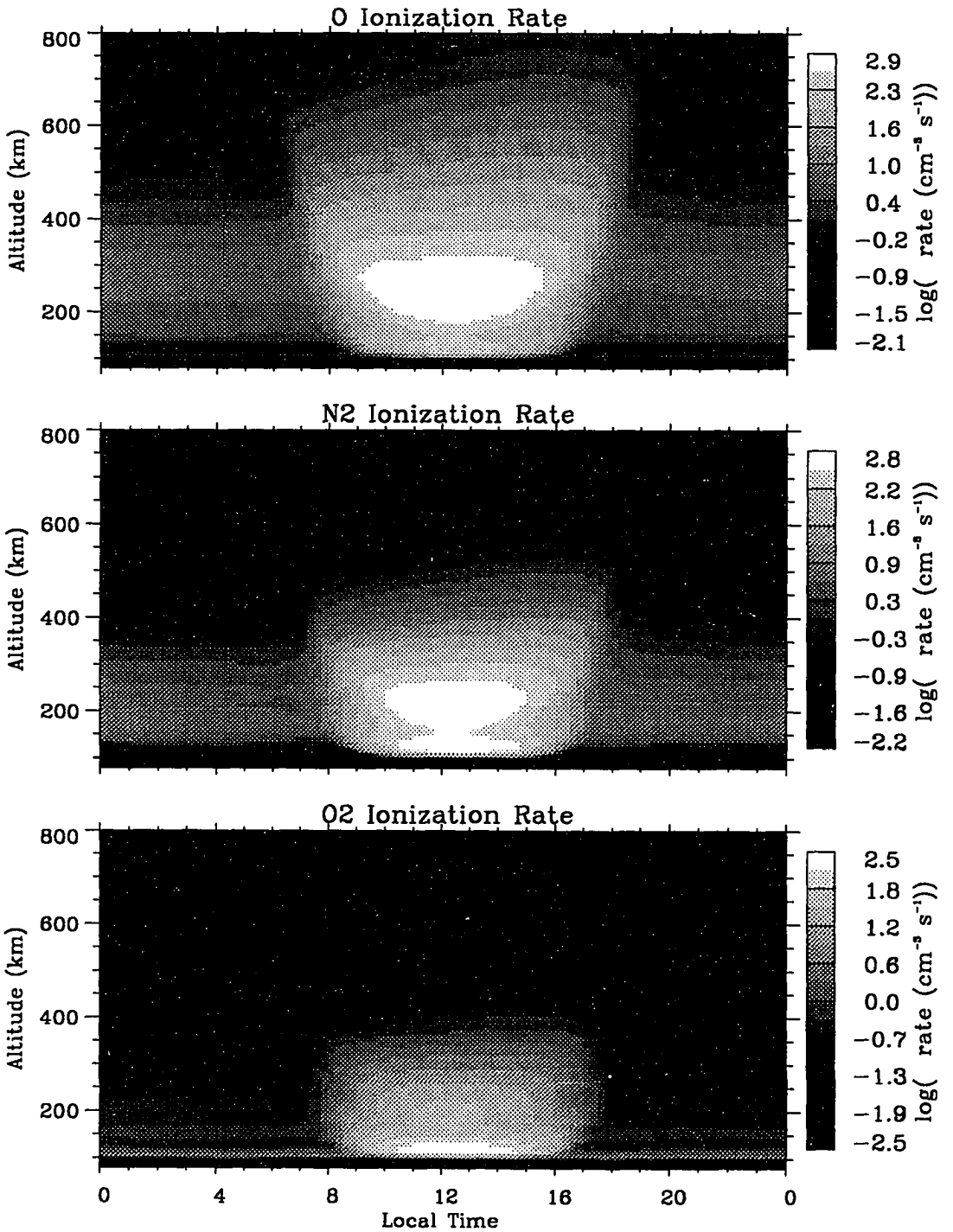

Figure 4.4 The diurnal variations of the ionization rates of three main neutral species, O, N_2, and O_2.

The diurnal variation of the ionization rates of three main neutral species are shown in Figure (4.4). During the night, ionization is produced in the *E*- and lower *F*-regions by scattered EUV and by precipitating soft electrons. During daytime, the photoionization and the electron impact ionization associated with photoelectrons are the dominant ionization sources at high altitudes. Solar X-rays penetrate deeper into the atmosphere to produce the dominant ionization in the *E*-region. The geocoronal ionization contributes little to daytime ionization at any altitude. After sunrise the ionization increases rapidly from its night-time minimum. The ionization below about 300 km is under strong solar control, peaking at noon when the solar zenith angle is smallest and decreasing symmetrically to dawn and dusk. Ionization above about 300 km, however, is influenced by the neutral composition and temperature. Therefore, its contour shapes do not show the strong solar zenith angle dependence, and maximum ionization occurs in the early afternoon.

4.1.2 Ionospheric Structure

The height distribution of ion densities is determined by solving the coupled ion continuity equations for $O^+(^2P)$, $O^+(^2D)$, $O^+(^4S)$, O_2^+, N_2^+, NO^+, $O_2^+(a^4\Pi)$, H^+ and N^+. The solution has been discussed in detail in Chapter 3. Zero fluxes are assumed at the upper boundary for the coupled time-dependent diffusion equations of O^+ and H^+. Photochemical equilibrium prevails at the lower boundary. The coupled electron and ion energy equations are solved at each time step according to the method discussed previously. A downward heat flux of 1×10^9 eV cm^{-2} s^{-1} at the upper boundary is assumed in solving the electron energy equation. Local thermal equilibrium between T_e, T_i and T_n prevails at the lower boundary.

The ion and electron density profiles at noon are shown in Figure (4.5). The electron density peak occurs at 290 km with a value of about 6×10^5 cm^{-3}. In the *F*-region and above the major ion is $O^+(^4S)$. At very high altitudes, H^+ becomes increasingly important due to the charge exchange

process of H with O^+. However, there is some uncertainty in the profiles because magnetosphere-ionosphere coupling has been neglected by assuming zero flux at the upper boundary. Below 200 km, the $O^+(^4S)$ number density decreases and NO^+ and O_2^+ become the dominant ions. The N_2^+ density is small primarily because of the fast chemical reactions removing N_2^+.

The electron and ion temperature profiles, shown in Figure (4.5), are determined by solving the coupled electron and ion energy equations. At the high altitudes, the electron temperature is maintained mostly by a flow of heat from the magnetosphere, determined by the specified upper boundary condition. Without this heat flux, the electron temperature in the top side ionosphere would be considerably lower. Below 300 km, the electron temperature is maintained by photoelectron heating producing a steep temperature gradient near 200 km. The ion gas is primarily heated by Coulomb collisions with the electrons and cooled by elastic and resonant charge exchange interactions with the neutral species, as discussed previously. Above about 350 km, coupling with electrons predominates and the ion temperature approaches the electron temperature. Below 350 km ion-neutral collisions predominate and the ion temperature approaches the neutral gas temperature. A small increase over the neutral temperature is due to heating by a perpendicular electric field. The perpendicular electric field primarily heats the ion gas in the lower thermosphere, where the Pederson conductivity is high.

The electron and ion densities at 22:00 LT, shown in Figure (4.6), have decreased considerably from their daytime values. The *F*-region is maintained by the night-time ionization source of the scattered EUV radiations from the geocorona and by impact ionization of soft electron precipitation. The main heat sources for the electron gas at night are the degraded electron population from the ionization sources listed above and heat flux flowing in from the magnetosphere, which is capable of maintaining T_e greater than T_i and T_n at altitudes above 200 km. In spite of the low electron density at night, the electron temperature is still below daytime values because of absence of the major photoelectron heating source. The ions are heated by the hot ambient

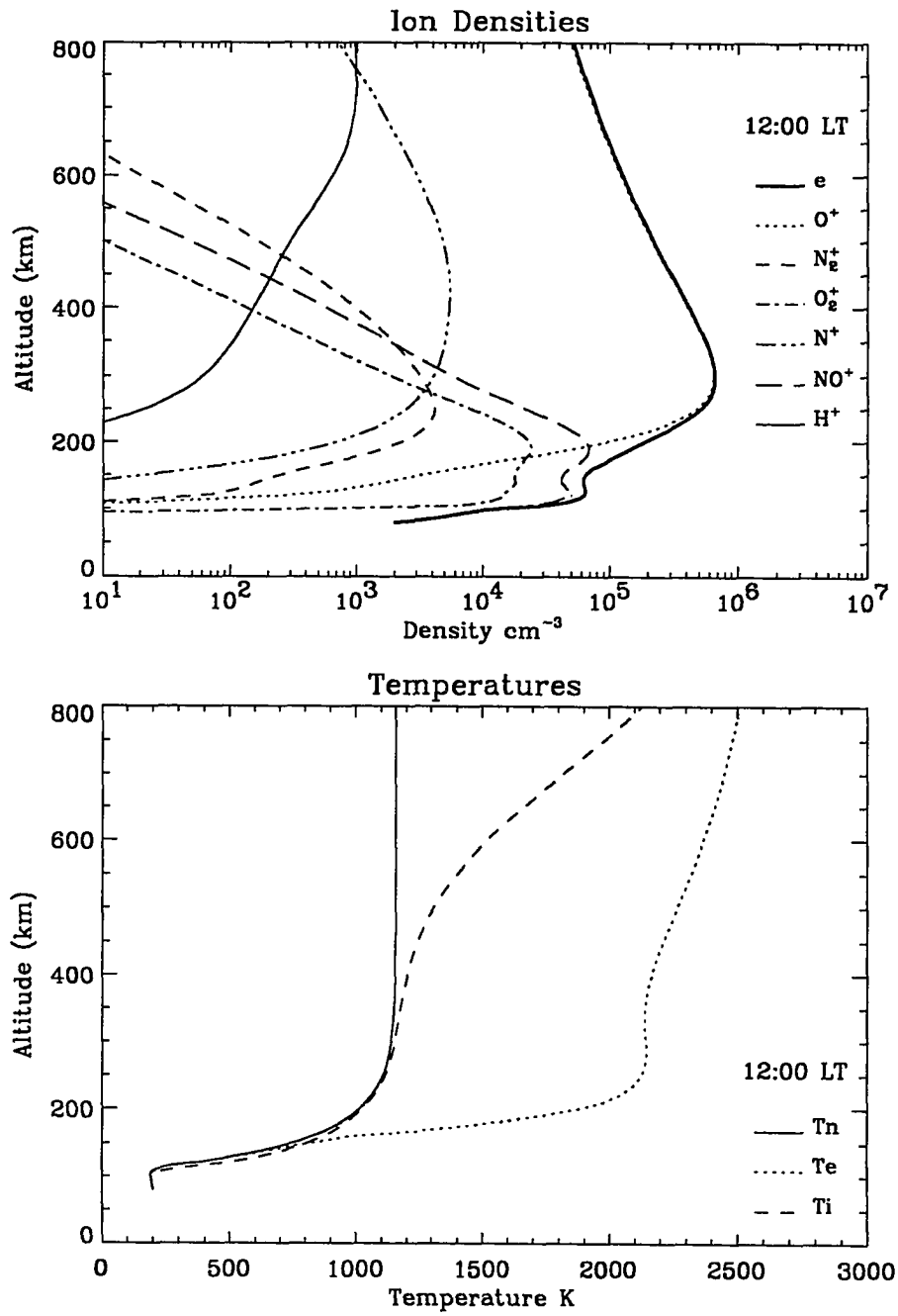

Figure 4.5 The ion composition and electron density profiles (top) and the electron, ion and neutral temperature profiles (bottom) at noon.

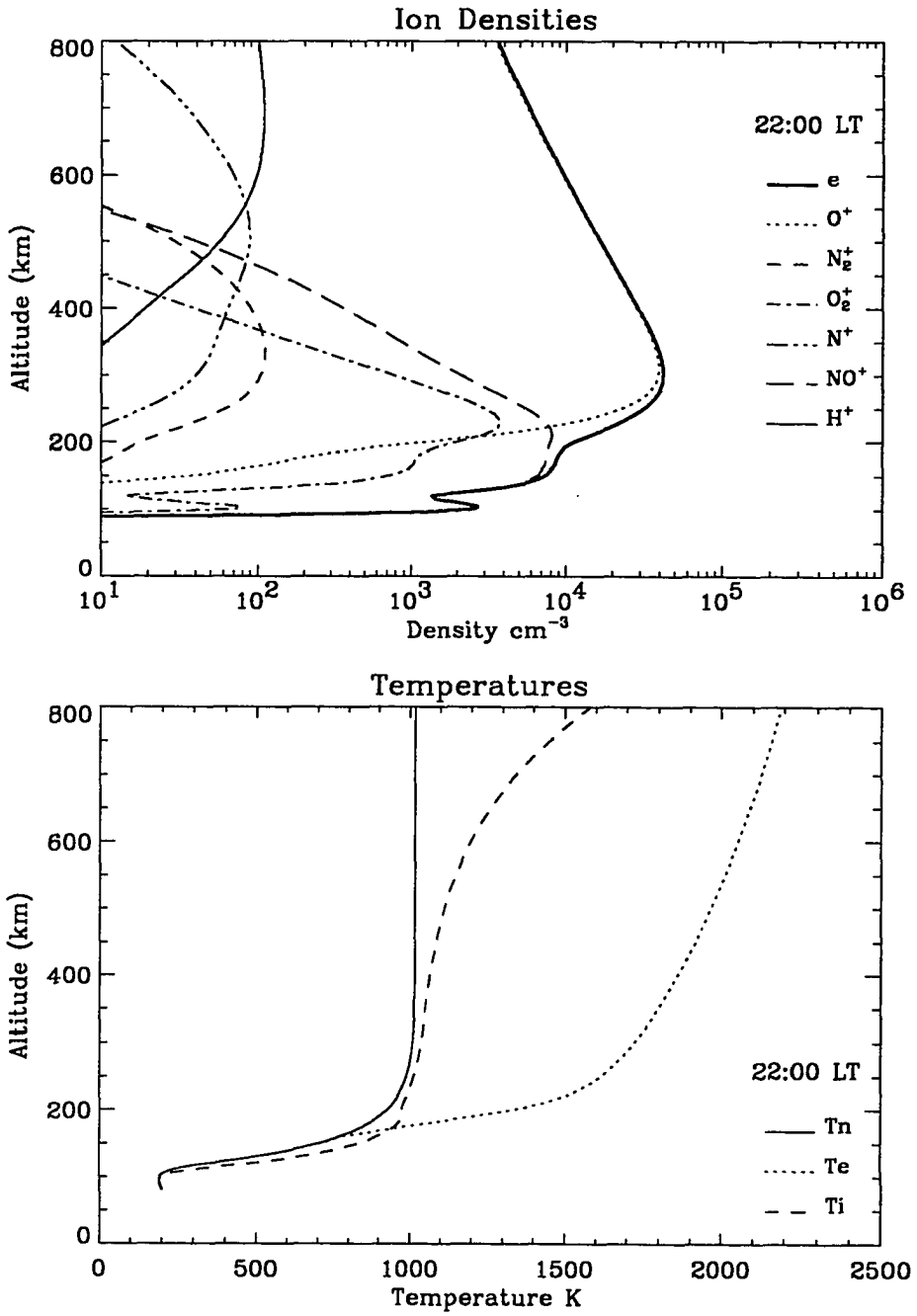

Figure 4.6 The ion composition and electron density profiles (top) and the electron, ion and neutral temperature profiles (bottom) at 22:00 LT.

electrons and the ion temperature increase in the topside ionosphere where the ion-neutral collision frequency is low. The Joule heating due to the perpendicular electric field enhances the ion temperature at low altitudes where the Pederson conductivity has a maximum value.

The diurnal variations of the electron density, electron temperature, ion temperature and neutral temperature are shown in Figure (4.7). Above 250 km, the time constant for the electron density build-up is longer than the time constant for the ionization rate build-up as well as the decay rate. Below 250 km, the variation of the electron density closely follows the variation of the ionization rate. From sunrise to sunset, the *F*-region peak height varies from 275 to 335 km. Night-time ionization by soft electron precipitation maintains the night-time ionosphere and keeps the peak height at 300 km. The maximum electron density at the peak is 6.5×10^5 cm^{-3} and occurs at 14:00 LT at an altitude of 303 km. The electrons are heated by collisions with energetic electrons and by a flow of heat from the magnetosphere. The electron temperature is also controlled by the electron number density through elastic and inelastic collisions between the electrons, the ions, and the relatively cool neutrals. When the electron density is high, the cooling rate is greater than when the electron density is low. Therefore, for a given heating rate the temperatures are inversely related to the electron density. At sunrise, there is rapid increase in the temperature at all altitudes above 200 km owing to increased heating arising from photoelectron production due to the solar EUV photoionization. Because the electron density at this time is low the average energy input per ambient electron is larger. The electron temperature increases abruptly at sunrise, then decreases as the electron density increases. At sunset the electron temperature reaches a minimum, then increases as the electron density decays. The diurnal variation of the ion temperature shows similar behaviour to the electron temperature variation at high altitudes because the ions are primarily heated by Coulomb collisions with the hot electrons. Below 400 km the ion temperature basically follows the neutral temperature variation.

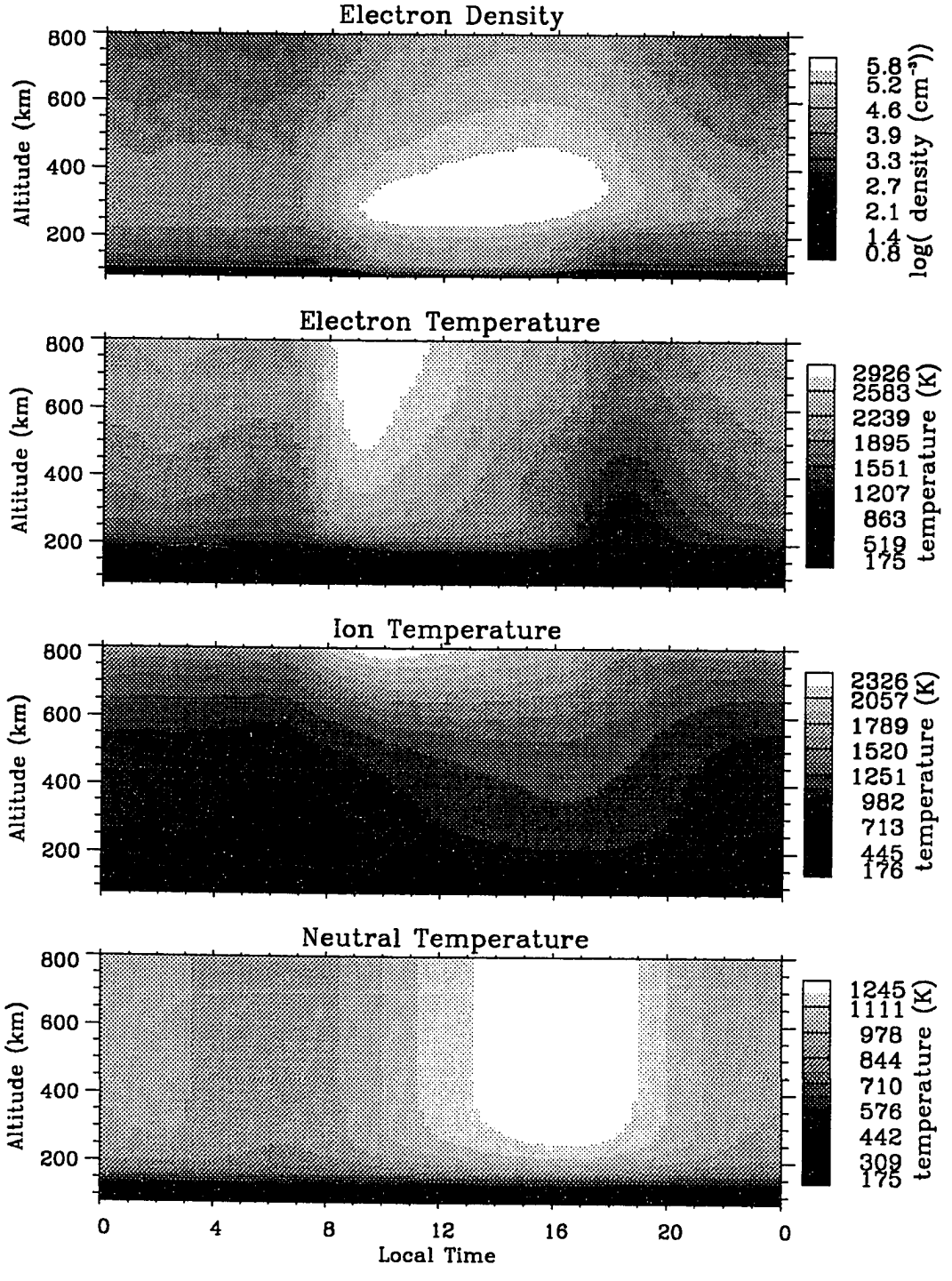

Figure 4.7 The diurnal variation of the electron density, electron temperature, ion temperature and neutral temperature.

4.2 A Night-time Auroral Event

4.2.1 Typical Auroral Precipitation

With rare exceptions, auroral precipitation events do not last longer than ten minutes without undergoing changes in brightness or significant motion, and usually they do not persist even that long. The model run is started at midnight but the auroral precipitation is not turned on until 22:00 LT of the following night and lasts ten minutes. Auroral electron precipitation is assumed to have an isotropic angular distribution and a Maxwellian energy distribution with 1 keV characteristic energy and a 5 erg cm^{-2} sec^{-1} energy flux, supplemented by a power law spectrum with energy dependence ϵ^{-2} below 100 eV, which may occur over a wide region of the auroral oval at any time. The auroral electron flux is imposed at the upper boundary of 800 km. As in the preceding section, at the lower boundary of 80 km zero backscattered flux is assumed in the transport equation, photochemical equilibrium in the continuity equations, and equal electron, ion and neutral temperatures in the energy equations. The upper boundary conditions are the same as in the non-auroral case except for the auroral electron flux specified above.

The differential electron flux computed with this model during the auroral event at 22:02 LT is shown in Figure (4.8) at 800, 400 and 200 km. The downward flux at 800 km is the imposed boundary value but the upward flux is the result of elastic and inelastic collisions, as well as the polarization electric field and dipole magnetic field. Collisional and field effects contribute to the evolution of the flux distribution with increasing atmospheric depth. Effects associated with fields are discussed in detail in Chapter 5. To illustrate the behaviour of the energetic electrons at different energies, Figure (4.9) shows altitude profiles of the upward and downward fluxes. At an energy of 1 keV the downward flux penetrates into the atmosphere without a significant altitude variation above 200 km. The upward flux is due to elastic scattering and the magnetic mirror

force. At a lower energy of 10 eV internal sources from degradation of primaries and secondary electron production become important, causing the downward flux to increase where the density of the scatterer becomes large. Below 200 km the upward and downward fluxes are equal because of the isotropic secondary electron production.

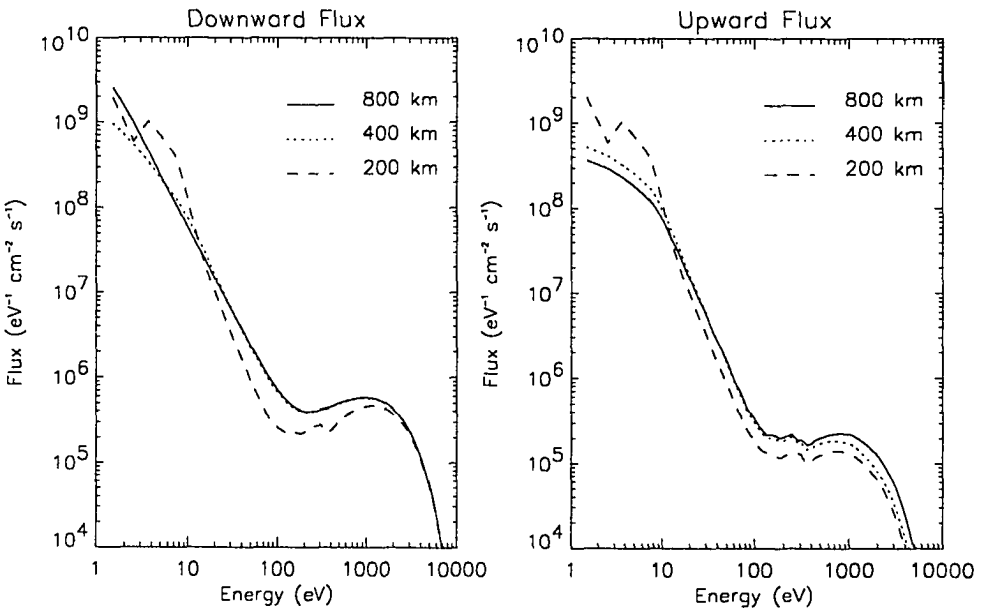

Figure 4.8 The downward and upward fluxes at 3 different altitudes for an isotropic Maxwellian input spectrum with $\epsilon_{char} = 1$ keV. The 800 km downward flux constitutes the boundary condition. Below 100 eV a power law with an ϵ^{-2} energy dependence was added to the Maxwellian distribution.

Integrating the product of the ionization cross sections and the electron intensity over energy and adding the geocoronal ionization rate, the total ionization rates for various species are obtained and are shown in Figure (4.10). The maximum ionization rate of O^+ is 3×10^3 cm^{-3} sec^{-1} and occurs at an altitude of 116 km.

Before presenting the time history of the ionospheric properties throughout the event, altitude profiles of electron and ion densities and temperatures inside the aurora at 22:04 LT are

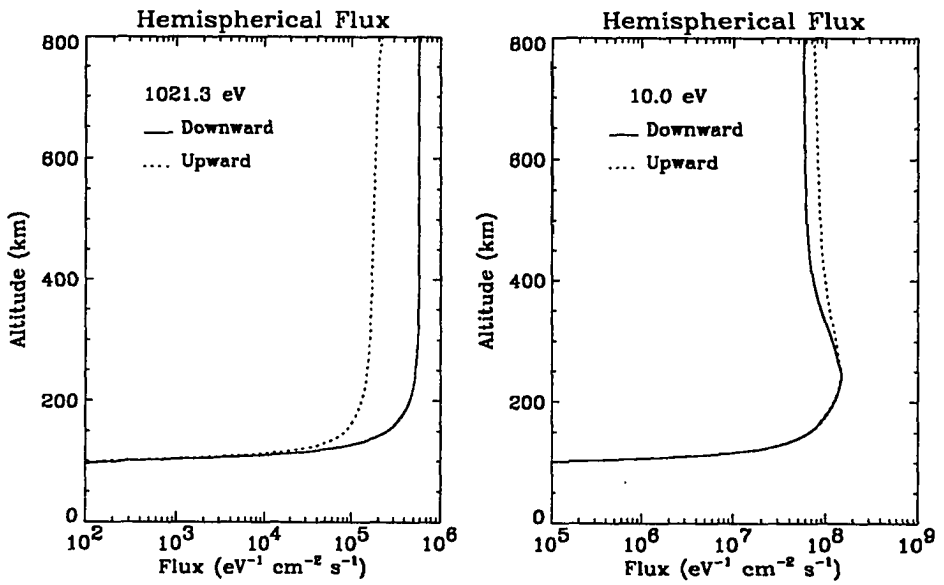

Figure 4.9 Downward and upward fluxes as a function of altitude for 2 selected energies, 1 keV and 10 eV.

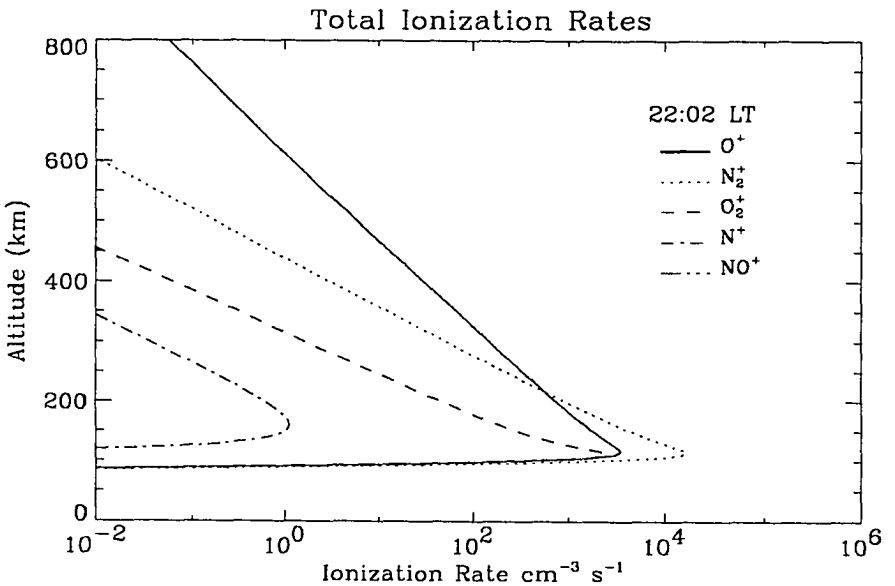

Figure 4.10 Altitude profiles of total ionization rates of O^+, N_2^+, O_2^+, N^+ and NO^+ at 22:02 LT of the auroral event discussed in the text.

shown in Figure (4.11). The ion composition is very different compared with pre-auroral profiles shown in Figure (4.6). Precipitating electrons produce ionization at all altitudes especially in the *E*-region, as shown in Figure (4.10), resulting in a build-up of molecular ions. At high altitudes, the O^+ density is enhanced due to local ionization and diffusion from the high density region at low altitudes. The H^+ density is slightly increased by the charge exchange process due to the enhanced O^+ density. The electron flux also heats the ambient electron gas resulting in an increase of the temperature. The ambient electron gas is heated even at 120 km but it also rapidly cools by collisions with the neutral gas. The electron temperature approaches 4670° K, twice the pre-auroral value in the topside *F*-region. The ion temperature also increases at high altitudes as a result of collisions with the hot electron gas.

The ionization rate of O^+ and the O^+ and H^+ ion densities are shown in Figure (4.12). The ionization rate of O^+ prior to onset of auroral particle precipitation is due to the soft electron precipitation and the geocoronal radiation, as discussed in the preceding section. At the onset of aurora the ionization rate increases rapidly with a maximum value at an altitude of 116 km. After ten minutes the aurora turned off and the ionization rate decreases to the pre-auroral level. Both O^+ and H^+ densities are computed by solving the coupled time-dependent diffusion equations. The O^+ ions show a significant increase over undisturbed night-time density values and subsequently diffuse upward, which leads to an enhancement of H^+ due to charge exchange of O^+ and H. There is a lag of tens of minutes between H^+ and O^+ reaching maximum due to ambipolar diffusion. The time constant for build-up of O^+ and H^+ varies with altitude; below 200 km, the O^+ density quickly reaches a steady state whereas at the *F*-peak and above the density continues to increase throughout the event. Even after the aurora is turned off, the O^+ density still increases above 400 km, as a result of the upward diffusion of ions from the denser lower levels. The decay process is similar to the built-up process, the *F*-peak decays much more slowly and is still a factor of two larger than the pre-auroral density 1 hour after the auroral event. N_2^+, O_2^+, NO^+ and N^+

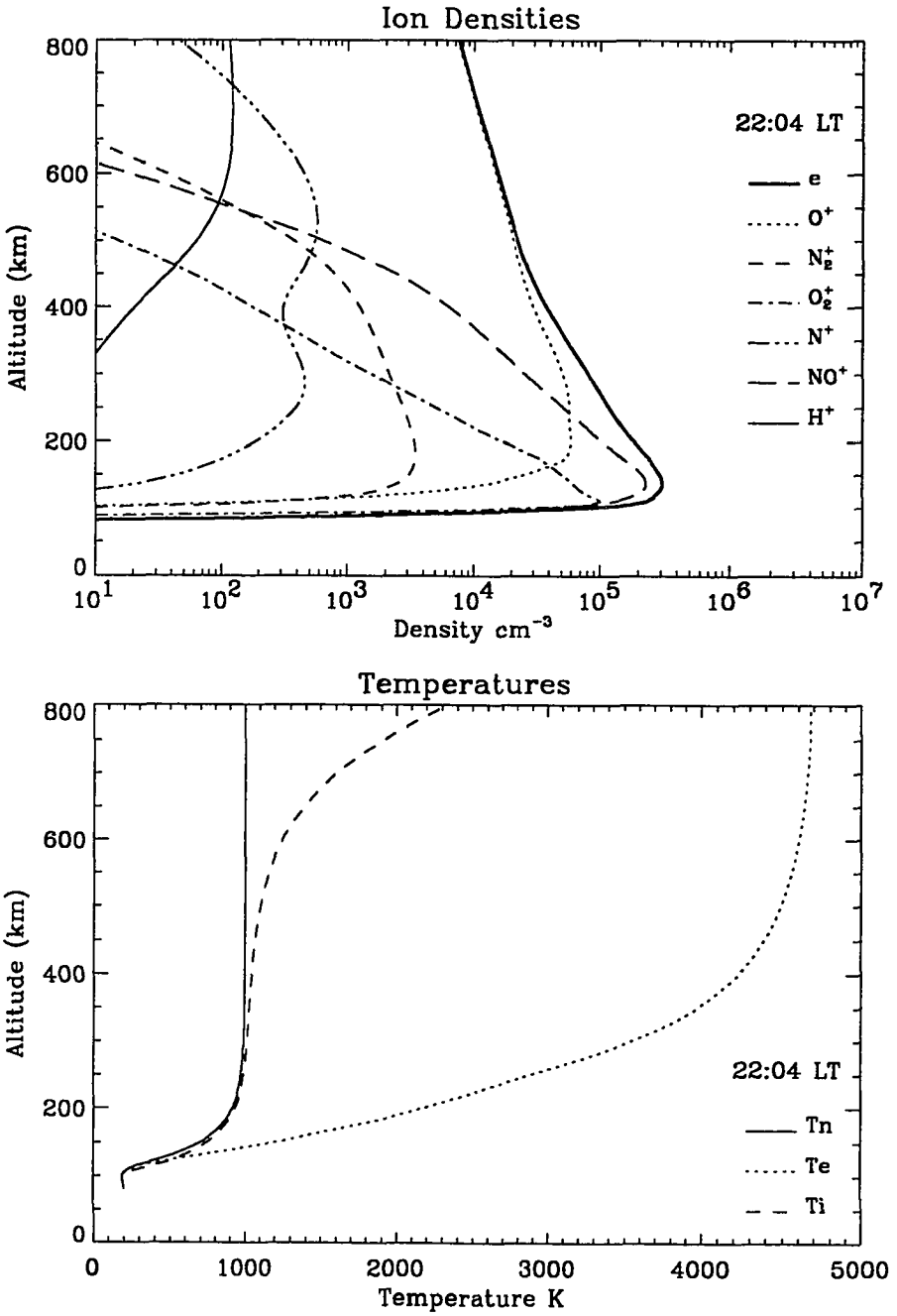

Figure 4.11 The ion composition and electron density profiles (top) and the electron, ion and neutral temperature profiles (bottom) at 22:04 LT.

densities are calculated by assuming local equilibrium with O^+ and H^+ ions. The time history of these ion densities is shown in Figure (4.13). Although the diffusion of molecular ions and atomic nitrogen ions is not explicitly included, the effects of O^+ ion ambipolar diffusion on the O_2^+ and N^+ ions are evident. The most effective chemical sources of O_2^+ and N^+ are various reactions with $O^+(^4S)$ and $O^+(^2D)$ (see Table 2.1), of which the former is subject to ambipolar diffusion. The principal source of N_2^+ ions is impact ionization by energetic electrons, and the N_2^+ ion density closely follows the ionization rate. Various chemical rate coefficients are temperature dependent, resulting in altitude varying source and loss rates of ions.

The electron density is the sum of all ion densities. The electron density and the electron and ion temperatures are computed and shown in Figure (4.14). At high altitudes the electron density follows the major ions O^+ and H^+. At low altitudes, the electron density follows the densities of the molecular ions, responding to the auroral bombardment. One hour after the particle precipitation ceases, the electron density is nearly the same as the pre-auroral value below the *F*-region peak and about a factor of two greater than its pre-auroral value above the peak. The electron temperature increases rapidly in response to heating of the ambient electrons by the auroral electron flux. The electron temperature reaches a peak early in the auroral event, before the electron density begins to build up. As the density increases, the electron temperature decreases because the energy is partitioned among more electrons. The ion temperature is coupled with the electron and neutral temperatures and approaches the electron temperature at high altitudes. The polarization field is enhanced as a result of auroral precipitation. Figure (4.15) clearly shows the relation between electron density and electron temperature at 349 km. There are two peaks in the electron density: the first one is a consequence of the enhanced ionization due to auroral electron precipitation, the second one is the result of electron diffusion upward from denser lower altitudes.

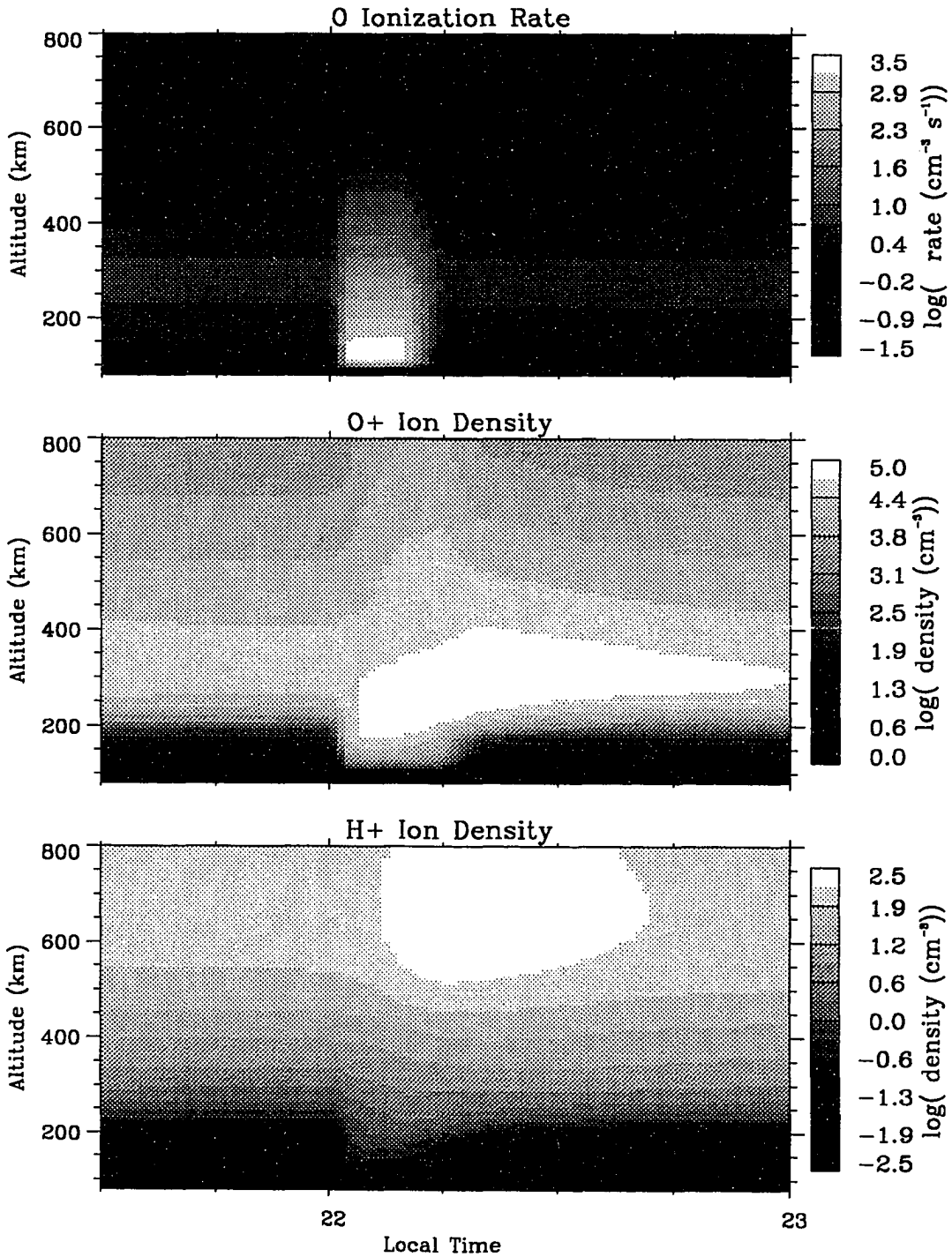

Figure 4.12 Ionospheric response to auroral electron bombardment: the time histories of O^+ ionization rate, O^+ and H^+ densities from 21:30 LT to 23:00 LT.

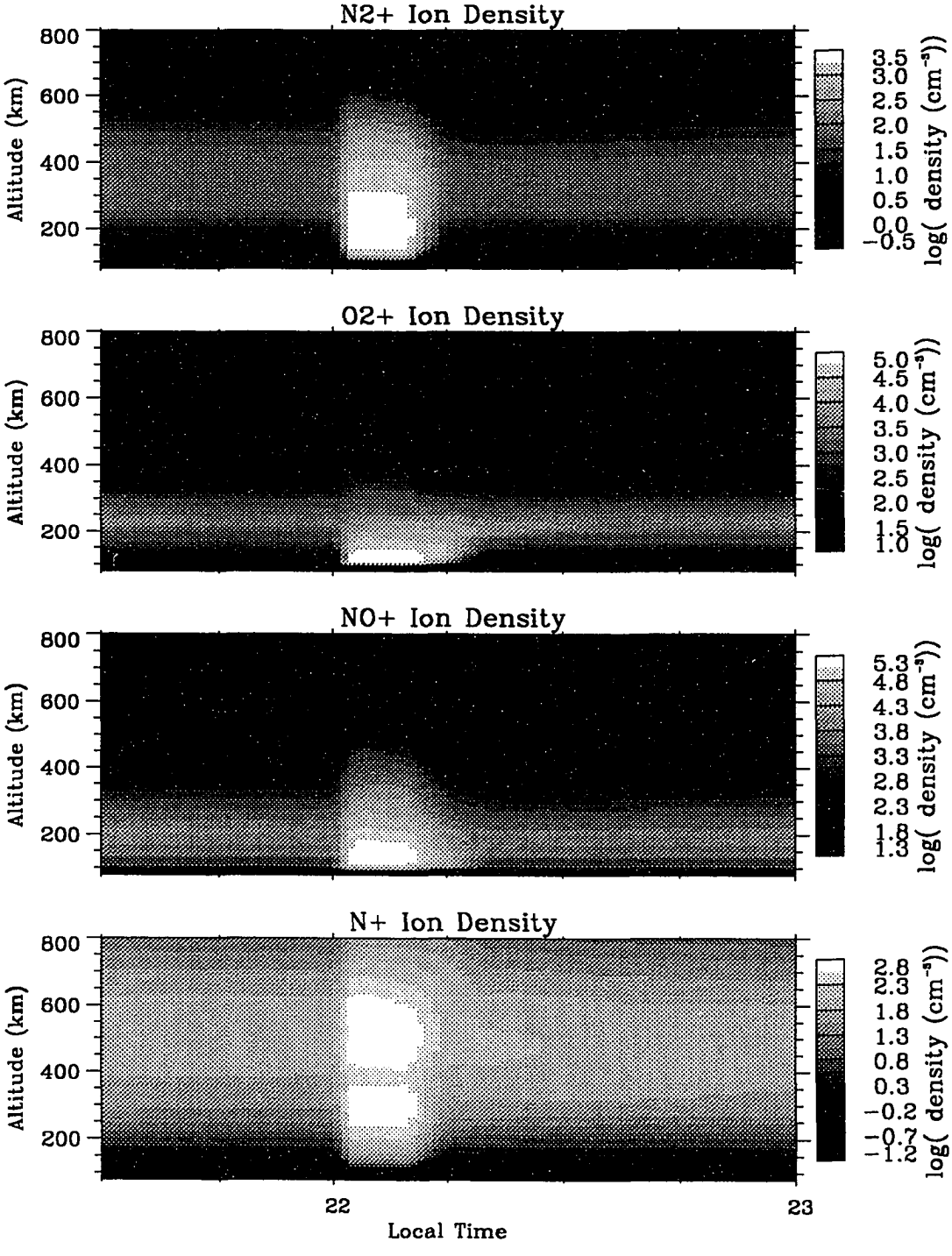

Figure 4.13 Ionospheric response to auroral electron bombardment: the time histories of densities of N_2^+, O_2^+, NO^+ and N^+ from 21:30 LT to 23:00 LT.

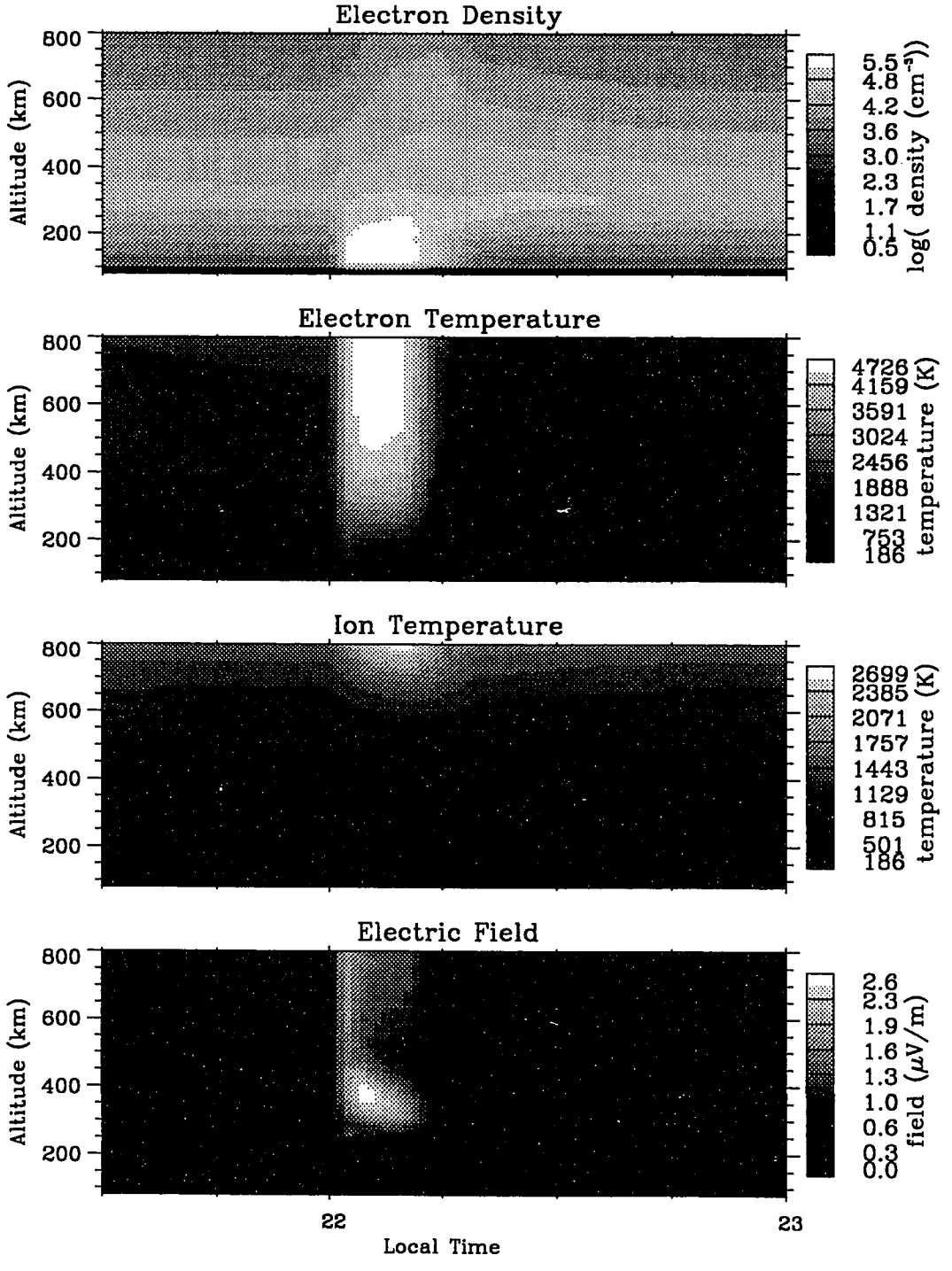

Figure 4.14 The time histories of electron density, electron temperature, ion temperature and polarization electric field from 21:30 LT to 23:00 LT in response to auroral electron bombardment.

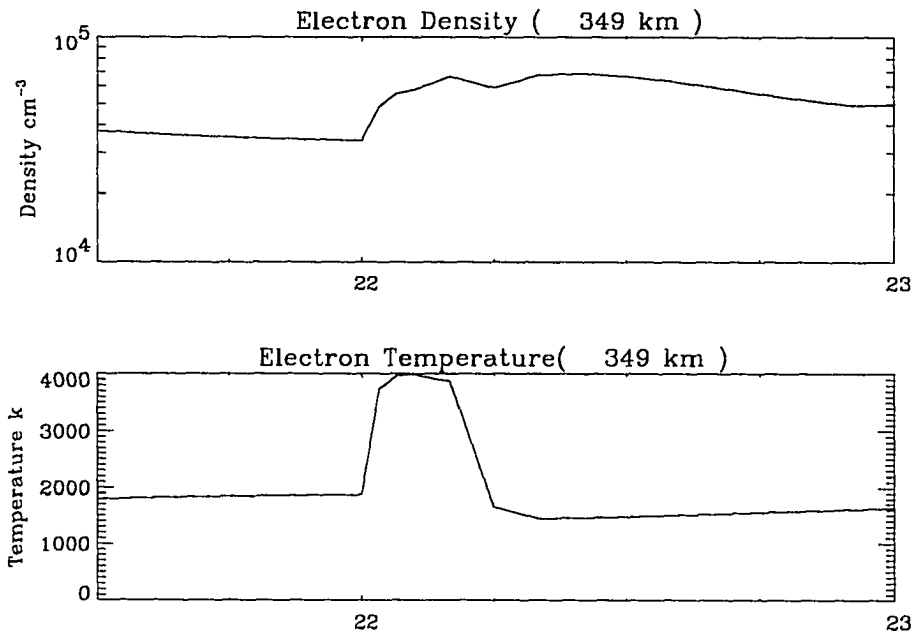

Figure 4.15 Temporal variation of the electron density and electron temperature at 349 km from 21:30 LT to 23:00 LT.

The long term effects of auroral precipitation on the ionosphere are illustrated in Figure (4.16) showing the electron density, the electron temperature and ion temperature during a period extending from four hours before to four hours after auroral bombardment. The auroral event occurs before midnight during the decay of the ionosphere. There is an electron density increase at *F*-region heights in the night-time ionosphere as a result of the auroral event, which lasts more than two hours. The electron and ion temperature contours show that two hours after the auroral event the magnitudes gradually return to the pre-auroral values.

4.2.2 Soft and Hard Electron Spectra Precipitation Events

Electron fluxes at the poleward edge of the auroral oval on the nightside usually have a spectral distribution that is significantly softer than typical auroral oval electron spectra. Electron

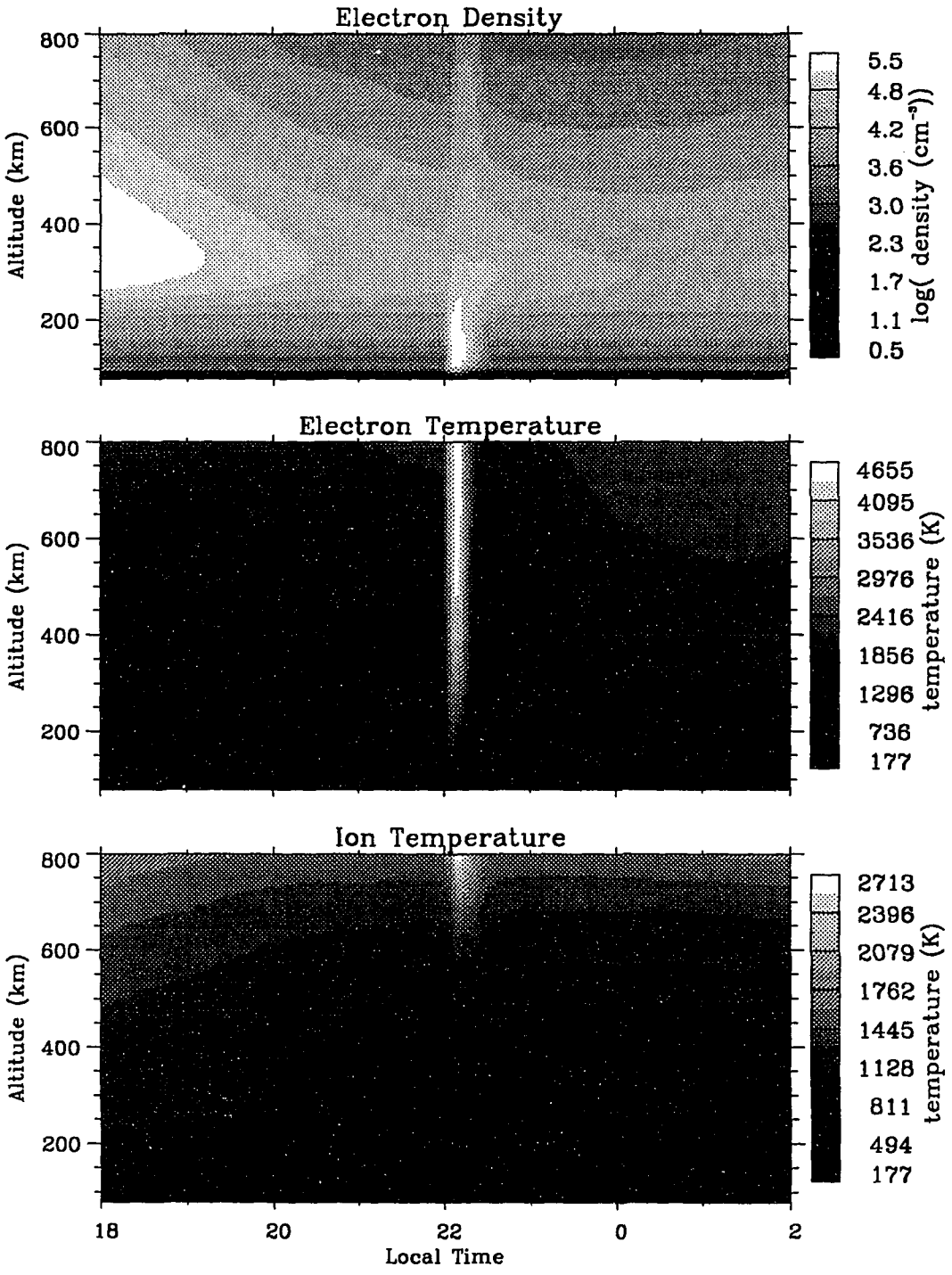

Figure 4.16 Ionospheric response to auroral electron bombardment: the time histories of electron density, electron temperature and ion temperature from 18:00 LT to 02:00 LT.

fluxes in an auroral arc, sometimes, have a hard electron spectrum. The results of two model calculations of aurora with particle spectra whose characteristic energy are 300 eV and 5 keV are presented in this section. The electron flux and the time history of the auroral event are the same as in the preceding section.

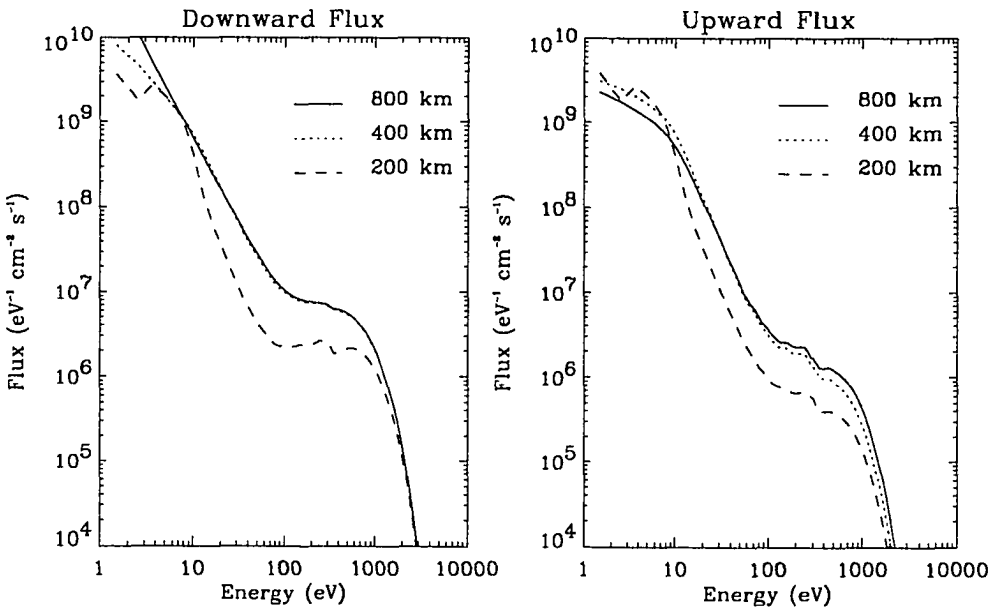

Figure 4.17 Same as Figure (4.8), but for the case of $\epsilon_{char} = 300$ eV.

The electron energy spectra computed with this model for an input flux distribution with characteristic energy of 300 eV are shown in Figure (4.17) at three altitudes. Altitude profiles of the ionization rate due to a flux of 5 erg cm^{-2} sec^{-1} precipitating along the magnetic field into the atmosphere, shown in Figure (4.18), illustrate the penetration of a soft electron flux. The maximum ionization rate of O^+ is 2.3×10^3 cm^{-3} sec^{-1} at an altitude of 192 km, which is lower

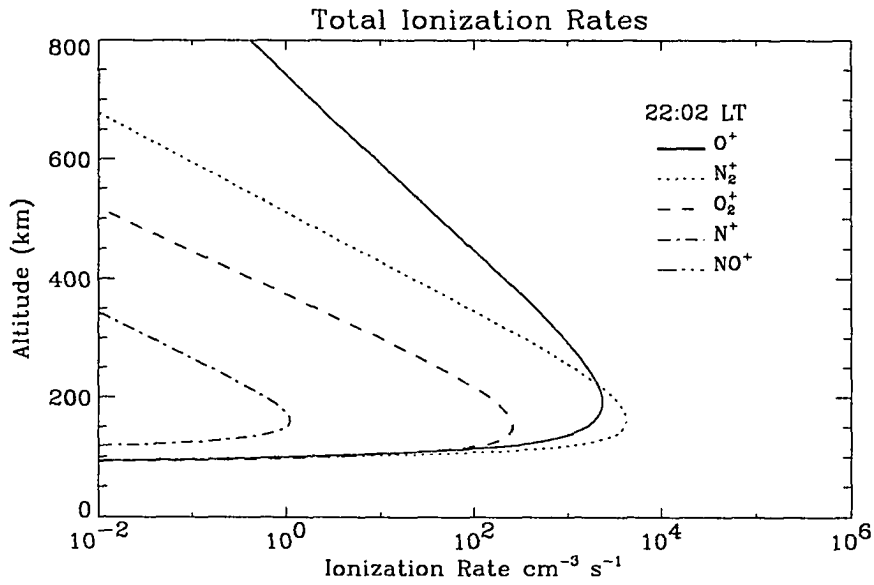

Figure 4.18 Same as Figure (4.10), but for the case of $\epsilon_{char} = 300$ eV.

in magnitude and higher in altitude than that caused by an auroral flux of 1 keV characteristic energy.

As a result of chemical reactions and transport, the electron and ion densities reach a maximum near 200 km. By 22:04 LT, the electron density at low altitude has reached a steady state, but in the upper ionosphere the build up of the density reached in four minutes is slow, resulting in the absence of an F-peak in Figure (4.19) compared with Figure (4.6). For a soft auroral electron flux more energy is deposited at high altitudes, resulting in higher electron and ion temperatures compared with the typical auroral event of $\epsilon_{char} = 1$ keV. The electron temperature reaches three times the pre-auroral value and is 2500° K higher than that shown in Figure (4.11). Figure (4.19) also shows a large increase in the ion temperature at high altitudes.

The soft auroral electrons produce a rapid increase in the ionospheric F_1-region electron density around 200 km as shown in Figure (4.20). The decay phase of this aurora is characterized by a decrease in the electron density that is slow, requiring three hours to approach pre-auroral

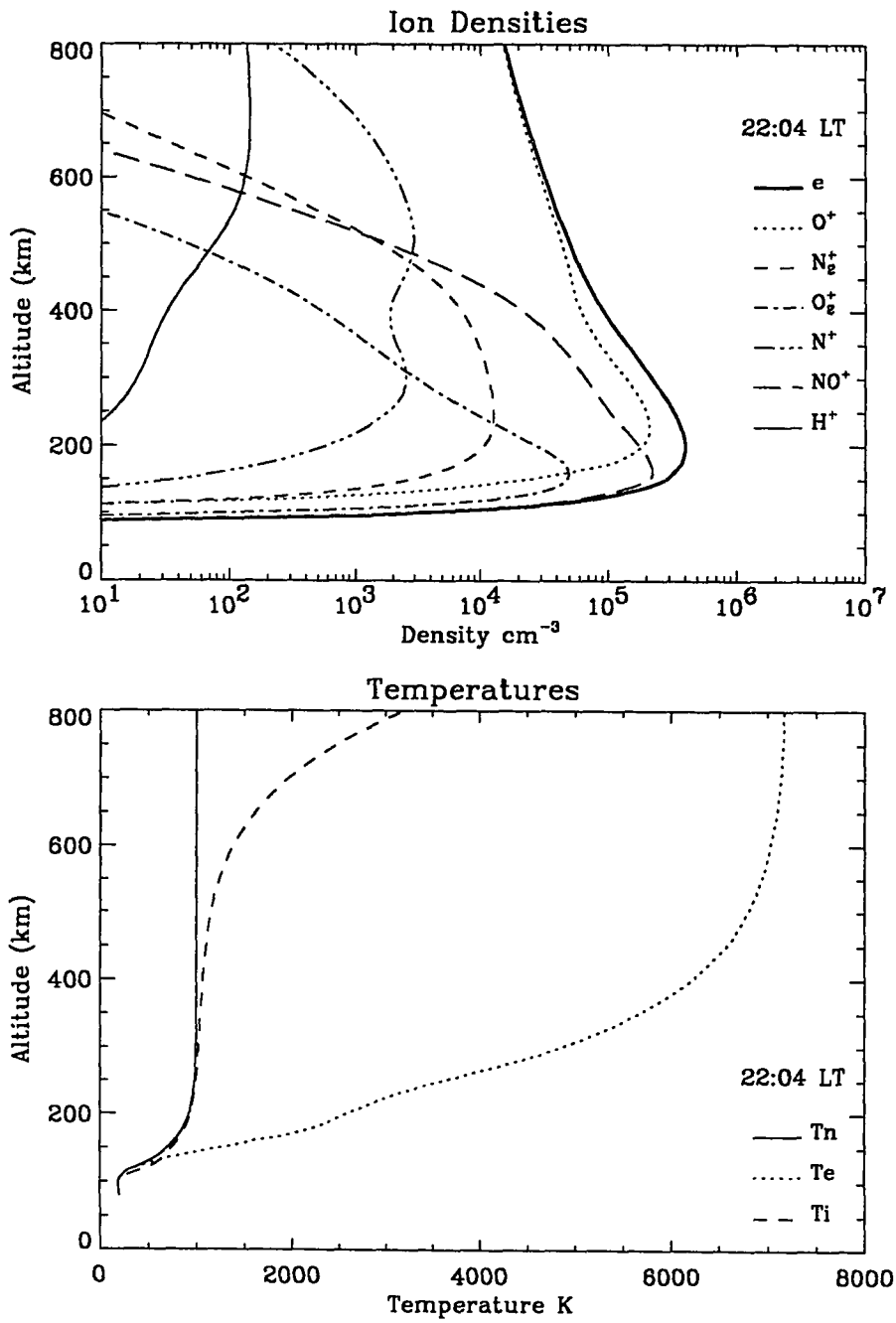

Figure 4.19 The ion composition and electron density profiles (top) and the electron, ion and neutral temperature profiles (bottom) at 22:04 LT for the case of $\epsilon_{char} = 300$ eV.

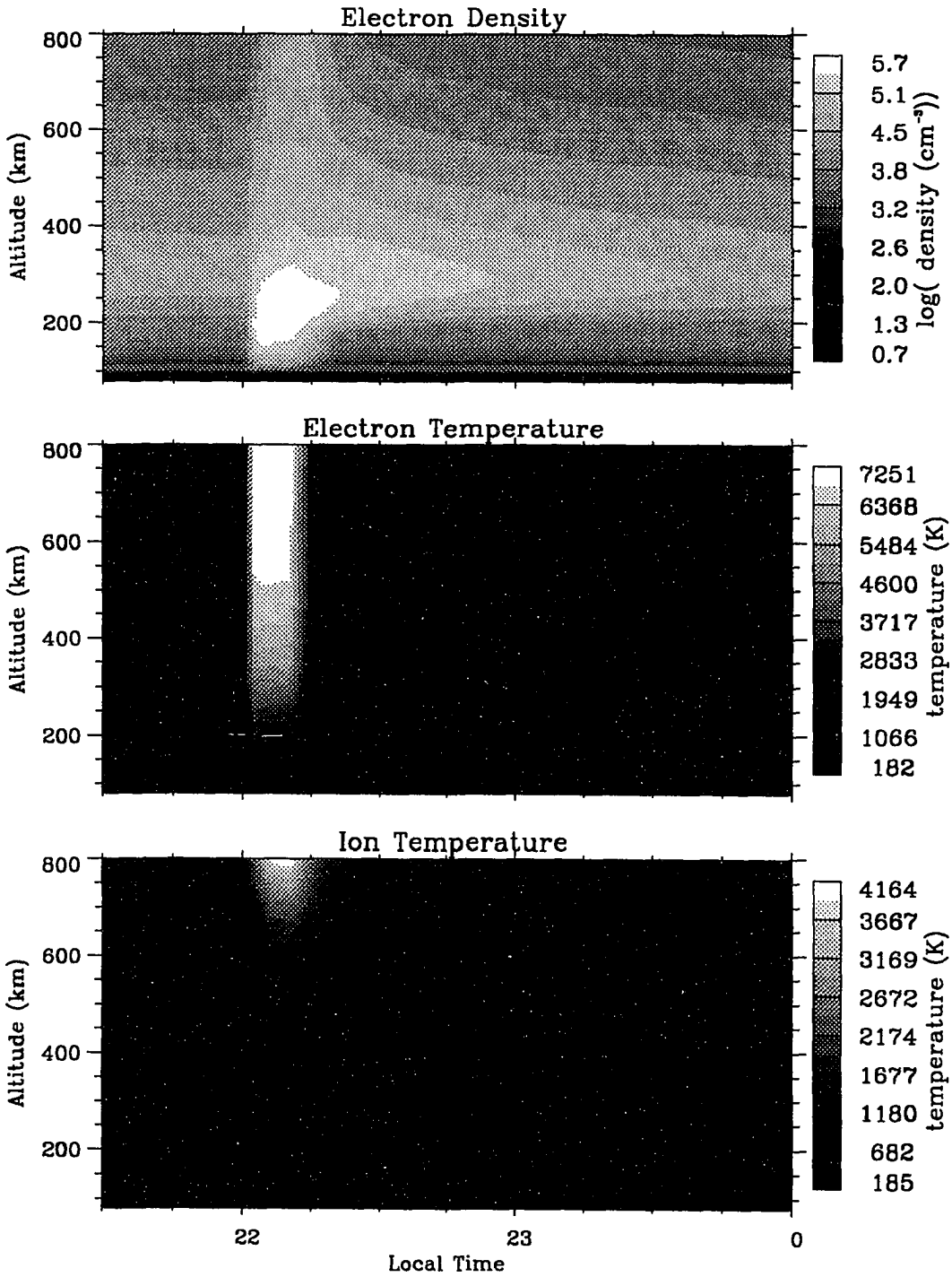

Figure 4.20 The time histories of electron density, electron temperature and ion temperature from 21:30 LT to 24:00 LT in response to the soft auroral electron bombardment.

levels at high altitude. The calculated electron and ion temperatures for this aurora are also shown in Figure (4.20). The assumed soft flux penetrates less deeply into the atmosphere than the 1 keV electron spectrum and heats the ambient electron gas to higher temperatures for the same input energy flux. This illustrates the efficiency of soft electron aurora in raising the electron temperature at *F*-region heights.

The results of a similar calculation, but for a hard auroral electron spectrum, are shown in the following figures. The spectrum for this aurora peaks at 5 keV and has an incident electron energy flux of 5 erg cm^{-2} s^{-1}. Such a hard spectrum aurora penetrates deeply into the atmosphere, heating the ambient electrons and ions as well as enhancing the ionization rate which increases the ion concentrations. Ionization rates for this case are shown in Figure (4.21). The peak rate of O^+ is 5.9×10^3 cm^{-3} sec^{-1} at an altitude of 101 km.

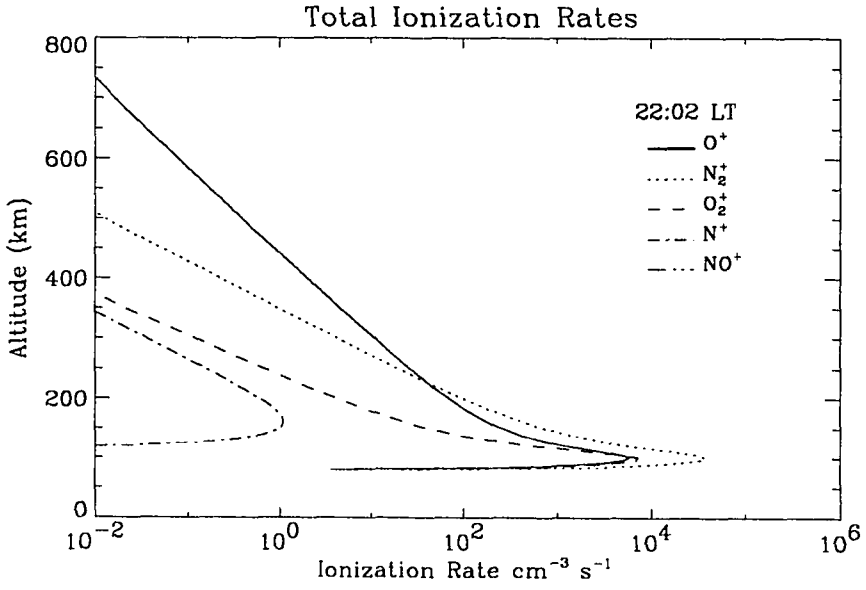

Figure 4.21 Same as Figure (4.10), but for the case of $\epsilon_{char} = 5$ keV.

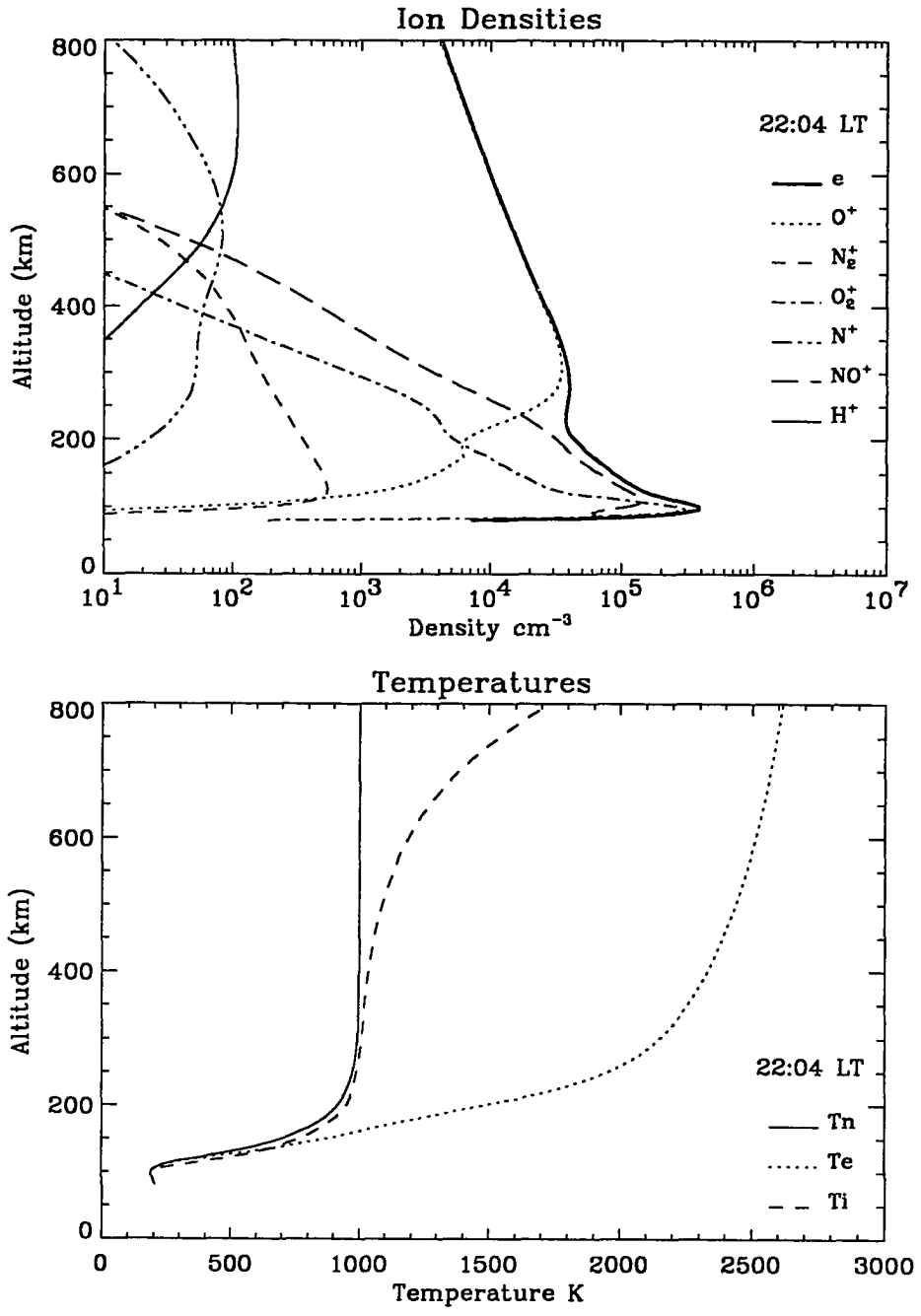

Figure 4.22 The ion composition and electron density profiles (top) and the electron, ion and neutral temperature profiles (bottom) at 22:04 LT for the case of $\epsilon_{char} = 5$ keV.

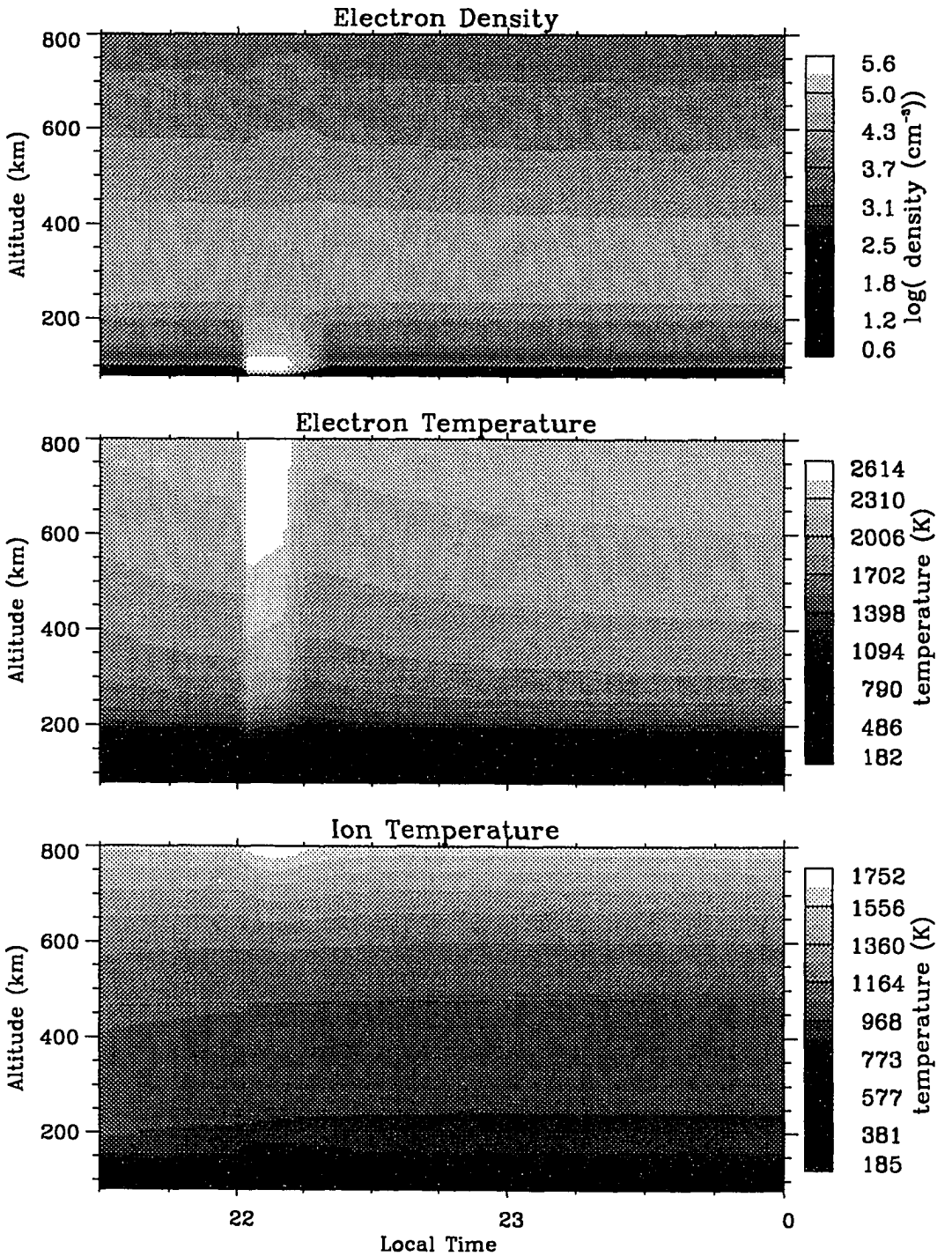

Figure 4.23 The time histories of electron density, electron temperature and ion temperature from 21:30 LT to 24:00 LT in response to the hard spectrum auroral electron bombardment.

The ion composition resulting from hard electron precipitation, four minutes after the aurora is turned on, is shown in Figure (4.22). The differences in the ion concentrations due to various auroral electron spectra, shown in Figures (4.11), (4.19) and (4.22), result from a combination of the effects of direct impact ionization, chemical reactions and transport. The calculated temperatures are slightly lower for the same electron energy flux but the general shape of the altitude profiles is similar to the 1 keV case.

The auroral *E*-region produced by the hard spectrum aurora is rapidly formed, as illustrated in Figure (4.23). The *F*-region electron density responds more slowly, thereby demonstrating that the major effects of this aurora occur at *E*-region heights. The hard spectrum aurora produces a strong *E*-region with electron densities of 5.0×10^5 cm^{-3} near 100 km. The electron and ion temperatures display characteristics similar to those derived for the auroral spectrum of 1 keV; however, enhanced electron and ion temperatures are found at altitudes as low as 100 km.

4.3 Auroral Events During Daytime

To investigate the ionospheric response to auroral electron bombardment under sunlit condition, an auroral electron Maxwellian spectrum of 1 keV characteristic energy is assumed to occur during daytime. In this case, electron precipitation with energy flux of 5 erg cm^{-2} sec^{-1} is turned on at noon, when photoionization caused by solar EUV controls to the maintenance of the ionosphere and also produces energetic photoelectrons as an embedded source. The differential electron flux computed from our model aurora is shown in Figure (4.24) at 800, 400 and 200 km, which illustrates the combination of transport of auroral electrons and photoelectrons. The downward flux at 800 km is the imposed boundary value representing auroral electrons. The

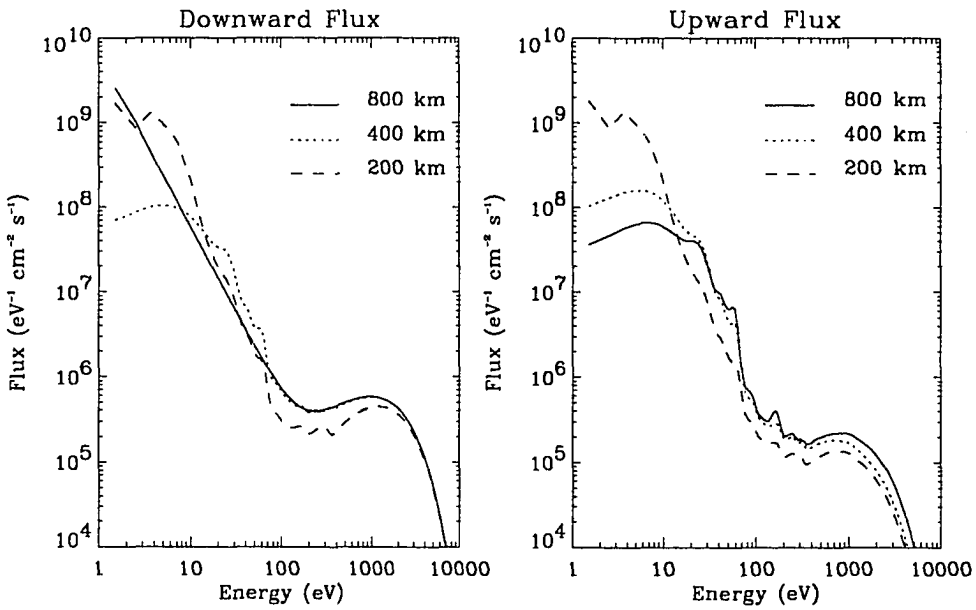

Figure 4.24 The downward and upward fluxes at 3 different altitudes from an isotropic Maxwellian input spectrum with $\epsilon_{char} = 1$ keV and an embedded source of photoelectrons. The 800 km downward flux constitutes the boundary condition. At low energy (below 100 eV) a powerlaw with ϵ^{-2} was added to the Maxwellian distribution.

structure below 200 eV is attributed to the embedded primary photoelectrons shown in Figure (4.1).

Contours of the resulting ionization rate, electron density, electron and ion temperatures, presented in Figure (4.25), show a significant increase over undisturbed daytime values. The solar EUV ionization rate provides a large background on which auroral ionization is superimposed, producing a large enhancement in the *E*-region. The percentage change in the ionization rate is smaller than under night-time conditions, as may be seen by comparing magnitudes before, during and after auroral precipitation. The electron density of the undisturbed daytime ionosphere is so large that the effect of auroral electron precipitation is small by comparison with the night-time case. Most of the increase in electron density occurs at the *E*-region near 120 km. Only a small

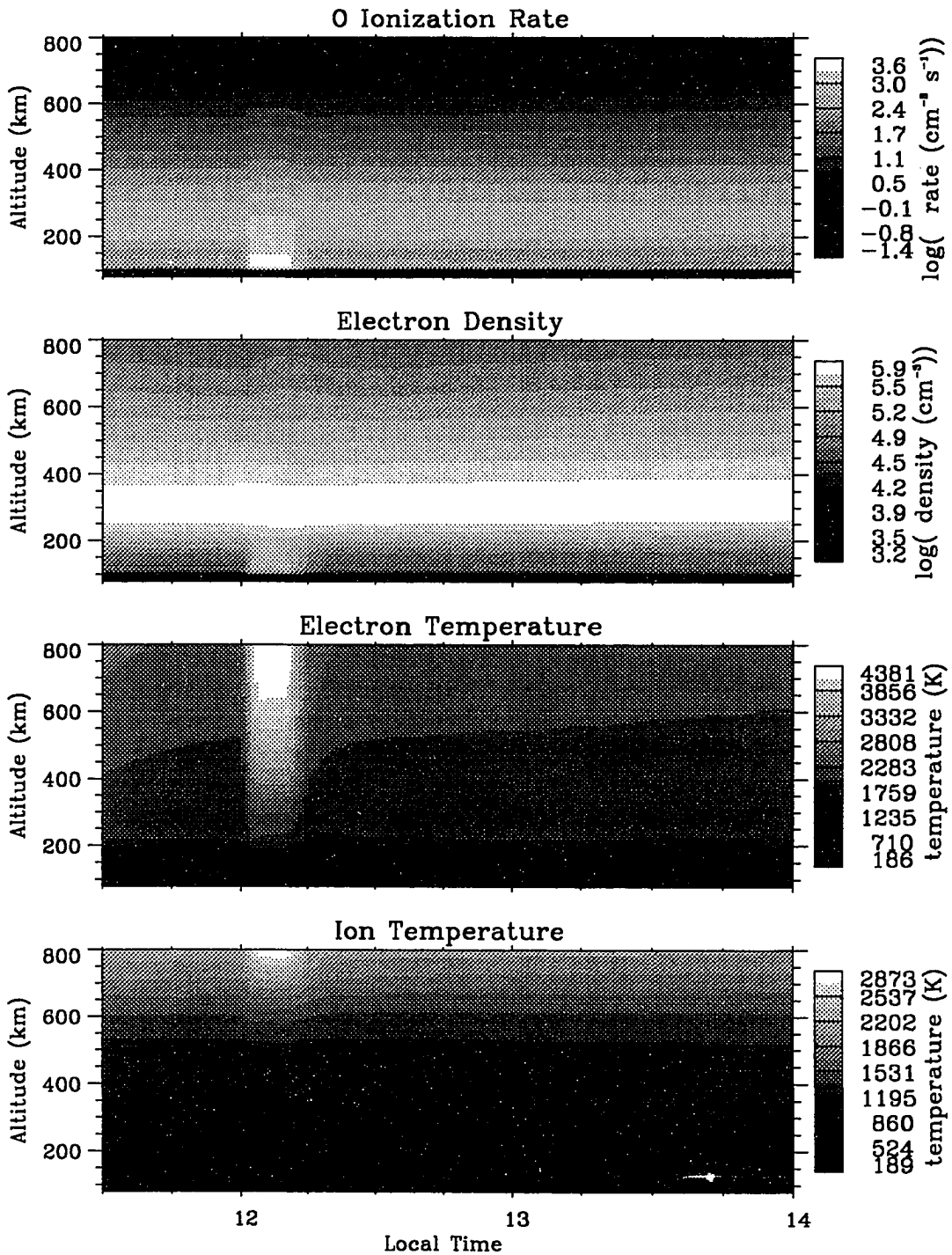

Figure 4.25 Ionospheric response to aurorai electron bombardment during daytime: the time histories of O^+ ionization rate, electron density, and electron and ion temperatures from 11:30 LT to 14:00 LT.

enhancement of the electron density occurs in the *F*-region. The enhancement of electron density in the *F*-region shows a time lag with respect to the auroral electron precipitation, as a result of transport of ionization from the *E*-region to the *F*-region. The electron and ion temperatures are enhanced by auroral electrons and photoelectrons. The perturbation is due to secondary auroral electron heating, but the energy is shared among a larger number of electrons than in the night-time event. As a result, the increase in electron temperature is considerably less than for night-time conditions, but the ion temperature increase more than for night-time conditions.

CHAPTER 5

The Effects of Fields on Electron Distributions and on Ionospheric Conductivities

The effects of a parallel electric field and the geomagnetic field on auroral and photoelectron energy distributions are studied in this chapter. Ionospheric conductivities are calculated by using the time varying auroral model discussed in the previous chapters.

5.1 The Effects of $E_{\parallel}$ and the Geomagnetic Field

The self-consistent parallel electric field has three contributions that arise from the electron density and electron temperature gradients and from a field aligned current. If the field aligned current is attributed to the flow of suprathermal (i.e. auroral and photoelectron) electrons only, and the parallel conductivity is assumed to be due to collisions, then the $\mathbf{J}/\sigma_e$ term is small compared with the gradient terms. Measurements of the geomagnetic field perturbations in the topside ionosphere have shown, however, that the actual current may be much larger than the energetic component would suggest, implying the presence of a substantial thermal component of the current. If an "anomalous" resistance is present in the topside ionosphere under auroral precipitation conditions, then the contribution of the current terms to the parallel electric field may be much larger than the minimum associated with the polarization effect. This possibility will be discussed by including an arbitrary additional term in equation (2.2). For the purpose of this study it is assumed that this field is maintained by the field aligned auroral currents in the vicinity of an auroral arc. The precipitating electrons are affected by this field. These electrons constitute the major heat source for the ambient thermal electrons and it is to be expected that a parallel electric field will thus influence the electron temperature. Joule heating by parallel electric fields

of the magnitude adopted here is negligibly small and is neglected as a direct heat source for the thermal electron population. To evaluate the consequences of a parallel electric field and the Earth's dipole magnetic field on the energy distribution of electron fluxes I have carried out numerical calculations of the coupled electron transport, ion continuity, and energy equations for an auroral event representing an external flux source and for a solar case representing an embedded source of photoelectron.

5.1.1 The Auroral Case

The auroral case is illustrated with an analytic Maxwellian electron spectrum with characteristic energy of 1 keV and an energy flux of 5 erg cm^{-2} s^{-1}, supplemented by a power law spectrum with energy dependence ϵ^{-2} below 100 eV. Such a spectrum is representative of observed auroral events (c.f. *Winningham et al.*, 1977; *Pulliam et al.*, 1981; *Lummerzheim et al.*, 1989). The auroral electron flux is imposed at the upper boundary at 800 km. At the lower boundary of 80 km zero backscattered flux is assumed in the transport equation. The assumed input parameters and boundary conditions for ion continuity equations and electron and ion energy equations are the same as discussed in Chapter 4.

The self-consistent polarization field associated with the auroral event specified above and computed from equation (2.2) is shown in Figure (5.1). The dominant term is the electron density gradient, yielding an upward directed field of about 3 μV/m at 350 km and a near constant value of 1.5 μV/m above 500 km. The temperature gradient term produces a downward directed field since the gradient is positive at all altitudes. The electric field due to the current density term is small and directed upward. Only the current carried by the energetic flux is included in this term which is smaller than the field aligned current inferred from measurements of magnetic field perturbations recorded by instruments on board satellites and rockets overflying auroral arcs (c.f.

Lanchester and Wallis, 1985; *Lanchester and Rees*, 1987). A reversal, to a downward directed $E_{||}$, occurs at about 200 km but this has no effect on the electron intensity distribution which is controlled entirely by collisional interactions below about 300 km.

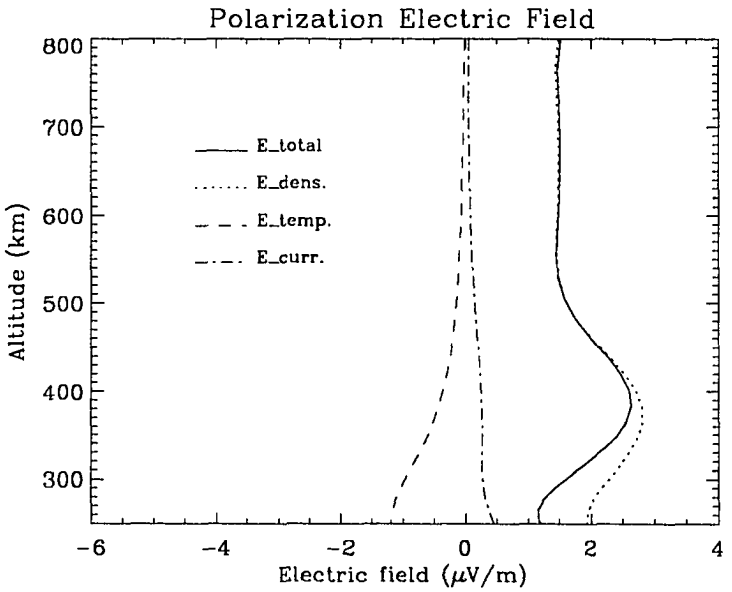

Figure 5.1 Altitude profiles of the polarization field for the auroral case presented in the text. The total field as well as terms corresponding to the density gradient, temperature gradient and current are shown. Positive values signify upward directed fields.

The differential electron flux computed from this model aurora is shown in Figure (4.8) at 800, 400 and 200 km and discussed in Section 4.2.1. To assess the contributions of fields to the structure of the differential fluxes the calculations have been repeated under four different assumptions: a) no magnetic field gradient and no polarization field, b) no magnetic field gradient and a self-consistent $E_{||}$, c) a dipole magnetic field and a self-consistent $E_{||}$ (leading to the results in Figure (5.1)), and d) a dipole magnetic field and an $E_{||}$ consisting of the polarization field and an additional 10 μV/m component. The results are displayed in different ways in Figure (5.2) and

(5.3). The downward and upward directed hemispherical fluxes at 800 km and 400 km are shown in Figure (5.2) to illustrate the different effects of the magnetic and electric fields. At 800 km the downward flux is the imposed boundary condition while the upward flux shows the effect of deceleration, decreasing slightly with increasing parallel electric field at electron energies below 100 eV. The magnetic mirror force has the effect of increasing the flux at electron energies above a few hundred eV. The 400 km altitude regime is closer to the embedded source of secondary electrons and the decelerating effect of the electric field is offset by the increased source term. The collision terms likewise tend to decrease the field effects. Even so, a 10 μV/m parallel electric field and the polarization field have a net effect of increasing the low energy part of the electron flux. Figure (5.3) illustrates the same point. The downward component of the 2 keV flux is unperturbed over the entire altitude range while the upward flux shows the effect of the magnetic mirror force above about 300 km altitude. The factor of two increase at 800 km in the backscattered flux should produce effects such as an increase in the electron temperature and enhancement of optical emissions that may be observed. The parallel electric field is entirely responsible for perturbations in the 10 eV electron flux. Profiles of the upward and downward fluxes, shown in Figure (5.3), illustrate the combined effects of the embedded source region, the accelerating/decelerating electric field, and the elastic and inelastic scattering processes. For different boundary conditions, i.e. the electron flux at the top of the atmosphere, the contribution of the various terms in the transport equation will, of course, differ from the case illustrated in Figure (5.3).

Observations of large parallel current densities at edges of auroral arc structures suggest the development of parallel electric fields due to non-ohmic resistance [*Papadopolous*, 1977, *Stasiewicz*, 1984]. The consequences of imposing a uniform upward directed parallel electric field, in addition to the self-consistent polarization field, have been investigated; magnitudes of 10, 20, and 30 μV/m were adopted. Since the largest effect of an $\mathbf{E}_{||}$ is on the electron flux

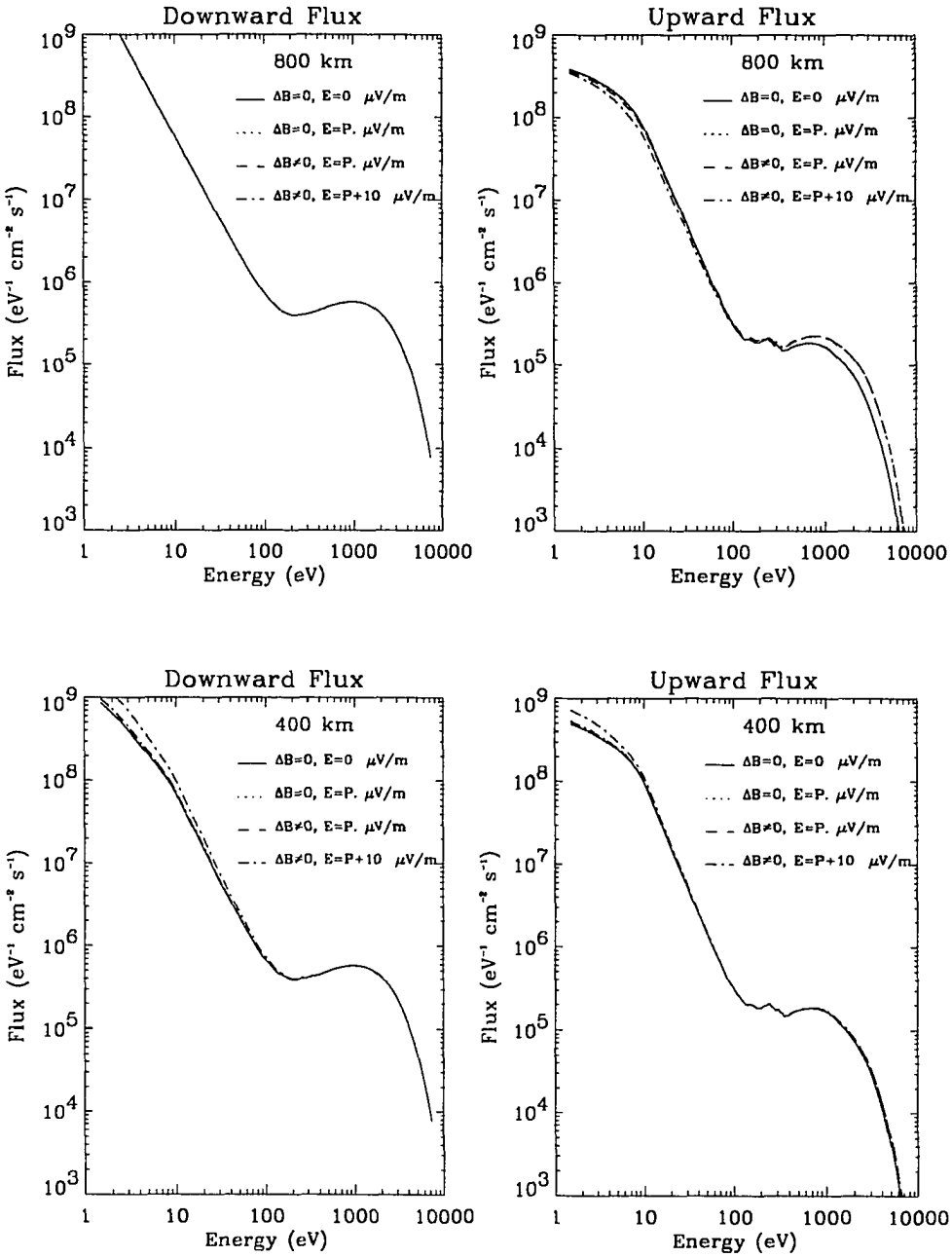

Figure 5.2 Electron energy spectra of downward and upward hemispheric fluxes at 800 km and 400 km for four different cases: no electric field and a homogeneous magnetic field (solid lines); a polarization field and a homogeneous magnetic field (dotted lines); a polarization field and a divergent magnetic field (dashed lines); polarization field plus an imposed electric field of 10 μV/m and a divergent magnetic field (chain-dotted lines).

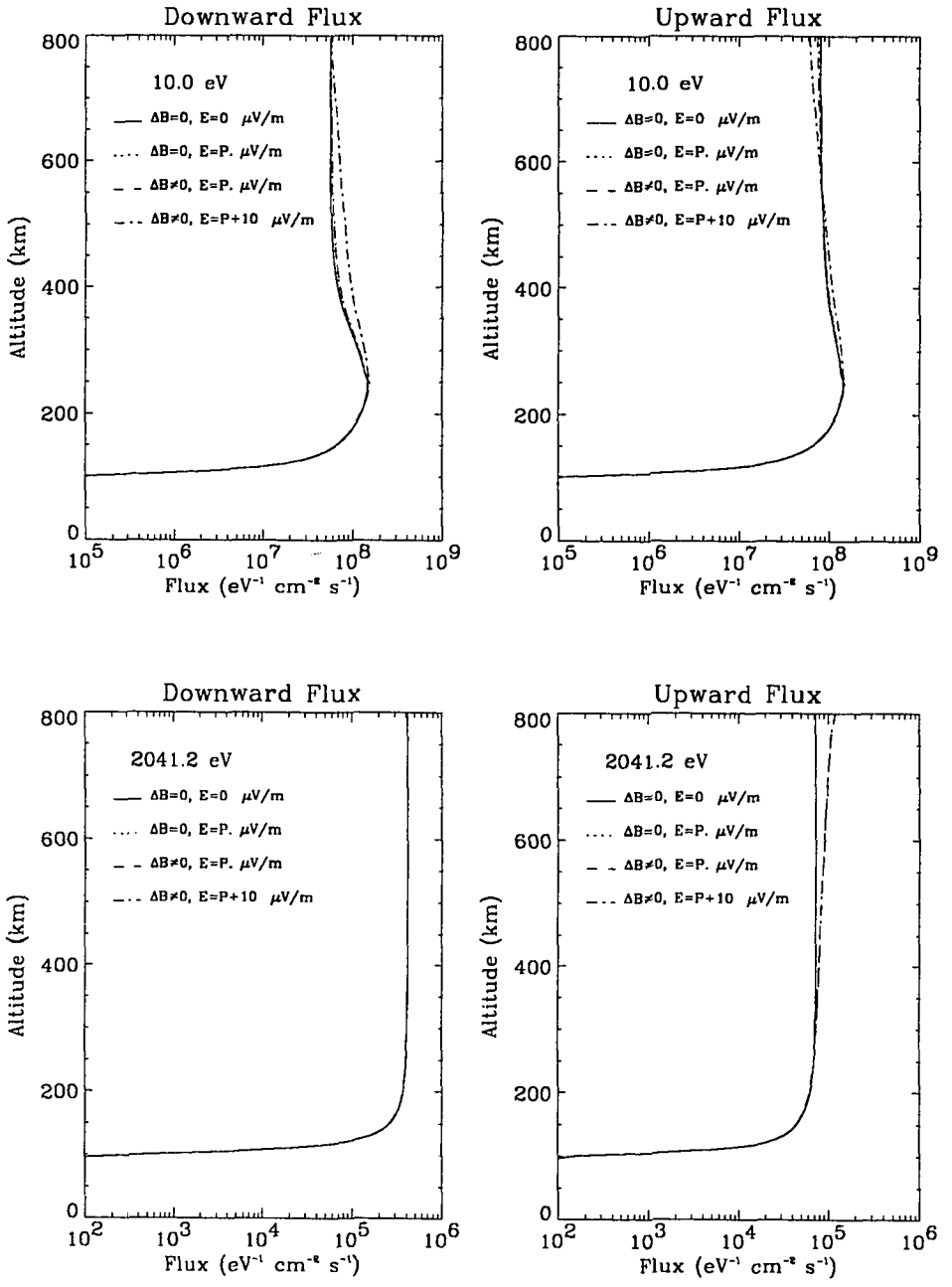

Figure 5.3 Altitude profiles of the downward and upward hemispheric fluxes of 10 eV and 2 keV electrons for the four different cases shown in Fig. (5.2).

below 100 eV, the results of the enhanced $E_{||}$ are shown in the energy range between 10 and 100 eV. The curves in Figure (5.4) essentially expand upon the results shown in Figure (5.2): the downward flux at the upper boundary of 800 km is given, while the upward moving electrons are decelerated; the upward flux is also decelerated at 400 km but this term is overshadowed by the embedded source and scattering terms; the downward flux at 400 km undergoes substantial acceleration, increasing the 10 eV flux by a factor of three for the 30 μV/m electric field. Height profiles of the 10 eV downward and upward fluxes are shown in Figure (5.5). A factor of three enhancement in the omnidirectional flux at 400 km is predicted for a 30 μV/m parallel electric field. The Figure shows that the altitude at which the upper boundary is imposed produces a response in the downward flux that is not realistic. More likely, the increase in the flux under the influence of an $E_{||}$ should persist at the boundary. However, deceleration of the upward flux may result in little change of the omnidirectional flux.

As mentioned above, an upward parallel electric field is expected to decelerate electrons upward, leading to a flattening of the spectral shape of the low-energy electron distribution. *Fung and Hoffman* [1991] investigated the variation of the low-energy portion of the secondary electron spectrum from the DE-2 satellite. The statistical results indicated the secondary electron spectral index (power-law) decreased by an amount between 0.04 to 0.22, with an average decrease of 0.13 from 400 to 900 km. The amount of spectral flattening can be explained by an encounter with a potential difference between 400 and 900 km. Figure (5.4) shows the sensitivity of the index of the downward and upward electron spectra (10 - 100 eV) to the presence of a potential drop between 400 and 800 km. It illustrates variations of the spectrum index due to the different potential drops of 4, 8, 12 V in addition to the potential drop due to polarization field (about 0.67 V). The rate of spectral steepening or flattening is not linear but depends on the imposed electric field strength; the average rate of steepening or flattening of the corrected spectrum is about 0.026 V^{-1}. The DE-2 measurements show that there can be a distributed parallel electric field of

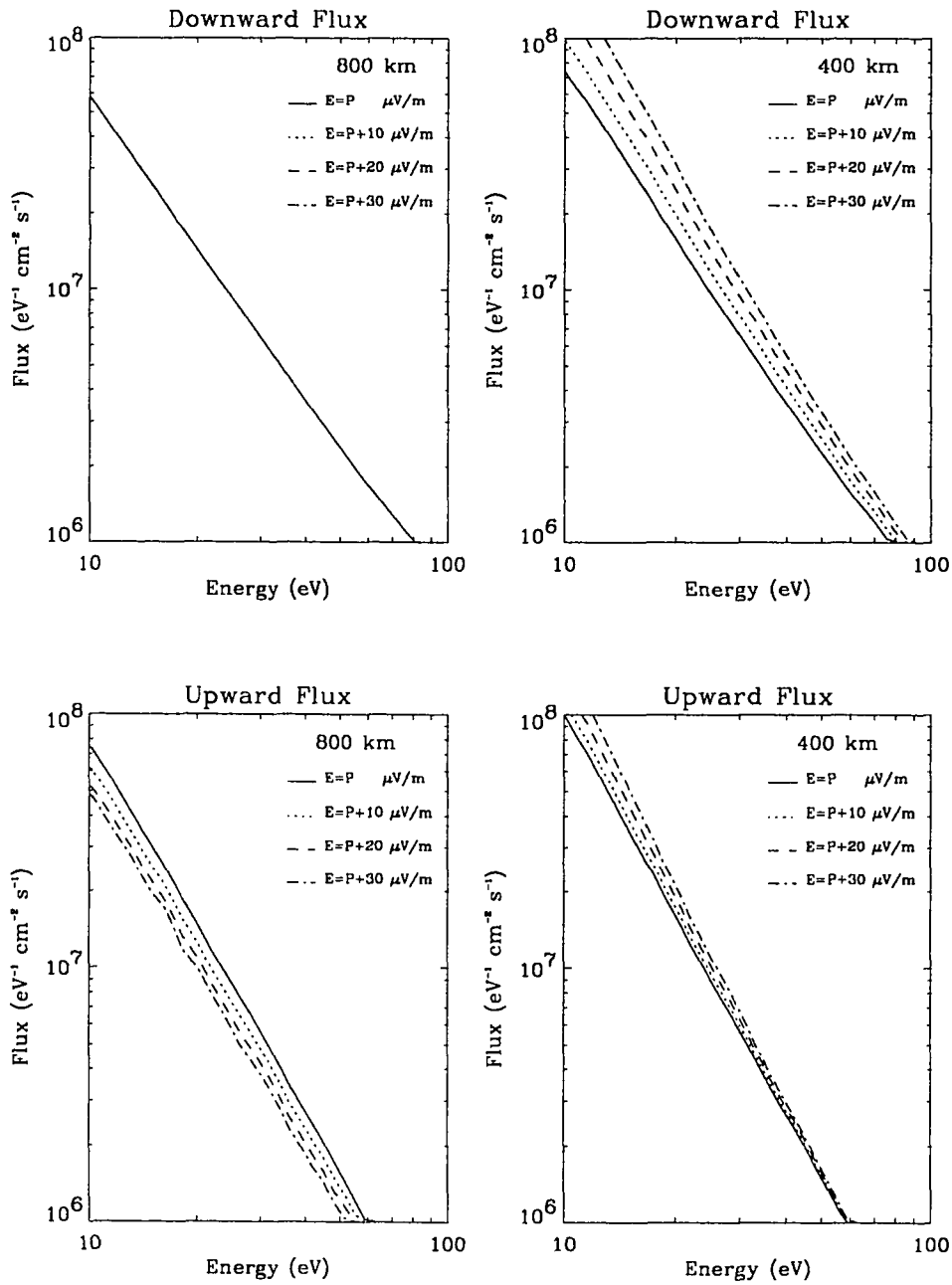

Figure 5.4 Electron energy spectra between 10 and 100 eV of the downward and upward hemispheric fluxes at 800 km and 400 km for the auroral example described in the text. Results are shown for the baseline polarization electric field (labeled E=P) and three values of enhanced parallel electric fields: 10, 20 and 30 μV/m.

10 μV/m in addition to the polarization field between 400 and 900 km altitudes, corresponding to an average potential drop of 5 volts. The reason for different results between *Fung and Hoffman*'s heuristic model and this model is that electron transport is calculated with the present model by including all sources and sinks. The internal sources and sinks make the low-energy spectrum less sensitive to the presence of a potential drop.

The omnidirectional electron flux is the parameter used to compute auroral ionization, plasma temperature enhancements, and auroral spectral emission features. Optical emissions do not influence the electron flux; the energy is radiated out of the region of excitation. Ionization and the electron temperature appear in various terms of the transport equation, necessitating the coupled solutions of the transport, continuity and energy equations described in preceding chapters. It is of interest, therefore, to investigate the effects of the assumed parallel electric field on the electron density and temperature profiles. The results are shown in Figure (5.6) for the auroral case, referenced to the baseline polarization field calculations. The electron density profile is influenced very little by a parallel field up to 30 μV/m. This is to be expected because ionization cross sections have maxima between about 100 eV and 200 eV and in this energy range the electron flux is not significantly perturbed by the electric field. Heating of the ambient electron gas is most efficient in collision with low energy auroral electrons (c.f. equation (2.5)) and it is this population that is most sensitive to the influence of electric fields. The electron temperature above 200 km is therefore enhanced by the application of an $E_{||}$, as shown in the Figure (5.6). The magnitude of the electron temperature above about 400 km is determined not only by local collisional heating but also by a heat flux conducted down from the magnetosphere. This flux is an imposed boundary condition on the energy equation and therefore arbitrary in this example.

Excitation thresholds of several prominent auroral emission features lie in the energy regime of a few eV, notably the $O(^1D)$ and $O(^1S)$ states and the $N(^2D)$ and $N(^2P)$ states. Electron impact is an important source of $O(^1D)$ and its excitation rate is directly proportional to the magnitude

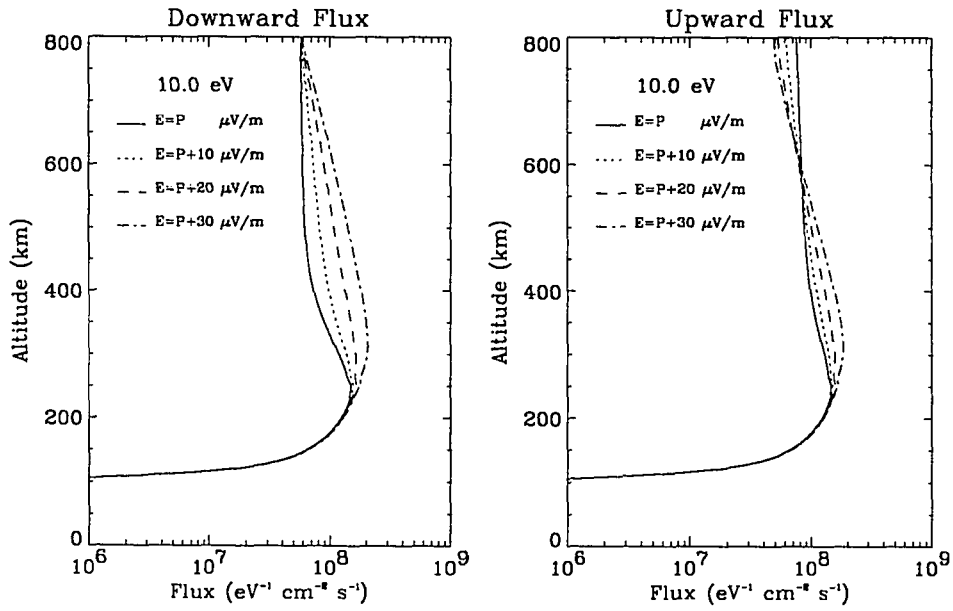

Figure 5.5 Altitude profiles of the downward and upward hemispheric fluxes of 10 eV electrons for the different magnitudes of parallel electric field: polarization field (solid lines); polarization field and 10 μV/m (dotted lines); polarization field and 20 μV/m (dashed lines);polarization field and 30 μV/m (chain-dotted lines). The behavior of the downward flux at the upper boundary is discussed in the text.

of the electron flux. A parallel electric field may, therefore, substantially increase the excitation rate of $O(^1D)$ at an altitude where collisional deactivation is minimal. An increase of the electron temperature further enhances excitation of $O(^1D)$. While thermal excitation has been included in current models of the 6300 Å emission, the enhancement of the low energy electron flux by a parallel electric field has not been included and could be substantial.

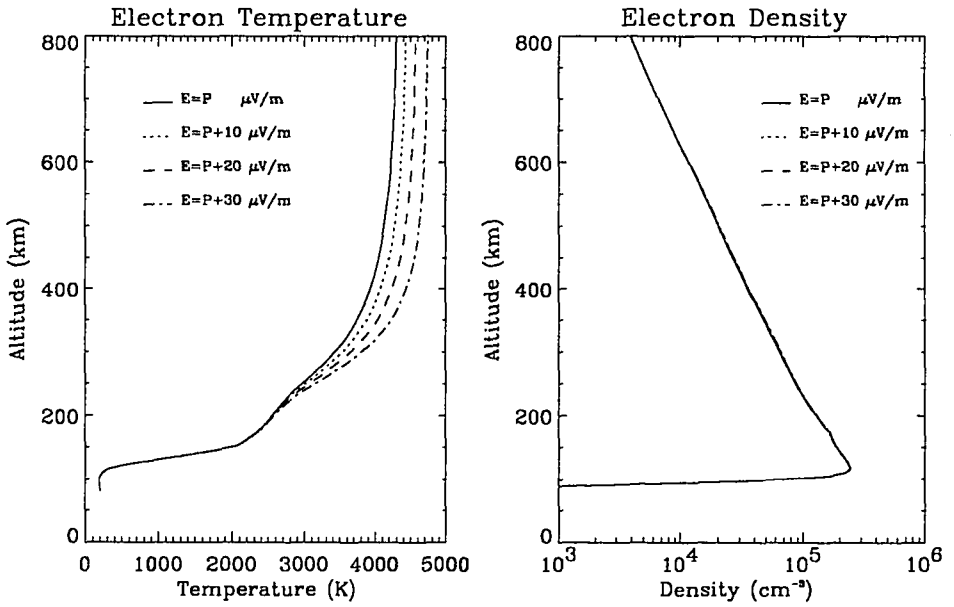

Figure 5.6 Altitude profiles of electron density and temperature for the different magnitudes of electric field polarization field only (solid lines); polarization field and 10 μV/m (dotted lines); polarization field and 20 μV/m (dashed lines); polarization field and 30 μV/m (chain-dotted lines).

5.1.2 The Photoelectron Case

The effects of a parallel electric field on the photoelectron flux in the absence of any auroral precipitation are investigated. The source of photoelectrons is embedded in the atmosphere, supplemented by a small external flux from the conjugate hemisphere. Several investigators have solved the photoelectron transport problem (e.g. *Banks and Nagy*, 1970; *Oran and Strickland*, 1978; *Link*, 1992) but none have included a self-consistent polarization electric field or larger values of parallel electric fields. The photoelectron source and transport calculation presented here have been compared with results of previously published photoelectron transport calculations [*Meier et al.*, 1985; *Link*, 1992] and good agreement was found.

Following the suggestion of *Winningham et al.* [1989] a small conjugate photoelectron flux is included by specifying a downward flux of 0.01 erg cm^{-2} s^{-1} with a characteristic energy of 50 eV at the upper boundary. Solving the coupled electron transport, ion continuity and energy equations, as previously described, the height profile of the polarization electric field is obtained and is shown in Figure (5.7). The upward directed field is almost constant above 400 km at a level of about 1 μV/m. The major contribution is due to the electron density term.

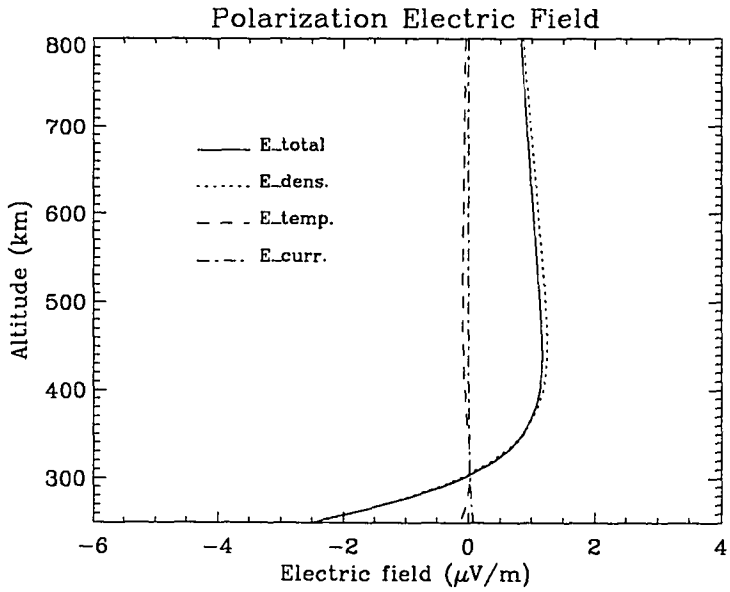

Figure 5.7 Altitude profiles of the polarization field for the photoelectron case. The total field as well as terms corresponding to the density gradient, temperature gradient and current are shown. Positive values signify upward directed fields

The downward and upward components of the photoelectron flux are shown in Figure (4.2) at three altitudes. Comparison with Figure (4.8) (the auroral case) shows the difference produced by the embedded source which attains a maximum at about 200 km altitude. The upward flux at 800 km in the 10 to 40 eV energy region exceeds the downward flux by an order of magnitude to become a source of conjugate photoelectrons. The result of solving the coupled governing

equations shows that the contributions of various terms (sources, sinks, elastic scattering, inelastic processes, polarization field, dipole magnetic field, etc.) makes it virtually impossible to predict by handwaving arguments the evolution of the electron flux with altitude. Detailed transport calculations coupled with the ion chemistry and energetics are required to model the response of the atmosphere to solar ionization.

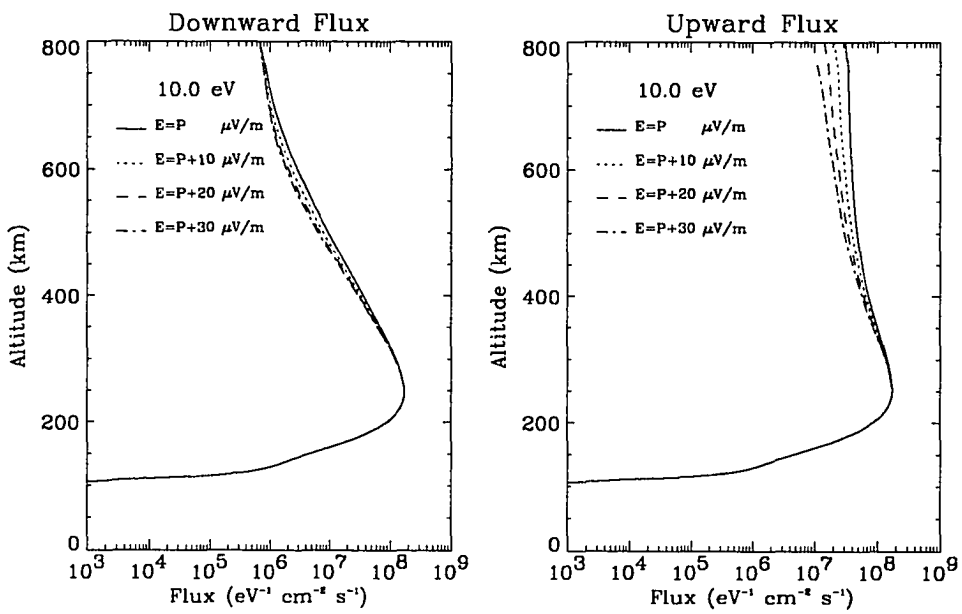

Figure 5.8 Altitude profiles of the downward and upward hemispheric fluxes of 10 eV photoelectrons for the different magnitudes of parallel electric fields: polarization field only (solid lines); polarization field and 10 μV/m (dotted lines); polarization field and 20 μV/m (dashed lines); polarization field and 30 μV/m (chain-dotted lines).

Electron fluxes computed including the self-consistent parallel electric field, and electron fluxes computed without including the effects of this field exhibit only small differences. Uncertainties in the solar EUV flux outweigh these changes of the photoelectron flux. Artificially increasing the magnitude of the parallel electric field has little effect on the downward flux component of photoelectrons but significantly decreases the upward flux, as shown in Figure (5.8).

The response differs from the auroral case shown in Figure (5.5) where the source of secondary auroral electrons is deeper in the atmosphere and the backscattered electron population reflects the increase in energy of the downward flux.

Parallel electric fields of the magnitude adopted in this study have no measurable effect on the electron density profile but decrease the temperature in the topside ionosphere, as shown in Figure (5.9). A downward heat flux of 10^9 eV cm^{-2} s^{-1} has been assumed in solving the energy equation; different assumptions for this boundary condition could alter the temperature profile. In this section it is intended to demonstrate the effects of a parallel electric field on the characteristics of the ionosphere.

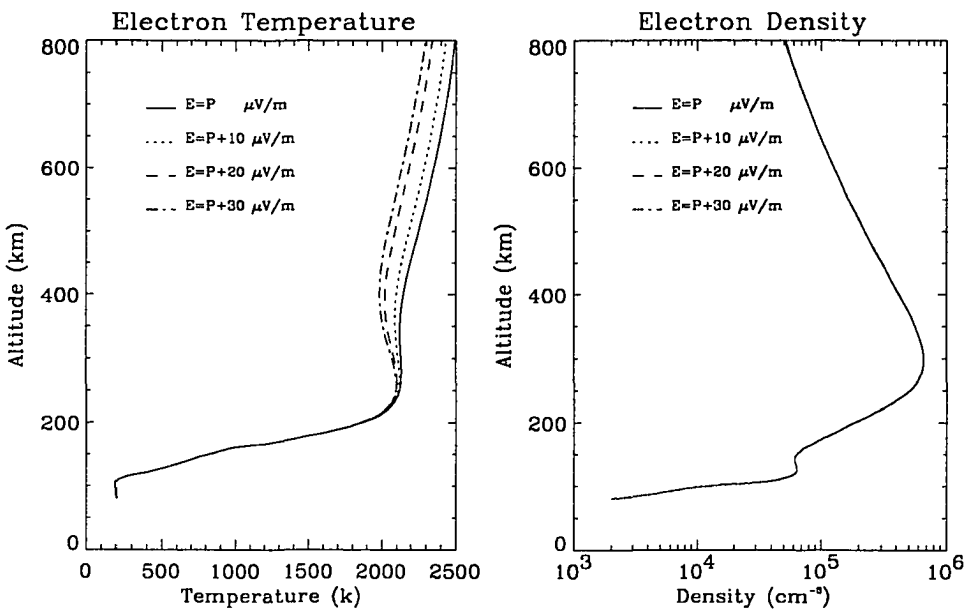

Figure 5.9 Altitude profiles of electron density and temperature for the different magnitudes of electric field: polarization field only (solid lines); polarization field and 10 μV/m (dotted lines); polarization field and 20 μV/m (dashed lines); polarization field and 30 μV/m (chain-dotted lines).

5.2 Ionospheric Conductivities

The conductivity of the ionosphere plays a critical role in magnetosphere-ionosphere coupling, where field-aligned currents feed the ionospheric system of electric fields and currents. Conductivity also links the thermospheric wind system to ionospheric electric fields. Several large-scale models require ionospheric conductivities as input, e.g. the global thermospheric neutral response to ion drag and Joule heating [*Fuller-Rowell et al.*, 1983; *Roble and Ridley*, 1987]; studies of the dynamics of magnetosphere-ionosphere coupling [*Lysak and Dum*, 1983]; the inversion of magnetometer data to obtain ionospheric electric fields [*Kamide et al.*, 1981] and ionospheric convection models [*Rasmussen and Schunk*, 1987].

The ionospheric Hall, Pederson and parallel conductivities usually are derived from height profiles of the electron density using well known formulae that contain the collision and gyrofrequencies [*Vickrey et al.*, 1981; *Brekke et al.*, 1988]. The electron density may be measured from the ground (ionsondes, incoherent backscatter radars) or *in situ* by means of rocket experiments. A less direct way to derive the electron density is to assume local equilibrium between ionization and recombination [*Rasmussen et al.*, 1988] and to calculate the ionization rate from observations of particle precipitation [e.g. *Rees*, 1963].

Unlike most other models that use parameterizations, the time varying auroral model self-consistently solves the electron transport equation, ion continuity equations, and ion and electron energy equations, yielding the electron density and temperature which allows study of the ionospheric conductivity resulting from auroral precipitation.

5.2.1 Profiles of Ionospheric Conductivities

Formulae for the height dependent ionospheric Hall, Pederson and parallel conductivities can be found in standard textbooks on ionospheric physics [see for example *Rees*, 1989, p. 203]. The collision frequencies in the formulae are adopted from *Banks* [1973]. With two parameters which can be inferred from auroral images, the total energy flux and the characteristic energy of auroral electron precipitation, the ionospheric conductances can be derived [*Lummerzheim et al.*, 1991]. *Robinson et al.* [1987] has shown that conductances derived by assuming Maxwellian energy distributions for the auroral electron flux yield good estimates of experimentally derived values. Electron transport calculations have been carried out with synthetic electron spectra of Maxwellian distribution plus a power law (ϵ^{-2}) at lower energies as input at the upper boundary to represent precipitating auroral electrons, consistent with many observation and theoretical results [*Opal et al.*, 1971; *Evans*, 1974; *Pulliam et al.*, 1981]. The altitude distribution of the Pederson and Hall conductivities depends on solar activity [*Brekke et al.*, 1988]. In the present calculation an $F_{10.7}$ solar activity index of 150 and an Ap index of 30 are assumed. The MSIS-90 neutral atmosphere [*Hedin*, 1991] at 60° N, 200° E for northern winter is adopted.

Precipitating energetic electrons ionize the neutral atmosphere and heat ambient electrons and ions. By running the time varying model with the same input parameters as adopted in Chapter 4, the dependence of the conductivities on energy flux and characteristic energy is investigated. The response of the ionosphere to auroral precipitation is shown in Figure (5.10). The hard auroral precipitation penetrates deeper into the atmosphere enhancing the electron density while the soft electron flux is more efficient in raising the electron temperature at higher altitudes.

The Hall and Pederson conductivities associated with the electron density and temperature profiles illustrated in Figure (5.10) are computed and shown in Figure (5.11). While the Hall conductivity is negligible small above 300 km, a minor contribution of Pederson conductivity to

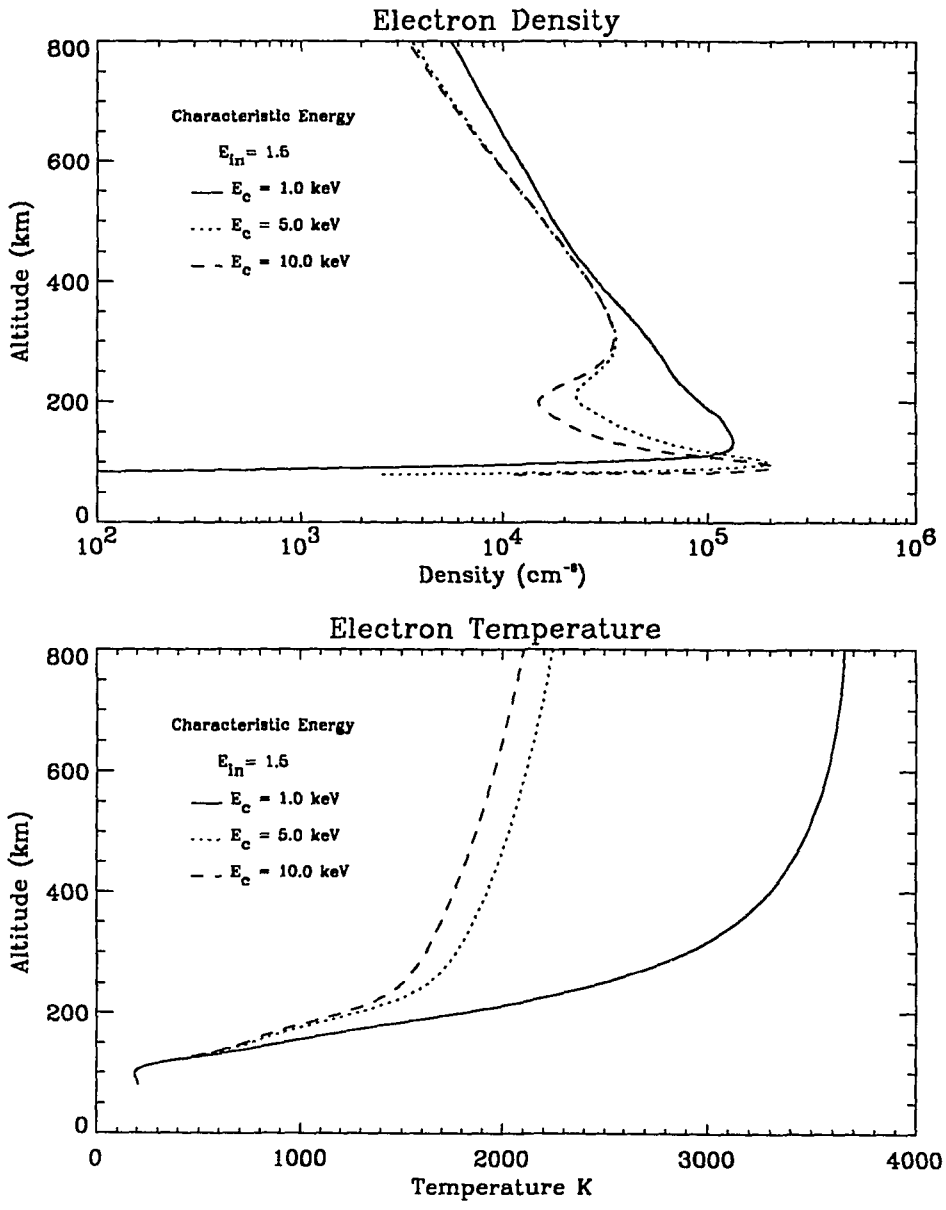

Figure 5.10 The electron density profiles (top) and the electron temperature profiles (bottom) for three different characteristic energies and the same incident energy flux of 1.5 erg cm^{-2} s^{-1}.

the Pederson conductance is observed up to 500 km. Details of the height profiles of the Hall and Pederson conductivities depend on the characteristic energy of the auroral precipitation. At high ionospheric levels where electron-ion collisions become important, the temperature dependence of the electron-ion collision frequency enhances the parallel conductivity of the 1 keV case, shown in Figure (5.11).

5.2.2 Hall and Pederson Conductances

The dependence of conductance on the characteristic energy and the incident energy flux of auroral precipitation has been examined. By integrating the Hall and Pederson conductivities, the Hall and Pederson conductances, shown in Figure (5.12), are computed for an incident energy flux from 0.5 to 27.5 erg cm^{-2} s^{-1} and a characteristic energy from 0.5 to 10 keV.

The conductances are normalized with respect to the power of the incident energy flux, ϵ_{in}^{α} (where the incident energy flux ϵ_{in} is given in units of erg cm^{-2} s^{-1}). The exponent α, shown in Figure (5.13), varies with characteristic energies and the average is 0.55 for both Hall and Pederson conductances rather than 0.5 for most equilibrium calculation [*Vickrey et al.*, 1981; *Robinson et al.*, 1987]. Figure (5.14) displays the normalized (to 1 erg cm^{-2} s^{-1}) Hall and Pederson conductances versus characteristic energy. As expected, soft electron fluxes produce ionization at higher altitudes, and therefore the Pederson conductance is larger than the Hall conductance. As the characteristic energy of the electron precipitation increases, energetic electrons reach to lower altitudes in the atmosphere leading to a larger Hall conductance.

The relationship between the Hall and Pederson conductance ratio and the characteristic energy of precipitating electrons has been studied. The results for two different magnitudes of incident energy flux are displayed in Figure (5.15). The Hall and Pederson conductances are dependent not only on the characteristic energy but also on the incident energy flux. Figure (5.15)

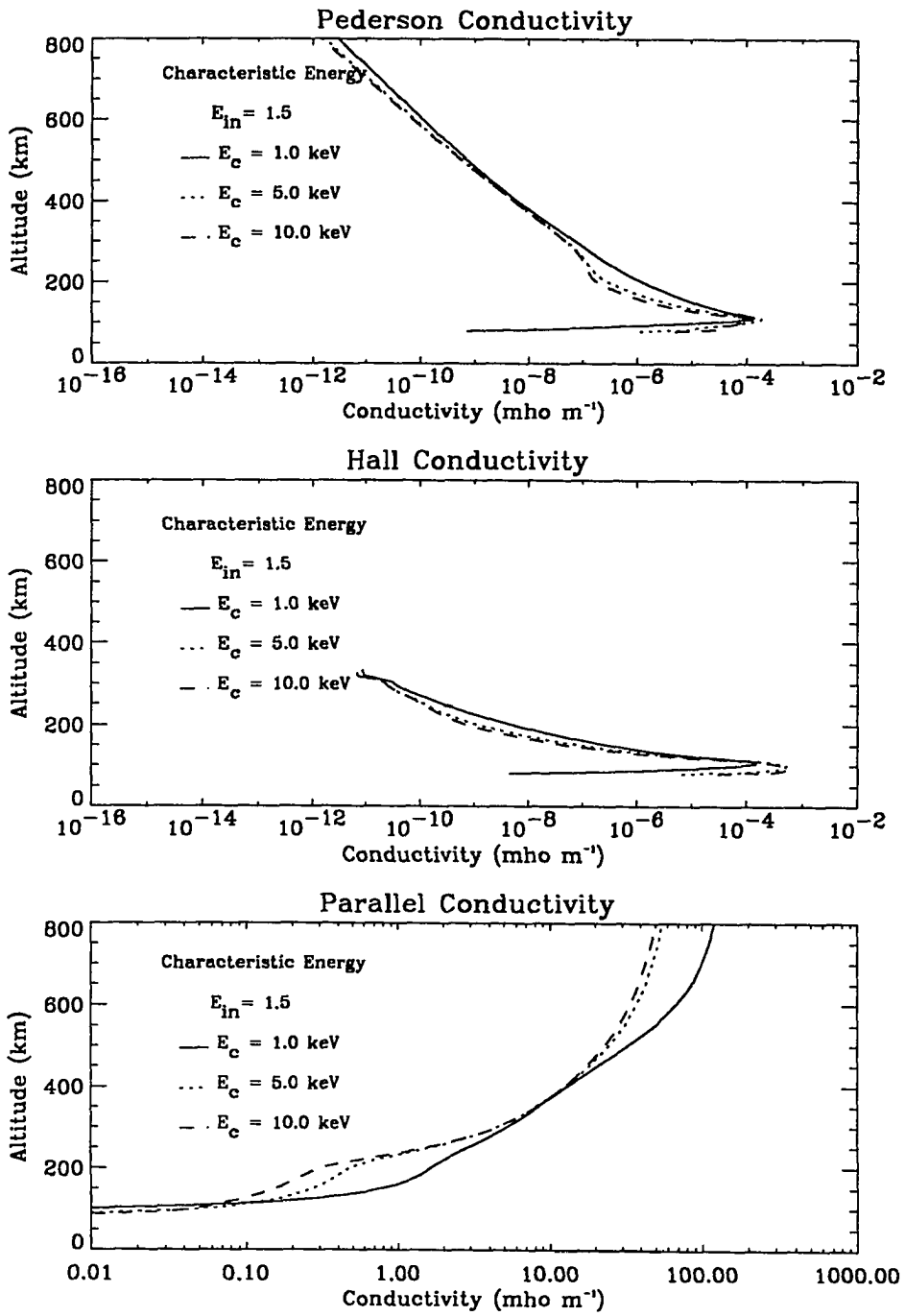

Figure 5.11 The Pederson conductivity profiles (top), the Hall conductivity (middle) and the parallel conductivity (bottom) for the auroral inputs shown in Figure (5.10).

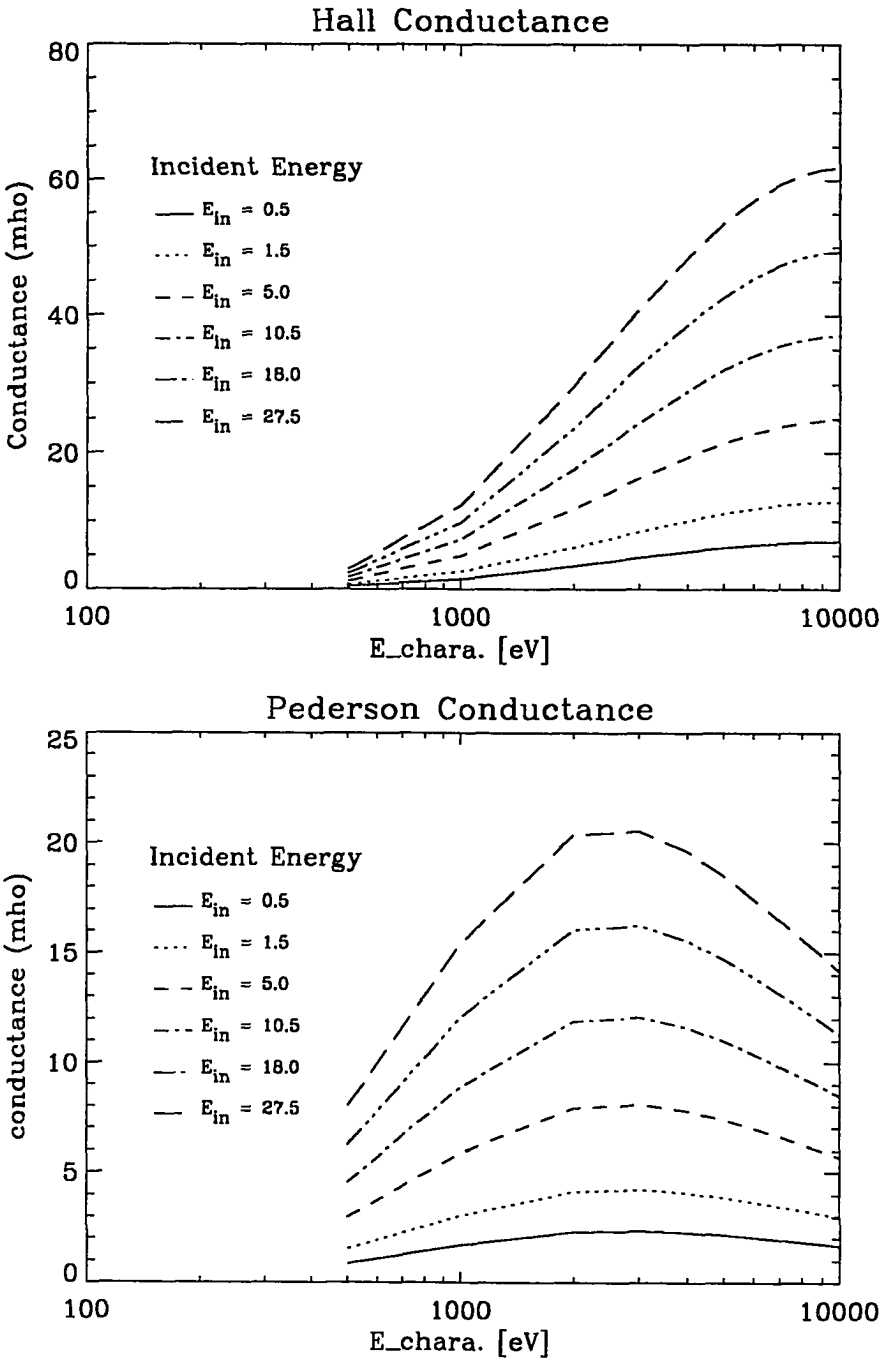

Figure 5.12 The Hall conductance (top) and the Pederson conductance (bottom) versus the characteristic energy of precipitating electrons for different incident energies (erg cm^{-2} s^{-1}).

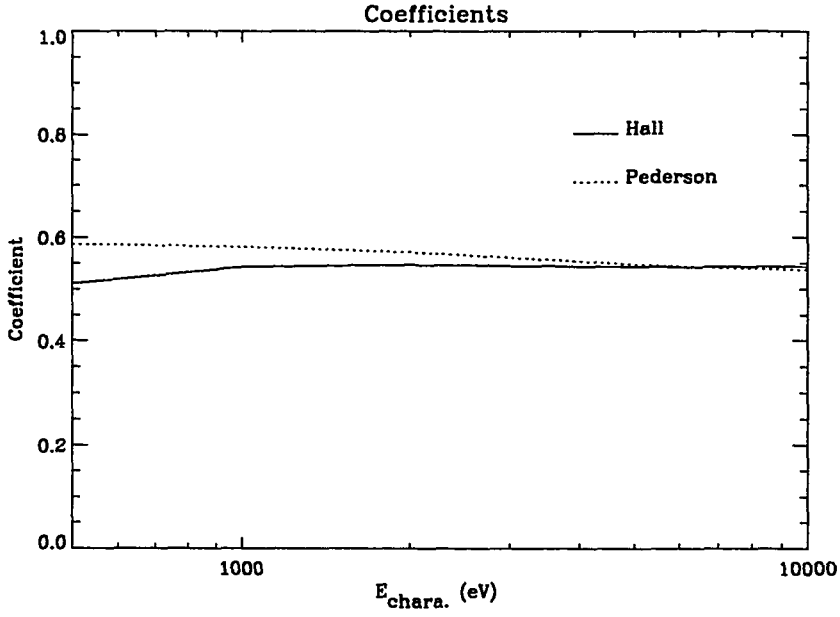

Figure 5.13 Normalization coefficient versus the characteristic energy of precipitating electrons.

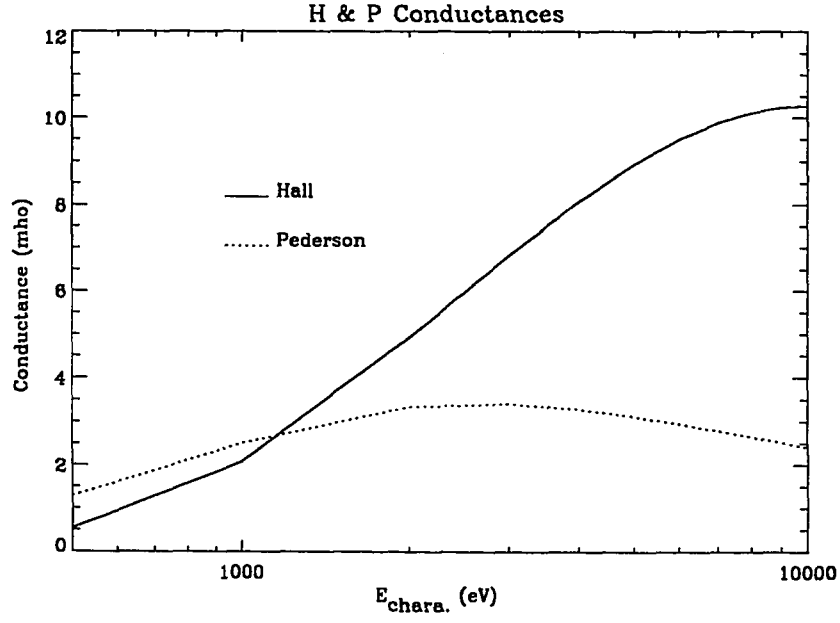

Figure 5.14 Normalized Hall and Pederson conductances versus the characteristic energy of precipitating electrons.

also shows a comparison between the results obtained in this work and the theoretical results of *Rasmussen et al.* [1988] and the empirical models of *Wallis and Budzinski* [1981] and *Robinson et al.* [1987].

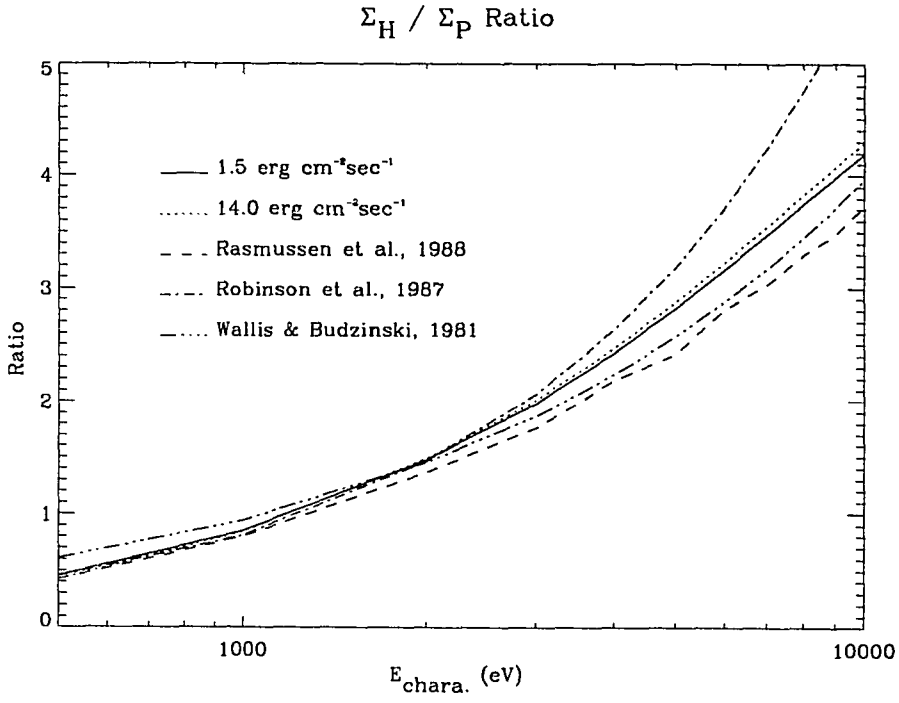

Figure 5.15 The Hall/Pederson conductance ratio as a function of characteristic energy of a Maxwellian spectrum of auroral electron precipitation. Results are shown for two energy fluxes using the present model calculations and comparison is made with the results of other investigators.

CHAPTER 6

Summary and Conclusions

Three systems — the solar wind, the magnetosphere, and the ionosphere — interact, transmitting and transforming the solar-wind energy into a variety of auroral phenomena, and eventually depositing most of it in the ionosphere. A number of major processes act simultaneously within the natural aurora: particle precipitation, perpendicular and parallel electric fields, enhanced thermospheric winds, ionized and neutral particle heating, and ion flow to or from the magnetosphere. Aurorally associated charged particle precipitation into the Earth's atmosphere produces substantial enhancements or perturbations in several ionospheric and atmospheric parameters such as ionization, excitation and thermal effects. In turn, aurorally produced changes in atmospheric/ionospheric parameters cause perturbations to the distribution of the precipitating particles. Due to the complexity of auroral activity, it is difficult to develop a complete three-dimensional model to address every aspect of the coupled system. In order to acquire a better understanding of the physical processes that operate, it is advantageous to examine the effects of each auroral input separately. The objective of this thesis is the development of a one-dimensional self-consistent time varying auroral model for understanding the auroral phenomena in terms of ionospheric properties.

In the atmosphere and ionosphere elastic and inelastic collisions dominate the processes that govern the phase space distribution of energetic particles as well as the ion composition and density and the plasma temperature. Therefore, the coupled electron transport, ion continuity, and electron and ion energy equations are solved self-consistently. Amongst the underlying physical processes in the coupled system, the polarization electric field has a major role in self-consistency, and represents the baseline value of parallel electric field in the topside ionosphere. Numerical

results show that the principal contribution to the polarization field is from the gradient of the electron density, that the field is in the upward direction above about 250 km, and is enhanced during auroral bombardment. Basically, there are two components to the electric field, a polarization field and a field due to current flowing in a region of finite conductivity. The upward directed parallel electric field generated by the properties of the ambient electron gas and the field aligned currents, in turn, accelerates the downward moving electrons and decelerates the upward moving component, as well as acting on the thermal electrons and ions. However, Poisson's equation which couples the electric field with the charge density is not included. Therefore, a self-consistent electric field due to a current of magnetospheric origin can not be adopted. For the purpose of this study, it is assumed that an arbitrary, but reasonable value electric field is maintained by the field aligned auroral currents in the vicinity of an auroral arc, such that the electric field term is always a minor acceleration source in the transport equation and has no direct influence on the ion and electron continuity and energy equations. The precipitating electrons are affected by this field. These electrons constitute the major heat source for the ambient thermal electrons and it is to be expected that a parallel electric field will thus influence the electron temperature. Joule heating from parallel electric fields of the magnitude adopted here is much smaller and the direct effect of such fields on the thermal electron population is neglected.

In this thesis an electric field acceleration term and a converging magnetic field term are introduced into the collisional electron transport equation, which is derived from the Boltzmann equation. The new electron transport code, which computes the evolution of the electron intensity as a function of altitude, energy, and pitch angle as the stream penetrates into the inhomogeneous atmosphere, is developed and discussed in Chapter 2. The feedback effects generated by the properties of the ambient electron gas and the polarization field are investigated. The numerical calculations have been carried out for an auroral event representing an external flux source and for a solar case representing an embedded source of photoelectrons. Reasonable agreement is found

between results of the present transport calculation and results of previously published transport calculations. It is noted that field effects are important when electrons experience a significant change in energy and/or momentum in a mean free path between collisions. Computations indicate that electric fields are most effective in perturbing the low energy($\epsilon < 50$ eV) component of the electron distribution function. Electric and magnetic fields of the magnitude investigated in this work perturb the distribution functions at altitudes above about 250 km but not below. The upward directed polarization electric field (above 250 km) and the field due to field aligned currents accelerate the downward electron flux and decelerate the upward component, thus leading to a steepening of the downward energy distribution as well as a flattening of the upward component. The inhomogeneous magnetic field produces anisotropies in the angular distribution of the electron intensity that result in perturbations of the high energy component of the electron distribution function. Even modest values of field aligned electric fields perturb the electron temperature in the topside ionosphere. The electron temperature can increase or decrease, depending on the magnitude of the low energy omnidirectional electron flux. Excited states of atoms and molecules with electron impact cross section that maximize at low energies are expected to be enhanced by the presence of parallel electric fields.

A new ionchemistry model is developed and the coupled time-dependent diffusion equations are derived in Chapter 2. The distribution of the two major ions, O^+ and H^+, is governed by ambipolar diffusion along the magnetic field, while the minor ions are asummed to be in photochemical equilibrium with the major ions. The dynamics and compositions of the thermosphere are influenced by the temperature structure and by the temperature dependence of the transport coefficients. The energy equations for electrons and ions are therefore coupled with the continuity equations. The coupled electron and ion energy equations are derived, in which major heat sources and sinks are included: energetic electrons, perpendicular electric fields, heat flow from the magnetosphere, Coulomb collisions and elastic and inelastic collisions. The computational

problem is simplified by using physical arguments based on different time scales and altitudes. The diurnal variation of the ionosphere during non-auroral conditions is presented and the response of the ionosphere to auroral precipitation is computed. The dynamical response of the ionosphere and atmosphere to auroral precipitations is dependent upon the characteristic energy, flux magnitude and time history of the precipitation. A soft auroral spectrum affects primarily the ionospheric F-region producing changes in electron and ion densities and temperatures. As the particle spectrum hardens, the ionospheric effects occur at lower altitude. It is shown that the ionospheric and atmospheric response is greater for night-time aurora than daytime aurora because during the day the aurora is superimposed upon a larger background electron density, maintained by solar EUV radiation. As discussed earlier, a three-dimensional model is needed for a self-consistent analysis of the dynamics and compositions of the major neutral gas constituents. To improve the present model and to better explain the observations, there are a number of extension of this work that can be carried out, based on the general framework of this model: adding a vertical wind into the ambipolar diffusion term and including the diffusion of the minor neutral constituents $N(^2D)$, $N(^2S)$ and NO. It is also possible to study the auroral emissions which are generated when excited atoms and molecules due to the incident energetic electrons decay to lower states. Emission rates also depend on chemical reactions and on radiative de-excitation.

A theoretical conductivity model, based on the time varying auroral model, is developed. The properties of Hall and Pederson conductances are discussed as a function of characteristic energy and energy flux. Good agreement with existing theoretical and empirical results is found. It is noted that as the Hall and Pederson conductances depend on the characteristic energy as well as the energy flux, the Hall to Pederson conductance ratio is also a function of both parameters. To complete the study of ionospheric conductivity, the Hall and Pederson conductivity of the quiet time auroral ionosphere can be investigated with the present model as a function of the $F_{10.7}$ solar flux and the solar zenith angle.

In summary, the present study of the self-consistent time varying auroral model provides a theoretical explanation for the response of the ionosphere to auroral precipitation. The parallel electric field affects the energy distributions of auroral electrons and photoelectrons as well as the temperature of the ambient electron gas.

APPENDIX A

Details of the Derivation of the Quartic Equation

It is assumed that in the ionosphere O^+ and H^+ are the dominant diffusing ions and N^+, O_2^+, N_2^+ and NO^+ are the minor ions which are in photochemical equilibrium with the O^+ and H^+ distributions. From the chemistry specified in Table (2.1), the production and loss terms of O_2^+, N_2^+ and NO^+ are equated.

Production and loss terms of N_2^+ are

$$P_{N_2^+} = D$$

$$L_{N_2^+} = (E + \alpha_2 n_e) n(N_2^+)$$

Therefore then

$$n(N_2^+) = \frac{D}{E + \alpha_2 n_e} \qquad (A.1)$$

where

$$D = \gamma_3 n(O^+(^2D)) n(N_2) + \gamma_6 n(O_2^+(a^4\Pi)) n(N_2) + \gamma_9 n(O^+(^2P)) n(N_2) + \eta_d^{N_2^+}$$

$$E = \gamma_4 n(O) + \gamma_5 n(O_2) + \gamma_{18} n(NO) + \gamma_{19} n(O)$$

Production and loss terms of O_2^+ are

$$P_{O_2^+} = H n(N_2^+) + B$$

$$L_{O_2^+} = (C + \alpha_1 n_e) n(O_2^+)$$

Therefore

$$n(O_2^+) = \frac{H n(N_2^+) + B}{(C + \alpha_1 n_e)} \qquad (A.2)$$

where

$$B = \gamma_2 n(O^+(^4S))n(O_2) + \gamma_7 n(O_2^+(a^4\Pi))n(O) + \gamma_{11} n(N^+)n(O_2)$$
$$+ \gamma_{22} n(O^+(^2D))n(O_2) + \gamma_{33} n(N^+)n(O_2) + A_8 n(O_2^+(a^4\Pi)) + \eta_d^{O_2^+}$$

$$C = \gamma_8 n(N_2) + \gamma_{15} n(NO) + \gamma_16 n(N(^4S)) + \gamma_{17} n(N(^2D))$$

$$H = \gamma_5 n(O_2)$$

Production and loss terms of NO^+ are

$$P_{NO^+} = A + Fn(O_2^+) + Gn(N_2^+)$$

$$L_{NO^+} = \alpha_3 n_e n(NO^+)$$

Therefore

$$n(NO^+) = \frac{A + Fn(O_2^+) + Gn(N_2^+)}{\alpha_3 n_e} \qquad (A.3)$$

where

$$A = \gamma_1 n(O^+(^4S))n(N_2) + \gamma_{10} n(N^+)n(O_2) + \gamma_{21} n(O^+(^4S))n(NO) + \eta_d^{NO^+}$$

$$F = \gamma_8 n(N_2) + \gamma_{15} n(NO) + \gamma_{16} n(N)$$

$$G = \gamma_4 n(O) + \gamma_{18} n(NO)$$

In the altitude region of interest negative ions are unimportant, reducing the charge neutrality

condition to the electron density being equal to the sum of all positive ion densities

$$n_e = n(O^+) + n(H^+) + n(N^+) + n(N_2^+) + n(O_2^+) + n(NO^+) \qquad (A.4)$$

Substituting the equations (A.1), (A.2), and (A.3) into (A.4) and setting

$$K = n(O^+) + n(H^+) + n(N^+)$$

it yields

$$K + \frac{D}{E+\alpha_2 n_e} + \frac{H\frac{D}{E+\alpha_2 n_e} + B}{(C+\alpha_1 n_e)} + \frac{A + F\frac{H\frac{D}{E+\alpha_2 n_e}+B}{(C+\alpha_1 n_e)} + G\frac{D}{E+\alpha_2 n_e}}{\alpha_3 n_e} = n_e \qquad (A.5)$$

Ordering the terms in powers of n_e gives:

$$\begin{aligned}
&n_e^4[\alpha_1\alpha_2\alpha_3]+ \\
&n_e^3[\alpha_3(\alpha_2 C + \alpha_1 E - \alpha_1\alpha_2 K)]+ \\
&n_e^2[\alpha_3(EC - \alpha_1 KE - \alpha_2 KC - \alpha_1 D - \alpha_2 B) - \alpha_1\alpha_2 A]+ \qquad (A.6)\\
&n_e[-\alpha_3(KEC + DC + HD + BE) - \alpha_1(AE + GD) - \alpha_2(AC + FB)] \\
&=[ACE + DHF + BEF + CDG]
\end{aligned}$$

With the definitions

$$\begin{aligned}
a_0 &= -ACE - DHF - BEF - CDG \\
a_1 &= -\alpha_3(KEC + DC + HD + BE) - \alpha_1(AE + GD) - \alpha_2(AC + FB) \\
a_2 &= \alpha_3(EC - \alpha_1 KE - \alpha_2 KC - \alpha_1 D - \alpha_2 B) - \alpha_1\alpha_2 A \\
a_3 &= \alpha_3(\alpha_2 C + \alpha_1 E - \alpha_1\alpha_2 K) \\
a_4 &= \alpha_1\alpha_2\alpha_3
\end{aligned}$$

equation (2.28) is obtained

$$a_4 n_e^4 + a_3 n_e^3 + a_2 n_e^2 + a_1 n_e + a_0 = 0 \qquad (A.7)$$

REFERENCES

Albert, R. D., and P. J. Lindstrom, Auroral particle precipitation and trapping caused by electrostatic double layers in the ionosphere, *Science, 170*, 1390, 1970.

Alfvén, H., On the theory of magnetic storms and aurorae, *Tellus, 10*, 104, 1958.

Alfvén, H., and C.-G. Fälthammer, Cosmical electrodynamics, *Second edition*, Oxford University Press, 1963.

Banks, P. M., G. Kockarts, Aeronomy, Academic Press, New York, 1973.

Banks, P. M., and A. F. Nagy, Concerning the influence of elastic scattering upon photoelectron transport and escape, *J. Geophys. Res., 75*, 1902, 1970.

Banks, P. M., C. R. Chappell, and A. F. Nagy, A new model for the interaction of auroral electrons with the atmosphere: spectral degradation, backscatter, optical emission, and ionization, *J. Geophys. Res., 79*, 1459, 1974.

Berger, M. J., S. M. Seltzer, and K. Maeda, Energy deposition by auroral electrons in the atmosphere, *J. Atmos. Terr. Phys., 32*, 1015, 1970.

Bingham, R., D. A. Bryant, and D. S. Hall, A wave model for the aurora, *Geophys. Res. Lett., 11*, 327, 1984.

Block, L. P., Potential double layers in the ionosphere, *Cosmic Electrodyn., 3*, 349, 1972.

Boehm, C. W., C. W. Carlson, J. P. McFadden, and F. S. Mozer, Dual sounding rocket observations of low-altitude electrostatic shocks, *J. Geophys. Res., 95*, 12173, 1990.

Brekke, A., C. Hall, and T. L. Hansen, Auroral ionospheric conductances during disturbed conditions, *Ann. Geophys., 7*, 269, 1988.

Bryant, D. A., The hot electrons in and above the auroral ionosphere; observations and physical implications, *High Latitude Space Plasma Physics*, edited by B. Hultqvist and T. Hagfors, p. 295, Plenum Press, New York and London, 1983.

Bryant, D. A., Auroral electron acceleration, *Phys. Scr., 30*, 215, 1990.

Burgers, J. M., Flow equations for composite gases, Academic Press, New York, 1969.

Burnett, T., and S. P. Rountree, Differential and total cross sections for electron-impact ionization of atomic oxygen, *Phys. Rev., A, 20*, 1468, 1979.

Cannon, C. J., Nonlocal perturbation techniques in radiative transfer, *Methods in Radiative Transfer Problems*, edited by Kalkofen, W., p. 155, Cambridge University Press, New York, 1984.

Chandrasekhar, S., Radiative transfer, Dover Publications, New York, 1960.

Christensen, A. B., L. R. Lyons, J. H. Hecht, G. G. Sivjee, R. R. Meier, and D. G. Strickland, Magnetic field-aligned electric field acceleration and the characteristics of the optical aurora, *J. Geophys. Res., 92*, 6163, 1987.

Chiu, Y. T., and M. Schulz, Self consistent particle and parallel electrostatic field distributions in the magnetospheric-ionospheric auroral region, *J. Geophys. Res., 83*, 629, 1978.

Chiu, Y. T., and J. M. Cornwall, Electrostatic model of a quiet auroral arc, *J. Geophys. Res., 85*, 543, 1980.

Chiu, Y. T., J. M. Cornwall, J. F. Fennell, D. J. Gorney, and P. F. Mizera, Auroral plasmas in the evening sector: satellite observations and theoretical interpretations, *Space Sci. Rev., 35*, 211, 1983.

Dickinson, R. E., E. C. Ridley, and R. G. Roble, A three-dimensional, time-dependent general circulation model of the thermosphere, *J. Geophys. Res., 86*, 1499, 1981.

Duderstadt, J. J., and W. R. Martin, Transport theory, Wiley, New York, 1979.

Evans, D. S., Precipitating electron fluxes formed by a magnetic field aligned potential difference, *J. Geophys. Res., 79*, 2853, 1974.

Evans, D. S., N. C. Maynard, J. Troim, T. Jacobson, and A. Egeland, Auroral particles and fields, *J. Geophys. Res. 82*, 2235, 1977.

Frank, L. A., and K. L. Ackerson, Observations of charged particle precipitation into the auroral zone, *J. Geophys. Res. 76*, 3612, 1971.

Fuller-Rowell, T. J., and D. Rees, A three-dimensional, time-dependent global model of the thermosphere, *J. Atmos. Sci., 37*, 2545, 1980.

Fuller-Rowell, T. J., and D. S. Evans, Height-integrated Pederson- and Hall-conductivity patterns inferred from the TIROS-NOAA satellite data, *J. Geophys. Res., 92*, 7606, 1987.

Fuller-Rowell, T. J., D. Rees, S. Quegan, G. J. Nailey, and R. J. Moffett, The effect of the realistic conductivities on the high-latitude neutral circulation, *Planet. Space Sci., 43*, 469, 1983.

Fuller-Rowell, T. J., S. Quegan, D. Rees, R. J. Moffett, and G. J. Bailey, Interactions between neutral thermospheric composition and the polar ionosphere using a coupled global model, *J. Geophys. Res., 92*, 7744, 1987.

Fung, S. F., and R. A. Hoffman, A search for parallel electric fields by observing secondary and photoelectrons in the low altitude auroral zone, *J. Geophys. Res. 96*, 3533, 1991.

Gerard, J.-C., and C. A. Barth, High latitude nitric oxide in the lower thermosphere, *J. Geophys. Res., 82*, 674, 1977.

Goertz, C. K., and R. W. Boswell, Magnetosphere-ionosphere coupling, *J. Geophys. Res., 84*, 7239, 1979.

Gurgiolo, C., and J. L. Burch, Simulation of electron distributions within auroral acceleration regions, *J. Geophys. Res., 93*, 3989, 1988.

Hardy, D. A., M. S. Gussenhoven, and R. Raistrick, Statistical and functional representations of the pattern of auroral energy flux, number flux and conductivity, *J. Geophys. Res., 92*, 12275, 1987.

Hays, P. B., R. A. Jones, and M. H. Rees, Auroral heating and the composition of the neutral atmosphere, *Planet. Space Sci., 21*, 559, 1973.

Hedin, A. E, Extension of the MSIS thermosphere model into the middle and lower atmosphere, *J. Geophys. Res., 96*, 1159, 1991.

Hinteregger, H. E., Representations of solar EUV fluxes for aeronomical applications, *Adv. Space Res., 1*, 39, 1981.

Hoffman, R. A., and D. S. Evans., Field-aligned electron bursts at high latitude observed by OGO-4, *J. Geophys. Res., 73*, 6201, 1968.

Hultqvist, B., On the production of a magnetic field-aligned electric field by the interaction between the hot magnetospheric plasma and the cold ionosphere, *Planet. Space Sci., 19*, 749, 1971.

Hyman, E., D. J. Strickland, P. S. Julienne, and D. F. Strobel, Auroral NO concentrations? *J. Geophys. Res., 81*, 4765, 1976.

Johnson, C. Y., Ion and neutral composition of the ionosphere, in *Annals of the IQSY, 5*, M.I.T. Press, 197, 1969.

Jones, R. A., and M. H. Rees, Time dependent studies of the auroral—I. Ion density and composition, *Planet. Space Sci., 21*, 537, 1973.

Kamide, Y., A. D. Richmond, and S. Matsushita, Estimation of ionospheric electric fields, ionospheric currents, and field-aligned currents from ground magnetic records, *J. Geophys. Res., 86*, 801, 1981.

Kan, J. R., Towards a unified theory of discrete auroras, *Space Sci. Rev., 31*, 71, 1982.

Kaufmann, R. L., D. N. Walker, and R. L. Arnoldy, Acceleration of auroral electrons in parallel electric fields, *J. Geophys. Res., 81*, 1673, 1976.

Killeen, T. L., F. G. McCormac, A. G. Burns, and R. G. Roble, Thermospheric dynamics, energetics, and composition at auroral latitudes, *Auroral Physics*, Cambridge, 1991.

Knight, S., Parallel electric fields, *Planet. Space Sci., 21*, 741, 1973.

Lanchester, B. S., and D. D. Wallis, Magnetic field disturbances over auroral arcs observed from Spitsbergen, *J. Geophys. Res., 90*, 2473, 1985.

Lanchester, B. S., and M. H. Rees, Field-aligned current reversals and fine structure in a dayside auroral arc, *Planet. Space Sci., 35*, 759, 1987.

Lennartsson, W., On the magnetic mirroring as the basic cause of parallel electric fields, *J. Geophys. Res., 81*, 5583, 1976.

Lilensten, J., Résolution de l'equation de transport de Boltzman et applications dans le plasma ionosphérique, these de doctorat, Inst. Natl. Polytech. de Grenoble, Grenoble, France, 1989.

Link, R., Feautrier solution of the electron transport equation, *J. Geophys. Res., 97*, 159, 1992.

Lummerzheim, D., Electron transport and optical emissions in the aurora, Ph.D. Thesis, University of Alaska, Fairbanks, 1987.

Lummerzheim, D., M. H. Rees, and H. R. Anderson, Angular dependent transport of auroral electrons in the upper atmosphere, *Planet. Space Sci., 37*, 109, 1989.

Lummerzheim, D., M. H. Rees, J. D. Craven, and L. A. Frank, Ionospheric conductances derived from DE-1 auroral images, *J. Atmos. Terr. Phys., 53*, 109, 1991.

Lundin, R., and L. Eliasson, Auroral energization processes, *Ann. Geophys.*, *9*, 202, 1991.

Lysak, R. L., and C. T. Dum, Dynamics of magnetosphere-ionosphere coupling including turbulent transport, *J. Geophys. Res.*, *88*, 365, 1983.

Mantas, G. P., Theory of photoelectron thermalization and transport in the ionosphere, *Plant. Space Sci.*, *23*, 337, 1975.

McFadden, J. P., C. W. Carlson, and M. H. Boehm, Structure of an energetic narrow discrete arc, *J. Geophys. Res.*, *95*, 6533, 1990.

McIlwain, C. E., Direct measurement of particles producing visible aurora, *J. Geophys. Res.*, *65*, 2727, 1960.

Meier, R. R., R. R. Conway, D. E. Anderson Jr., P. D. Feldman, R. W. Eastes, E. P. Gentieu, and A. B. Christensen, The ultraviolet dayglow at solar maximum, 3, Photoelectron-excited emissions of N_2 and O, *J. Geophys. Res.*, *90*, 6608, 1985.

Meira, L. G., Rocket measurements of upper atmospheric nitric oxide and their consequences to the lower ionosphere, *J. Geophys. Res.*, *76*, 202, 1971.

Menietti, J. D., and J. L. Burch, "Electron conic" signatures observed in the nightside auroral zone and over the polar cap, *J. Geophys. Res.*, *90*, 5345, 1985.

Mozer, F. S., On the lowest altitude S3-3 observations of electrostatic shocks and parallel electric fields, *Geophys. Res. Lett.*, *7*, 1097, 1980.

Mozer, F. S., The low altitude electric field structure of discrete auroral arcs, *Physics of Auroral Arc Formation, Geophys. Monogr. Ser.*, *25*, edited by S.-I. Akasofu and J. R. Kan, p. 136, AGU Washington, D. C., 1981.

Mozer, F. S., C. W. Carlson, M. K. Hudson, R. B. Torbert, B. Parady, J. Yatteau, and M. C. Kelly. Observations of paired electrostatic shocks in the polar magnetosphere, *Phys. Rev. Lett.*, *38*, 292, 1970.

Nagy, A. F., and P. M. Banks, Photoelectron fluxes in the ionosphere, *J. Geophys. Res.* *75*, 6260, 1970

Opal, C. B., W. K. Peterson, and E. C. Beaty, Measurements of secondary-electron spectra produced by electron impact ionization of a number of simple gases, *J. Chem Phys.*, *55*, 4100, 1971.

Oran, E. S., and D. J. Strickland, Photoelectron flux in the Earth's ionosphere, *Planet. Space Sci., 26,* 1161, 1978.

Otto, A., and G. Birk, The dynamical evolution of small-scale auroral arc phenomena due to a resistive instability, *J. Geophys. Res., 97,* 6500, 1992.

Papadopoulos, K., A review of anomalous resistivity for the ionosphere, *Rev. Geophys. Space Phys., 15,* 113, 1977.

Porter, H. S., F. Varosi, and H. G. Mayr, Iterative solution of the multistream transport equation 1. comparison with laboratory beam injection experiments, *J. Geophys. Res., 92,* 5933, 1987.

Press, W. H., B. P. Flannery, S. A. Teukosky, and W. T. Vetterling, Numerical recipes, Cambridge, 1989.

Pulliam, D. M., H. R. Anderson, K. Stamnes, and M. H. Rees, Aurora electron acceleration and atmospheric interactions, *J. Geophys. Res., 86,* 2397, 1981.

Rasmussen, C. E., and R. W. Schunk, Ionospheric convection driven by NBZ currents, *J. Geophys. Res., 92,* 4491, 1987.

Rasmussen, C. E., R. W. Schunk, and V. B. Wickwar, A Photochemical equilibrium model for ionospheric conductivity, *J. Geophys. Res., 93,* 9831, 1988.

Rees, D., and T. J. Fuller-Rowell, Thermospheric response and feedback to auroral inputs, *Auroral Physics*, edited by C.-I. Ming, M. J. Rycroft and L. A. Frank, p. 51, Cambridge, 1991.

Rees, M. H., Absolute photometry in the auroral-I the ionized molecular nitrogen emission and the oxygen green line in the dark atmosphere, *J. Atmos. Terr. Phys., 14,* 325, 1958.

Rees, M. H., Auroral ionization and excitation by incident energetic electrons, *Planet. Space Sci., 11,* 1209, 1963.

Rees, M. H., Modeling of the heating and ionizing of the polar thermosphere by magnetospheric electron and ion precipitation, *Physica Scripta, T18,* 249, 1987.

Rees, M. H., Physics and chemistry of the upper atmosphere, Cambridge, 1989.

Rees, M. H., and J. C. G. Walker, Ion and electron heating by auroral electric fields, *Ann. Geophys., 24,* 193, 1968.

Rees, M. H., and R. A. Jones, Time-dependent studies of the aurora—II. Spectroscopic morphology, *Planet. Space Sci., 21*, 1213, 1973.

Rees, M. H., and D. Luckey, Auroral electron energy derived from ratio of spectroscopic emissions 1. Model computations, *J. Geophys. Res., 79*, 5181, 1974.

Rees, M. H., and R. G. Roble, Observations and theory of the formation of stable auroral red arcs, *Rev. Geophys. Space Phys., 13*, 201, 1975.

Rees, M. H., and R. G. Roble, Excitation of $O(^1D)$ atoms in aurorae and emission of the [OI] 6300 line, *Can. J. Phys., 64*, 1608, 1986.

Rees, M. H., and D. Lummerzheim, Auroral excitation processes, *Auroral Physics*, edited by C.-I. Ming, M. J. Rycroft and L. A. Frank, p. 29, Cambridge, 1991.

Rees, M. H., J. C. G. Walker, and A. Dalgarno, Auroral excitation of the forbidden lines of atomic oxygen, *Planet. Space Sci., 15*, 1097, 1967.

Rees, M. H., A. I. Stewart, and J. C. G. Walker, Secondary electron in aurora, *Planet. Space Sci., 17*, 1997, 1969.

Rees, M. H., R. A. Jones, and J. C. G. Walker, The influences of field-aligned currents on auroral electron temperatures, *Planet. Space Sci., 19*, 313, 1971.

Rees, M. H., B. A. Emery, R. G. Roble, and K. Stamnes, Neutral and ion gas heating by auroral electron precipitation, *J. Geophys. Res., 88*, 6289, 1983.

Rees, M. H., D. Lummerzheim, R. G. Roble, J. D. Winningham, J. D. Craven, and L. A. Frank, Auroral energy deposition rate, characteristic electron energy, and ionospheric parameters derived from Dynamics Explorer 1 images, *J. Geophys. Res., 93*, 12841, 1988.

Reiff, P. H., H. L. Collin, J. D. Craven, J. L. Burch, J. D. Winningham, E. G. Shelley, L. A. Frank, and M. A. Friedman, Determination of auroral electrostatic potentials using high- and low-altitude particle distributions, *J. Geophys. Res., 93*, 7441, 1988.

Robinson, R. M., R. R. Vondark, K. Miller, T. Dabbs, and D. Hardy, On calculating ionospheric conductances from the flux and energy of precipitating electrons, *J. Geophys. Res., 92*, 2565, 1987.

Roble, R. G., The calculated and observed diurnal variation of the ionosphere over Millstone Hill on 23-24 March 1970, *Planet. Space Sci., 23*, 1017, 1975.

Roble, R. G., and M. H. Rees, Time-dependent studies of the aurora: effects of particle precipitation on the dynamic morphology of ionospheric and atmospheric properties, *Planet. Space Sci. 25*, 991, 1977

Roble, R. G., and E. C. Ridley, An auroral model for the NCAR thermospheric general circulation model (TGCM), *Ann. Geophys., 5A*, 369, 1987.

Roble, R. G., E. C. Ridley, A. D. Richmond, and R. E. Dickinson, A coupled thermosphere - ionosphere general circulation model, *Geophys. Res. Lett., 15*, 1325, 1988.

Schunk, R., and J. C. G. Walker, Thermal diffusion in the *F*2-region of the ionosphere, *Planet. Space Sci. 18*, 535, 1970a.

Schunk, R., and J. C. G. Walker, Minor ion diffusion in the *F*2-region of the ionosphere, *Planet. Space Sci. 18*, 1319, 1970b.

Schunk, R., and J. C. G. Walker, Transport properties of the ionospheric electron gas, *Planet. Space Sci. 18*, 1535, 1970c.

Schunk, R., and A. F. Nagy, Electron temperatures in the *F* region of the ionosphere: theory and observations, *Rev. Geophys. Space Phys., 16*, 355, 1978.

Smith, F. L., and C. Smith, Numerical evaluation of Chapman's grazing incident integral ch(X, χ), *J. Geophys. Res., 77*, 3592, 1972.

Stamnes, K., A theoretical investigation of the interaction of auroral electrons with the atmosphere, Ph.D. Thesis, University of Colorado, 1978.

Stamnes, K., Analytic Approach to auroral electron transport and energy degradation, *Planet. Space Sci., 28*, 427, 1980.

Stamnes, K., On the two-stream approach to electron transport and thermalization, *J. Geophys. Res., 86*, 2405, 1981.

Stamnes, K., and M. H. Rees, Inelastic scattering effects on photoelectron spectra and ionospheric electron temperature, *J. Geophys. Res., 88*, 6301, 1983.

Stamnes, K., S. Perraut, J. M. Bosqued, M. H. Rees, and R. G. Roble, Ionospheric respose to daytime auroral electron precipitation, *Annales Geophys. 3*, 235, 1986.

Stamnes, K., W. J. Wiscombe, S. C. Tsay, and K. Jayaweera, An improved, numerically stable multiple scattering algorithm for discrete-ordinate-method radiative transfer in scattering and emitting layered media, *Appl. Optics, 27*, 2502, 1988.

Stasiewicz, K., On the origin of the auroral inverted-V electron spectra, *Planet. Space Sci., 32,*, 379, 1984.

Stasiewicz, K., The influence of a turbulent region on the flux of auroral electrons, *Planet. Space Sci., 33*, 591, 1985.

Stasiewicz, K., R. Lundin, and B. Hultqvist, The origin of the power-law component in auroral electron spectra, *Geophys. Res. Lett., 14*, 447, 1987.

Störmer, C., The polar aurora, Oxford Clarendon Press, 1955

Strickland, D. J., and P. C. Kepple, Preliminary report on the transport and production of energetic electrons in auroras, *NRL Memorandum Report*, 2779, 1974.

Strickland, D. J., D. L. Book, T. P. Coffey, and J. A. Fedder, Transport equation techniques for the deposition of auroral electrons, *J. Geophys. Res., 81*, 2755, 1976.

Strickland, D. J., J. R. Jasperse, and J. A. Whalen, Dependence of auroral FUV emissions on the incident electron spectrum and neutral atmosphere, *J. Geophys. Res., 88*, 8051, 1983.

Swartz, W. E., J. S. Nisbet, and A. E. S. Green, Analytic expression for the energy transfer rate from photoelectrons to thermal electrons, *J. Geophys. Res., 76*, 8425, 1971.

Temerin, M., K. Cerny, W. Lotko, and F. S. Mozer, Observations of double layers and solitary waves in auroral plasma, *Phys. Res. Lett., 48*, 1175, 1982.

Temerin, M., J. McFadden, M. Boehm, C. W. Carlson, and W. Lotko, Production of flickering aurora and field-aligned electron flux by electromagnetic ion cyclotron waves, *J. Geophys. Res., 91*, 5769, 1986.

Vallance, Jones A., Aurora, D. Reidel Publishing Co., Dordrecht-Holland, 1974.

Vallance, Jones A., Overview of auroral spectroscopy, *Auroral Physics*, edited by C.-I. Ming, M. J. Rycroft, and L. A. Frank, p. 15, Cambridge, 1991.

Vallance, Jones A., R. L. Gattinger, P. Shih, J. W. Meriwether, V. B. Wickwar, and J. Kelly, Optical and radar characterization of a short-lived auroral event at high latitude, *J. Geophys. Res., 92*, 4575, 1987.

Vickrey, J. F., R. R. Vondrak, and S. J. Matthew, The diurnal and latitudinal variation of auroral zone ionospheric conductivity, *J. Geophys. Res., 86*, 609, 1981.

Volokitin, A. S., V. V. Krasnosel'skikh, E. V. Mishin, L. O. Tyurmina, V. A. Sharova, and S. I. Shkol'nikova, Small-scale structure of intense logitudinal currents at high latitudes (in Russian), *Kosm. Issled., 22*, 749, 1984, (translated by Plenum, New York.).

Walker, J. C. G., and M. H. Rees, Ionospheric electron densities and temperatures in auroral, *Planet. Space Sci., 16*, 459, 1968.

Wallis, D. D., and E. E. Budzinski, Empirical models of height integrated conductivities, *J. Geophys. Res., 86*, 125, 1981.

Watson, C. E., V. A. Dulock, Jr., R. S. Stolarski, and A. E. S. Green, Electron impact cross sections for atmospheric species, 3. molecular oxygen, *J. Geophys. Res., 72*, 3961, 1967.

Winningham, J. D., D. T. Decker, J. U. Kozyra, J. R. Jasperse, and A. F. Nagy, Energetic (> 60 eV) atmospheric photoelectrons, *J. Geophys. Res., 94*, 15335, 1989.

Winningham, J. D., T. W. Speiser, E. W. Hones, Jr., R. A. Jeffries, W. H. Roach, D. S. Evans, and H. C. Stenbaek-Nielsen, Rocket-borne measurements of the dayside cleft plasma: the tordo experiments, *J. Geophys. Res., 82*, 1876, 1977.

Zipf, E. C., L. W. Borst, and T. M. Donahue, A mass spectrometer observation of NO in an auroral arc, *J. Geophys. Res., 75*, 6371, 1970.